

**Interaction of Surface and Gas Phase Chemistry
in the High Temperature Catalytic Methane Oxidation
on Platinum**

vorgelegt von Diplom - Chemiker

Michael Geske

aus Frankfurt (Oder)

Von der Fakultät II - Mathematik und Naturwissenschaften
der Technischen Universität Berlin
zur Erlangung des akademischen Grades

Doktor der Naturwissenschaften

- Dr. rer. nat. -

genehmigte Dissertation

Promotionsausschuß:

Vorsitzender: Prof. Dr. M. Gradzielski

Berichter: Prof. Dr. R. Schlögl

Berichter: Prof. Dr. R. Schomäcker

Tag der wissenschaftlichen Aussprache: 28. August 2009

Berlin 2009

D 83

für meine Familie

In der Wissenschaft gleichen wir alle nur den Kindern, die am Rande des Wissens hie und da einen Kiesel aufheben, während sich der weite Ozean des Unbekannten vor unseren Augen erstreckt.

Isaac Newton
(Physiker, 1643-1727)

Abstract

Goal of the present work was the analysis of the complex interplay between surface and gas phase reactions using the catalytic partial oxidation of methane as reference system. The focus of the work was the detection and quantification of reactive gas phase intermediates to verify or rebut existing reaction models.

The reaction was performed at industrial relevant conditions of temperatures up to 1300 °C, total flows of about 1000 ml · min⁻¹ and atmospheric pressure. The reactor consisted of a resistively heated platinum tube, which acted as reaction tube and catalyst simultaneously. Reactive species were analyzed using a Threshold Ionization Mass Spectrometer. It allows the detection of small amounts of analyte in a matrix of interfering species, appearing at the same m/z ratio, by its ionization potential. The stabilization of reactive species was achieved by expanding a small gas fraction from the atmospheric pressure reaction mixture into a surrounding vacuum through an orifice of about 125 μm. This step represented the first stage of a three stage pumped vacuum system, which creates by a skimmer and collimator arrangement a molecular beam, that couples the reactor to the mass spectrometer. By the resulting supersonic expansion radicals and other species were quenched. The molecular beam therefore represents, with some restrictions, the gas phase above the catalyst.

The first task was the validation of the experimental system in terms of analysis of several key data, as e.g. energy spread and offset of the MS, its detection limits and the separation effects, occurring inside a molecular beam.

The found energy offset of 1.1 eV and the energy spread of 0.6 eV were low enough to allow the unambiguous identification of all expected reaction intermediates, except for the OH· radical, as the not consumed ¹³CH₄ will become ionized at subjacent energies. Using an internal standard allowed additionally the quantitative

data analysis.

Temperature profile measurements and off gas GC analysis identified two independent reaction ignitions. The first could be described as the catalytic oxidation of methane with CO , CO_2 , H_2O and H_2 as only products. Depending on flow rate, temperature and gas composition a second ignition was observed at much higher temperatures, which was described by a more complex product distribution. With the appearance of C2 products also $CH_3\cdot$ radical could be detected. Their molecular flow correlated with the concentration of the C2 products. Together with the simultaneous occurrence of higher, highly unsaturated hydrocarbons as diacetylene or several C3 species it was concluded that these molecules were formed by homogeneous reaction pathways. The change in the oxygen conversion from about 80 %, due to a laminar flow profile inside the tube, to 100 % and the appearance of flames supported this theory. Experiments with varying flow rates and reactant stoichiometries revealed the exclusive formation of the radical in the gas phase.

One can conclude that heterogeneous and homogeneous reactions can run in parallel. Surface bound reactions release heat into the surrounding gas phase and, at a certain temperature, pyrolysis may start which is responsible for the formation of radicals and coupling products. Additionally gas phase oxidation reactions ignite generating more CO_x and several radicals ($H\cdot$, $CH_3\cdot$, $OH\cdot$), which can have an impact onto the reaction mechanism. Unfortunately beside $CH_3\cdot$ no other radicals could be observed due to the expected very low concentrations below the detection limit of the MS. At least for the methane CPO under the chosen conditions heterogeneous and homogeneous reactions are coupled by the exchange of heat, but not by reactive species themselves.

This work is the first experimental detection and quantification of methyl radicals under such reaction conditions.

Kurzfassung

Das Ziel der vorliegenden Arbeit war die Analyse des komplexen Netzwerkes zwischen Gasphasen und Oberflächenreaktionen, unter Verwendung der katalytischen Partialoxidation von Methan als Beispielsystem. Der Fokus der Arbeit richtete sich auf die Detektion und Quantifizierung von reaktiven Gasphasenintermediaten, um in der Literatur diskutierte Reaktionsmodelle zu unterstützen oder zu entkräften.

Die Reaktion wurde unter industriell relevanten Bedingungen mit Temperaturen von bis zu $1300\text{ }^{\circ}\text{C}$, Gesamtflüssen von $1000\text{ ml} \cdot \text{min}^{-1}$ und bei Atmosphärendruck durchgeführt. Der Reaktor bestand aus einem widerstandsgeheizten Platinröhrchen, welches gleichzeitig als Reaktionsrohr und Katalysator diente. Reaktive Verbindungen wurden mit Hilfe von Threshold Ionization Massenspektrometrie detektiert. Dies erlaubte die Bestimmung von kleinen Mengen des Analyten in einer Matrix störender Verbindungen, die bei dem gleichen m/z Verhältnis auftreten, durch die zugehörigen Ionisierungspotenziale. Die Stabilisierung der reaktiven Spezies erfolgte durch Expansion einer kleinen Gasfraktion aus dem Reaktor durch eine kleine, $125\text{ }\mu\text{m}$ große Öffnung in ein umgebenes Vakuum. Die sich ergebene Überschall-expansion for Radikale und weitere vorhandene Spezies ein. Die folgende Formung eines Molekularstrahls mithilfe von Skimmer und Kollimator gewährleistete einen schnellen und stoßfreien Transport in die Ionenquelle des Massenspektrometers. Damit bildet der Molekularstrahl, mit gewissen Einschränkungen, die Gasphase direkt über dem Katalysator ab.

Die erste Aufgabe war die Untersuchung des experimentellen Aufbaus in Bezug auf einige Schlüsselfaktoren, wie die Energieverbreiterung und der Offset des Massenspektrometers, Erfassungsgrenzen und auftretende Separationseffekte innerhalb des Strahls.

Der bestimmte Offset von 1.1 eV und die Energieverbreiterung von 0.6 eV waren ausreichend, um eine ungestörte Identifikation aller erwarteten Intermediate zuzulassen; mit Ausnahme von OH· Radikalen, da nicht umgesetztes $^{13}\text{CH}_4$ Methan bei geringeren Energien ionisiert und dieses Signal überlagert. Die Verwendung eines internen Standards erlaubte zusätzlich die quantitative Auswertung der Daten.

Messungen von Temperaturprofilen und Produktgasuntersuchungen mittels GC identifizierten zwei unabhängige Reaktionszündungen. Die erste ließ sich als katalytische Oxidation des Methans zu CO, CO₂, H₂O und H₂ als Produkte beschreiben. Abhängig von der Flussgeschwindigkeit, der Temperatur und der Gaszusammensetzung wurde eine zweite Zündung beobachtet, die bei höheren Temperaturen auftritt und ein komplexeres Produktbild zeigte. Mit dem Auftreten von C2 Verbindungen wurden auch CH₃ Radikale detektiert. Ihr molekularer Fluss korrelierte mit dem der C2 Produkte. Zusammen mit dem zeitgleichen Erscheinen von höheren, stark ungesättigten Kohlenwasserstoffen wie Diacetylen und verschiedene C3 Spezies, wurde auf Reaktionen in der Gasphase geschlossen. Die Steigerung des Sauerstoffumsatzes von rund 80 % auf Grund eines laminaren Flussprofils im Reaktorrohr auf 100 % und das Auftreten von Flammerscheinungen im Rohr unterstützen diese Theorie. Experimente mit veränderten Flussgeschwindigkeiten und Reaktant Stöchiometrien belegten die ausschließliche Bildung der Methylradikale in der Gasphase.

Zusammenfassend kann gefolgert werden, dass heterogene und homogene Reaktionen parallel ablaufen. Dabei dienen oberflächengebundene Reaktionen ausschließlich zur Erwärmung der Gasphase. Ab einer bestimmten Temperatur können Pyrolysereaktionen starten, die für die Bildung von Methylradikalen und Kopplungsprodukten verantwortlich sind. Zusätzlich zünden Gasphasenverbrennungsreaktionen, welche weiteres CO_x bilden und ebenfalls durch verschiedene Radikale (H·, CH₃·, OH·) in den Reaktionsmechanismus eingreifen. Außer CH₃· konnte kein weiteres Radikal nachgewiesen werden, was auch an den zu erwartenden, wesentlich geringeren Konzentrationen unterhalb der Detektionsgrenze des MS lag. Zumindest für die Methan CPO unter den gewählten Bedingungen sind homogene und heterogene Reaktionen demzufolge durch Wärmetransport, aber nicht durch Stofftransport gekoppelt.

Diese Arbeit beschreibt die erste Detektion und Quantifizierung von Methylradikalen unter solchen Reaktionsbedingungen.

Contents

| | |
|---|----------|
| List of Abbreviations | vii |
| List of Symbols | x |
| I Introduction | 1 |
| 1 Introduction | 2 |
| II Background | 5 |
| 2 Background | 6 |
| 2.1 Catalytic and Non-Catalytic Methane Activation | 6 |
| 2.1.1 Principles of Heterogeneous Catalysis | 6 |
| 2.1.2 Methane Activation by Heterogeneous Catalysis | 8 |
| 2.1.3 Non-Catalytic Methane Activation: Methane Pyrolysis and Methane Combustion | 15 |
| 2.1.4 Interaction of Catalytic and Non-Catalytic Reactions in Methane Oxidation | 20 |
| 2.2 Molecular Beam Threshold Ionization Mass Spectrometry | 23 |
| 2.2.1 Molecular Beam Principles | 23 |
| 2.2.2 Molecular Beam Characterization | 26 |

| | | |
|------------|--|-----------|
| 2.2.3 | Molecular Beam Applications | 29 |
| 2.2.4 | Threshold Ionization Mass Spectrometry | 30 |
| III | Experimental | 34 |
| 3 | Experimental | 35 |
| 3.1 | Molecular Beam Mass Spectrometry | 35 |
| 3.1.1 | Reactor | 35 |
| 3.1.2 | Vacuum System | 37 |
| 3.1.3 | Mass Spectrometer | 39 |
| 3.1.4 | Pyrometer | 39 |
| 3.2 | Gas Supply and Reactor Off-Gas Analysis | 41 |
| IV | Results & Discussion | 45 |
| 4 | Results and Discussion | 46 |
| 4.1 | Key Data of the Experimental Setup | 46 |
| 4.1.1 | Gas Flow through Orifice | 46 |
| 4.1.2 | Enrichment of Heavier Species in the Molecular Beam Center . | 50 |
| 4.1.3 | Offset and Energy Spread of the Mass Spectrometer | 53 |
| 4.1.4 | Quantification of Radicals by Threshold Ionization | 58 |
| 4.1.5 | Detection Limits by using Threshold Ionization | 59 |
| 4.1.6 | GC Calibration | 65 |
| 4.1.7 | Identification of Unknown Components by GC-MS | 66 |
| 4.1.8 | Standardless GC Quantification | 67 |
| 4.1.9 | Pyrometer Stability | 69 |

| | | |
|----------|---|------------|
| 4.2 | Description of Flow Parameters | 70 |
| 4.2.1 | Convective Mass Transport through the Reactor | 70 |
| 4.2.2 | Radial Mass Transport by Diffusion | 74 |
| 4.3 | Catalytic Partial Oxidation of Methane on <i>Pt</i> | 77 |
| 4.3.1 | Ignition Studies | 77 |
| 4.3.2 | Reaction Zone Shifting | 79 |
| 4.3.3 | Visual Examination of the Reaction Zones | 82 |
| 4.4 | Catalytic Partial Oxidation of Methane - $C/O = 0.6$ | 85 |
| 4.4.1 | Product Gas Composition at $C/O = 0.6$ | 87 |
| 4.4.2 | Radical Detection and Quantification at $C/O = 0.6$ | 90 |
| 4.4.3 | Unsaturated Higher Hydrocarbons at $C/O = 0.6$ | 98 |
| 4.5 | Catalytic Partial Oxidation of Methane - variable C/O Ratios and Gas Flows | 102 |
| 4.5.1 | Temperature Profiles for variable C/O Ratios | 102 |
| 4.5.2 | Conversions and Selectivities for variable C/O Ratios | 103 |
| 4.5.3 | Gas phase Ignition and Ignition Delay | 106 |
| V | Summary | 112 |
| 5 | Summary | 113 |
| | Bibliography | 117 |
| | List of Figures | 130 |
| | List of Tables | 138 |
| | Acknowledgement | 140 |
| | Curriculum Vitae | 141 |

List of Abbreviations

| abbreviation | explanation |
|--------------|--|
| AP | Appearance Potential |
| CPO | Catalytic Partial Oxidation |
| CVD | Chemical Vapor Deposition |
| EFC | Electronic Flow Controller |
| EI | Electron Ionization |
| EPR | Electron Paramagnetic Resonance |
| ETD | Everhart Thornley Detector |
| FID | Flame Ionization Detector |
| FWHM | Full Width at Half Maximum |
| GC | Gas Chromatography |
| GHSV | Gas Hourly Space Velocity |
| IE | Ionization Energy |
| IP | Ionization Potential |
| LFL | Lower Flammable Limit |
| LIF | Laser Induced Fluorescence |
| MBMS | Molecular Beam Mass Spectrometry |
| MN | Mach Number |
| MS | Mass Spectrometry |
| NIST | National Institute of Standards and Technology |
| QMS | Qadrupole Mass Spectrometry |
| SEM | Scanning Electron Microscopy |
| SSD | Solid State Detector |
| STP | Standard Temperature and Pressure |

| | |
|------------|--|
| TCD | T hermal C onductivity D etector |
| UFL | U pper F lammable L imit |
| UHV | U ltra H igh V acuum |
| XPS | X -ray P hotoelectron S pectroscopy |

List of Symbols

fundamental constants

| symbol | explanation | numerical value |
|--------|---------------------------|---|
| amu | atomic mass unit | $1.66056 \cdot 10^{-27} \text{ kg}$ |
| C_1 | first radiation constant | $3.74177118 \cdot 10^{-16} \text{ W} \cdot \text{m}^2$ |
| C_2 | second radiation constant | $1.4387752 \cdot 10^{-2} \text{ m} \cdot \text{K}$ |
| h | Planck's constant | $6.62618 \cdot 10^{-34} \text{ J} \cdot \text{s}$ |
| k | Boltzmann's constant | $1.38066 \cdot 10^{-23} \text{ J} \cdot \text{K}^{-1}$ |
| R | universal gas constant | $8.31451 \text{ J} \cdot \text{mol}^{-1} \cdot \text{K}^{-1}$ |

mathematical notation

notation meaning

| | |
|----------------|-------------------------------|
| $\frac{d}{dv}$ | differentiation after v |
| dx | differential increment of x |
| $f(x)$ | function of x |
| \bar{x} | mean value of x |
| $\Delta \dots$ | increment of ... |
| $\Sigma \dots$ | Sum of ... |

common subscripts and superscripts

| symbol | explanation | type |
|--------|---|-----------|
| cc | indicates parameter in the collimator chamber | subscript |
| D | diameter | subscript |
| in | indicating inlet direction | subscript |
| M | Mach disk | subscript |
| max | maximum value | subscript |

| | | |
|----------|--|-------------|
| nc | indicates parameter in the nozzle chamber | subscript |
| out | indicating outlet direction | subscript |
| r | reaction | subscript |
| s | surface | subscript |
| sc | indicates parameter in the skimmer chamber | subscript |
| x | value for non specified stoichiometry | subscript |
| 0 | normal state (for gases $p = 101325 Pa, T = 273.15 K$) | superscript |
| Θ | standard state (for gases $p = 101325 Pa, T = 298.15 K$) | superscript |
| * | maximum values | superscript |

specific symbols

| symbol | explanation | unit |
|--------------------|---|---|
| A | surface area | $[A] = cm^2$ |
| A | detector signal | $[A] = cps$ |
| c | concentration | $[c] = 1 Vol\% \equiv 10000 ppm$ |
| C/O | carbon to oxygen feed gas ratio | $[C/O] = 1$ |
| C_p | isobar heat capacity | $[C_p] = J \cdot K^{-1}$ |
| C_v | isochore heat capacity | $[C_v] = J \cdot K^{-1}$ |
| D | tube diameter | $[D] = m$ |
| D | diffusion coefficient | $[D] = cm^2 \cdot s^{-1}$ |
| d_n | orifice diameter | $[d_n] = m$ |
| E | energy of electrons | $[E] = eV$ |
| E_a | activation energy | $[E_a] = J$ |
| $E_{\lambda,b}(T)$ | spectral radiation energy | $[E_{\lambda,b}(T)] = J \cdot m^{-2} \cdot sr^{-1}$ |
| \dot{F} | molar flow | $[\dot{F}] = mol \cdot s^{-1}$ |
| f_T | translational degrees of freedom | $[f_T] = 1$ |
| f_R | rotational degrees of freedom | $[f_R] = 1$ |
| f_v | vibrational degrees of freedom | $[f_v] = 1$ |
| G | pressure ratio | $[G] = 1$ |
| G^* | critical pressure ratio for supersonic expansion | $[G^*] = 1$ |

| | | |
|-------------------|---|--|
| i | ion current | $[i] = \text{counts} \cdot \text{s}^{-1} = \text{cps}$ |
| I_e | ionizer emission current | $[I_e] = A$ |
| j_m | mass flux | $[j_m] = \text{kg} \cdot \text{m}^{-2} \cdot \text{s}^{-1}$ |
| k | reaction rate constant | $[k] = (\text{l} \cdot \text{mol}^{-1})^{v-1} \text{s}^{-1}$ |
| K | pyrometer specific geometric constant | $[K] = 1$ |
| k_0 | preexponential factor | $[k_0] = (\text{l} \cdot \text{mol}^{-1})^{v-1} \text{s}^{-1}$ |
| Kn | Knudsen number | $[Kn] = 1$ |
| L | tube length | $[L] = \text{m}$ |
| l_{cage} | length of the ionizer | $[l_{\text{cage}}] = \text{m}$ |
| m | mass | $[m] = \text{kg}$ |
| M | molar mass | $[M] = \text{kg} \cdot \text{mol}^{-1}$ |
| \bar{M} | mean molar mass | $[\bar{M}] = \text{kg} \cdot \text{mol}^{-1}$ |
| m/z | mass to charge ratio | $[m/z] = \text{amu}$ |
| MN_{max} | maximum reachable Mach number | $[MN_{\text{max}}] = 1$ |
| MN | Mach number | $[MN] = 1$ |
| n | number of electrons | $[n] = 1$ |
| n | particle density | $[n] = \text{m}^{-3}$ |
| p | pressure | $[p] = \text{Pa}$ |
| P_i | probability of ionization | $[P_i] = 1$ |
| \dot{q}_m | mass flow | $[\dot{q}_m] = \text{kg} \cdot \text{s}^{-1}$ |
| R | MS signal response factor between analyte and standard | $[R] = 1$ |
| Re | Reynolds number | $[Re] = 1$ |
| S | MS signal | $[S] = \text{cps}$ |
| S | selectivity | $[S] = \%$ |
| t | transmission efficiency | $[t] = 1$ |
| T | temperature | $[T] = K$ |
| U | thermal electron energy | $[U] = \text{eV}$ |
| V | applied potential | $[V] = \text{eV}$ |
| \dot{V} | volumetric flow | $[\dot{V}] = \text{m}^3 \cdot \text{s}^{-1}$ |
| x | distance | $[x] = \text{m}$ |
| X | molar fraction | $[X] = 1$ |
| X | conversion | $[X] = \%$ |

| | | |
|--------------------|--|--|
| y | displacement orifice - skimmer | $[y] = m$ |
| Z | number of three body collisions | $[Z] = s^{-1} \cdot m^{-3}$ |
| α | enrichment factor | $[\alpha] = 1$ |
| β | extraction efficiency | $[\beta] = 1$ |
| γ | adiabatic exponent | $[\gamma] = 1$ |
| $\bar{\gamma}$ | mean adiabatic exponent | $[\bar{\gamma}] = 1$ |
| δ | distance to approach collision | $[\delta] = m$ |
| ΔG^\ominus | Gibbs free energy | $[\Delta G^\ominus] = J \cdot mol^{-1}$ |
| ΔH^\ominus | enthalpy | $[\Delta H^\ominus] = J \cdot mol^{-1}$ |
| ΔS^\ominus | entropy | $[\Delta S^\ominus] = J \cdot mol^{-1} \cdot K^{-1}$ |
| ϵ | force constant | $[\epsilon] = J$ |
| ϵ_λ | monochromatic emissivity | $[\epsilon_\lambda] = 1$ |
| η | dynamic viscosity | $[\eta] = Pa \cdot s$ |
| λ | wavelength | $[\lambda] = m$ |
| λ | slope of the electron impact ionization cross section | $[\lambda] = m^2 \cdot eV^{-1}$ |
| $\bar{\lambda}$ | mean free path | $[\bar{\lambda}] = m$ |
| Ω | collision integral | $[\Omega] = 1$ |
| Φ | filament work function | $[\Phi] = eV$ |
| ρ | density | $[\rho] = kg \cdot m^{-3}$ |
| σ | standard deviation | $[\sigma] = 1$ |
| σ | binary collision cross section | $[\sigma] = m^2$ |
| σ | collision diameter for the Lennard-Jones-Potential | $[\sigma] = pm$ |
| τ | time for ignition delay | $[\tau] = s$ |
| τ_C | time for convective transport | $[\tau_C] = s$ |
| τ_D | time for diffusion | $[\tau_D] = s$ |
| Θ | detector sensitivity | $[\Theta] = 1$ |
| Θ_v | critical excitation wave number | $[\Theta_v] = cm^{-1}$ |
| v | velocity | $[v] = m \cdot s^{-1}$ |
| \tilde{v} | wave number | $[\tilde{v}] = cm^{-1}$ |

Part I

Introduction

Chapter 1

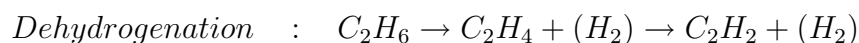
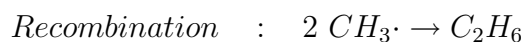
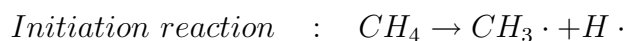
Introduction

Catalysis is very present in our everyday life. Apart from automotive catalysis, which is often the only catalytic application of public awareness, about 90 % of all chemical conversions are accomplished with catalysts [1]. To illustrate the scale on which catalytic processes are conducted in industry, catalytic cracking of crude oil can be taken as example. About $3.9 \cdot 10^9$ tons of crude oil are processed by catalytic cracking on zeolites every year. Facing this number, the economic aspects of catalysis research are obvious. Already a small improvement in terms of conversion, selectivity or catalyst lifetime can reduce costs and environmental pollution drastically.

As already a simple catalytic reaction as the ammonia synthesis consists of adsorption, decomposition, recombination and desorption steps [2] the development of an atomistic understanding of catalytic reactions is very challenging, costly and time consuming. The industrial way of upgrading existing catalysts and processes is often dominated by a "trial and error" approach [3]. Improvements are made by changing catalyst formulation or process conditions without an in-depth analysis of the underlying reaction mechanism. The interplay between the active catalyst, the support and the reaction media is very complex and in the majority of cases not understood. The nature of the "active site", defined as the combination of functional groups which are essential for the catalytic reaction, is object of intensive work [4] but remains unknown in many cases. The situation is further complicated by the fact that a catalyst typically changes its composition or shape under reaction atmosphere [5] making it necessary to analyze as many parameters in situ as possible.

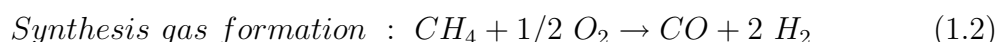
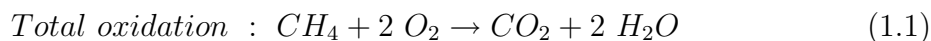
In many industrial processes and in the present work, heterogeneous catalytic

reactions are conducted at high temperatures ($T > 500\text{ }^{\circ}\text{C}$) and atmospheric or elevated pressures. Under such drastic conditions, non-catalytic reactions can occur in the gas phase surrounding the catalyst and the atomistic picture of the entire process becomes even more complex. Taking methane activation as example, the $C - H$ bond dissociation energy in methane is about $435\text{ kJ} \cdot \text{mol}^{-1}$ ($104\text{ kcal} \cdot \text{mol}^{-1}$) [6]. At temperatures above $1100\text{ }^{\circ}\text{C}$ a noticeable fraction of $C - H$ bonds break and gas phase radical reactions can be initiated [7, 8]. After bond cleavage the methyl radicals can recombine to form ethane and depending on temperature by dehydrogenation, unsaturated species like ethylene and acetylene.



Gas phase reactions become typically more important with increasing pressure which can be a problem for industrial processes which operate often at pressures of 1 to 100 *bar* [9]. This pressure dependence is easily understood as the number of intermolecular collisions increases with pressure.

The aim of this work was the analysis of the interplay between heterogeneous surface reactions and homogeneous gas phase reactions during the partial oxidation of methane at temperatures up to $1300\text{ }^{\circ}\text{C}$ and atmospheric pressure over a platinum catalyst. Literature results indicate that next to surface reactions producing CO_2 , H_2O and synthesis gas ($\text{CO} + \text{H}_2$) (Eq. 1.1-1.2 and Fig. 1.1) [10], also C2 hydrocarbons are formed in a homogeneous reaction [11] via radical recombination.



The C2 products are thought to be formed by recombination of methyl radicals, but an in situ observation under atmospheric pressure and high temperature conditions has never been performed.

The first task to study the formation process of C2 products would be to correlate the concentration of $\text{CH}_3 \cdot$ radicals in the gas phase with the formation of C2

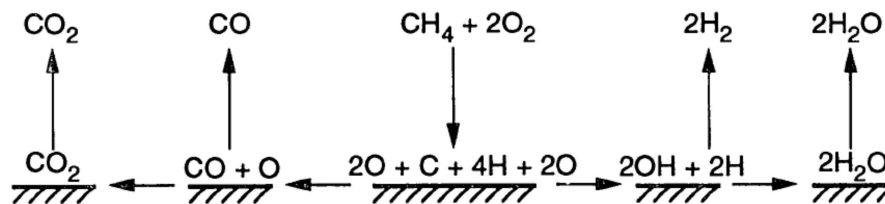


Figure 1.1: Simplified surface mechanism for syngas formation and total oxidation - adopted from [10].

hydrocarbons. If such a correlation could be established, the gas phase recombination mechanism was supported. If high amounts of C_2 hydrocarbons were formed without that methyl radicals were detected in the gas phase, a direct radical coupling on the surface could be the formation pathway.

Secondly the origin of gas phase methyl radicals must be clarified. They could be either produced on the *Pt* surface and desorb into the gas phase, or generated homogeneously in the gas phase. Radical formation in the gas phase is typical for combustion processes or methane pyrolysis. Other radicals such as $OH\cdot$ formed by hydrogen oxidation which in turn is formed by surface chemistry (c.f. Fig 1.1) can initiate methane fission.

It can be summarized that the question of the connection between gas phase and surface reactions for methane oxidation on *Pt* is still unresolved and experimentally largely unexplored. The high rate of methane oxidation on platinum leads to a high rate of heat generation which results in high reaction temperatures and probably a complicated reaction network at the surface and in the gas phase linked by physical transport processes of mass and heat. Numerical simulations can give insight into the reaction mechanism on a molecular scale [12], but the results remain speculative unless they can be confirmed by in situ measurements.

In the present work, a combination of molecular beam mass spectrometry with threshold ionization, optical pyrometry and gas chromatography is applied to study the methane oxidation on *Pt* for the first time in situ at temperatures up to $1300\text{ }^\circ\text{C}$ and atmospheric pressure. Goal is to correlate the production of gas phase radicals with the catalytic performance to study the coupling of surface and gas phase chemistry in this reaction in general and the formation mechanism of C_2 hydrocarbons in particular.

Part II

Background

Chapter 2

Background

2.1 Catalytic and Non-Catalytic Methane Activation

The following chapter will introduce the basic principles of heterogeneous catalysis and the difference between catalytic and non-catalytic reactions. As methane oxidation is the subject of this work examples will be given how methane can be activated by means of heterogeneous catalysis but also non-catalytically by combustion and pyrolysis reactions. The chapter finishes by giving an overview over the state of knowledge about methane oxidation reactions involving catalytic and non-catalytic reaction pathways.

2.1.1 Principles of Heterogeneous Catalysis

A chemical reaction that possesses a negative Gibbs free energy could, at least from a thermodynamic point of view, proceed spontaneously (Eq. 2.1). However, even a spontaneous reaction might proceed immeasurably slow if it is hindered by a high activation barrier. As displayed in Fig. 2.1, a catalyst is a substance that lowers the activation barrier for a specific chemical reaction without influencing its thermodynamics.

$$\text{Gibbs free energy} : \Delta G = \Delta H - T\Delta S \quad (2.1)$$

$$\begin{aligned} \text{spontaneous reaction } \Delta G &< 0 \\ \text{equilibrium state } \Delta G &= 0 \\ \text{nonspontaneous reaction } \Delta G &> 0 \end{aligned}$$

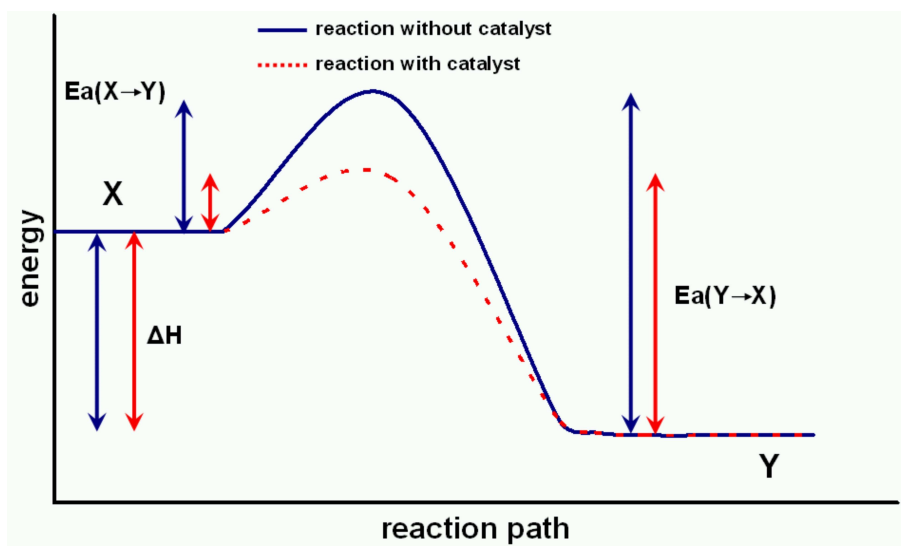
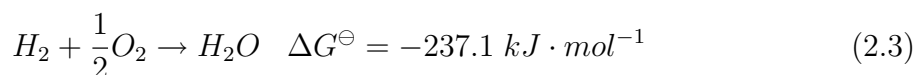


Figure 2.1: Activation barrier for a reaction $X \rightarrow Y$ with and without catalyst. The reaction enthalpy ΔH is equal for both, but the activation energies E_a are reduced for the catalytic reaction. - Adopted from [13].

The reaction enthalpy ΔH is the same for the catalytic and the noncatalytic reaction but as the reaction rate depends exponentially on the negative of the activation energy (Eq. 2.2), the reaction rate of a catalytic reaction is higher at a given temperature than that of a non-catalytic reaction. Vice versa, the same reaction rate is achieved at a lower temperature due to the lower E_a for the catalytic reaction (red) compared to the non-catalytic reaction (blue).

$$k = k_0 e^{-\frac{E_a}{RT}} \quad (2.2)$$

An example is the oxidation of hydrogen with oxygen to water (Eq. 2.3).



According to Eq. 2.3, the Gibbs free energy is very negative for this reaction and it could proceed spontaneously. However, a mixture of H_2 and O_2 can be stored

for decades without that a measurable conversion occurs as the reaction involves a high activation barrier. If the necessary activation energy is provided by means of an external energy source (flames, sparks, etc) an explosion occurs. Contrary, flowing hydrogen over a platinum sponge in air will immediately result in a flame. The platinum sponge acts as a catalyst by reducing the activation energy by dissociative adsorption of both gases and the reaction can proceed with a high rate. This is the principle of the first lighter invented by Johann Wolfgang Döbereiner ("Döbereiner's lamp").

The economic importance of catalysts results from the fact that a catalyst can be designed to increase, in a set of spontaneous reactions, the rate of one reaction stronger than the rates of the others. This leads to the concepts of selectivity, i.e. a catalyst can be used to accelerate the formation of the desired product at the expense of the undesired products. An example is the conversion of synthesis gas (a mixture of CO and H_2) to a variety of products over different catalysts as shown in Fig. 2.2.

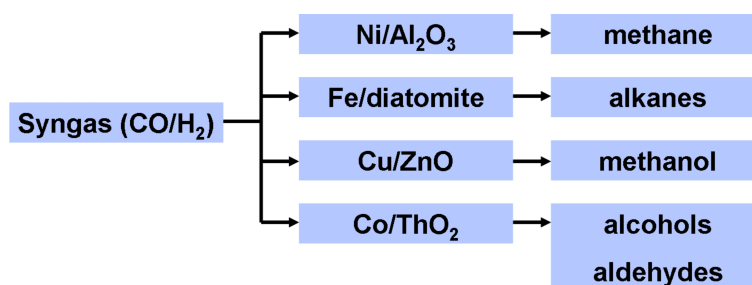


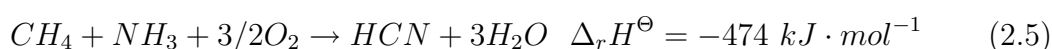
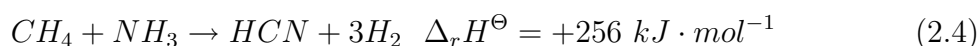
Figure 2.2: Selectivity control by catalysts, adopted from [14].

2.1.2 Methane Activation by Heterogeneous Catalysis

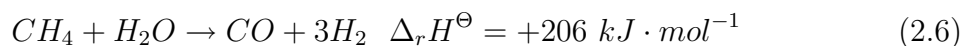
The conversion of methane to more valuable chemicals is one of the major topics in heterogeneous catalysis research during the last decades. The primary driving force is to use natural gas as chemical feedstock instead of crude oil. The difficulty of transformation arises from the strong $C-H$ bonds in methane with bond energies of about $\Delta H^\ominus(H-CH_3) = 435 \text{ kJ}\cdot\text{mol}^{-1}$ [15]. The activation is further complicated by the fact that the methane molecule does not possess a permanent dipole moment and that the electron cloud possesses nearly spherical symmetry. If high temperature/high

pressure conditions are chosen to oxidize methane to desired products like ethylene, formaldehyde or methanol, the target molecules react readily to CO_x and H_2O .

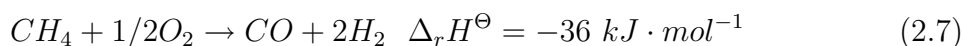
Despite these challenges several conversion pathways have reached industrial stage, e.g. the formation of hydrocyanic acid from methane and ammonia via the Degussa process (Eq. 2.4, [16]) or the Andrussov process (Eq. 2.5, [17]):



Another large scale methane conversion process is the production of synthesis gas via steam reforming on *Ni* catalysts, which has been investigated and used for more than 50 years [18] Eq. 2.6:

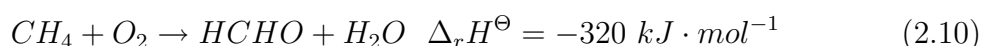
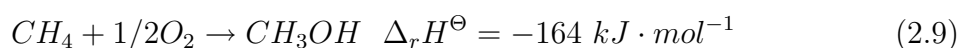


The production of synthesis gas by catalytic partial oxidation (CPO, Eq. 2.7, e.g. on *Rh*) has reached pilot plant status.



The advantage of catalytic partial oxidation is that the reaction approaches equilibrium within *ms* contact times and that CPO reactors can operate autothermally and can be much smaller than conventional steam reformers [19].

Currently under research are methane oxidative coupling to ethylene [20] (Eq. 2.8) and the direct oxidation of methane to methanol or formaldehyde [21] (Eqs. 2.9 and 2.10):



Whereas the oxidative coupling of methane (Eq. 2.8) can provide up to 25 % one pass yield of *C2* coupling products and has a certain potential for industrial application the direct oxidation of methane to formaldehyde or methanol provides only a few percent yield [21] and is currently only of academic interest.

As the focus of the present work is on the mechanism of the high temperature methane oxidation and the interaction between catalytic (surface) and non-catalytic (gas phase) reactions, mechanistic details of selected catalytic processes of methane conversion will be discussed in the following. After reviewing mechanistic aspects of non-catalytic methane activation by combustion and pyrolysis in Section 2.1.3, the state of knowledge for the interaction between catalytic and non-catalytic reactions is discussed in Section 2.1.4.

Catalytic Combustion of Methane

Combustion of hydrocarbons is widely used to produce energy for domestic, transportation or industrial use. Combustion engines rely usually on non-catalytic combustion in flames. Methane (natural gas) is often used as fuel due to its high energy content and environmental friendliness. The common oxidant is air. Unfortunately the combustion in air leads to temperatures $> 1600\text{ }^{\circ}\text{C}$ - and to the emission of NO_x from atmospheric nitrogen [22].

Catalytic combustion offers an interesting alternative to non-catalytic combustion as i) no ignition source is required ii) the combustion temperatures are much lower than in a flame ($< 1300\text{ }^{\circ}\text{C}$) and iii) the hydrocarbon/air mixture can be outside the flammability limits (for methane in air 5–16 Vol% [23]). The only restriction for a self sustained catalytic combustion is a minimum inlet gas temperature to maintain full conversion [24]. For example, the catalytic combustion of 2% methane in air with an inlet temperature of $450\text{ }^{\circ}\text{C}$ will result in an exhaust gas temperature of about $980\text{ }^{\circ}\text{C}$, which is low enough to reduce the emission of NO_x to zero. Temperatures below $1000\text{ }^{\circ}\text{C}$ reduces also the formation of soot and tar and CO_2 and H_2O are the only observed products [25].

The general mechanism of catalytic combustion is presented in Figure 2.3. At point (A) oxidation reactions are initiated on the catalyst surface at a temperature, which depends from the catalyst itself and the used hydrocarbon. Increasing the temperature leads to an exponential increase of the reaction rate (B). At the point, where the produced heat by the combustion process exceeds heat losses, reactor light off is observed (C). At this stage the reaction is controlled by mass transport. In point (D) the reactants are depleted [26]. Relevant for the present work is that

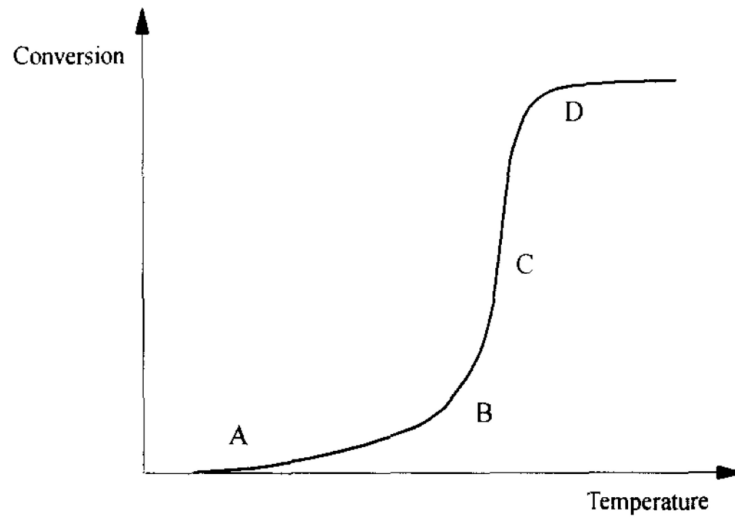
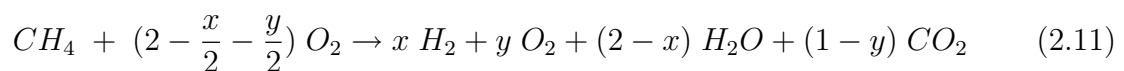


Figure 2.3: General mechanism of catalytic combustion - adopted from [26].

reactive intermediates can be released to the gas phase under catalytic combustion conditions which can initiate gas phase radical chain reactions. Numerical simulations on catalytic combustion systems have been published by numerous authors [27, 28]. An experimental proof of $OH\cdot$ radicals desorbing from the Pt surface under reaction conditions has been given by Pfefferle et al. using LIF [29].

Catalytic Partial Oxidation of Methane on Noble Metals

The catalytic partial oxidation of methane on noble metals is very similar to catalytic combustion but uses methane rich mixtures above the upper flammability limit. Goal is to produce $CO + H_2$ (synthesis gas) in ms contact times. As the formation of small amounts total oxidation products (CO_2 and H_2O) is inevitable, the reaction can be described by Eq. 2.11:

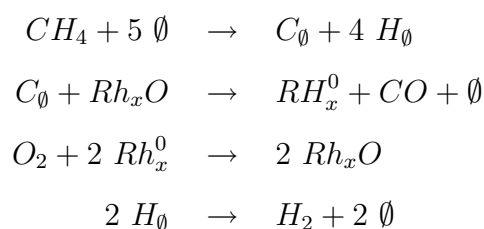


The values of x and y depend strongly on the catalyst and on the operation conditions. On Rh the selectivity to hydrogen is over 90 % [10] and much higher than on Pt which produces more water. The different behavior of the two catalysts results from different activation barriers for the reaction of surface oxygen atoms O_s and surface hydrogen atoms H_s to surface OH_s (Eq. 2.12):



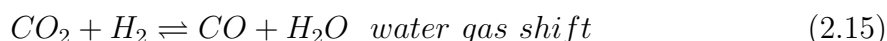
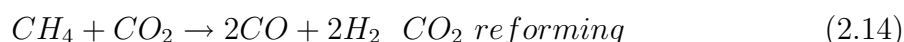
On *Pt* the activation energy for Reaction 2.12 is with only $10.5 \text{ kJ} \cdot \text{mol}^{-1}$ much lower than on *Rh* ($83.8 \text{ kJ} \cdot \text{mol}^{-1}$) [12]. Hence, platinum increases the reaction rate to H_2O making it an excellent catalyst for catalytic combustion applications whereas rhodium hinders this step and is the catalyst of choice for synthesis gas formation.

Other authors propose a Mars - van Krevelen mechanism via rhodium oxide for the formation of CO and metallic rhodium sites for methane splitting and H_2 formation [30].



Chemisorbed oxygen plays a role in the further oxidation of the carbon monoxide to carbon dioxide. The authors stated, that over platinum a similar reaction mechanism takes place, but could not confirm the formation of platinum oxide by ex situ XPS as opposed to rhodium oxide. *In situ* X-ray absorption studies shows the presence of RhO_x and PtO_x at least close to the ignition temperature of about $310^\circ C$ in the oxidation zone [31].

The production of partial oxidation products is furthermore discussed in terms of a two step (indirect) mechanism [32], where first a total oxidation of CH_4 to CO_2 and H_2O occurs, followed by steam and carbon dioxide reforming (Eq. 2.13 and 2.14 respectively). The product distribution can also be changed by side reactions as for example the water gas shift reaction (Eq. 2.15) [33]:

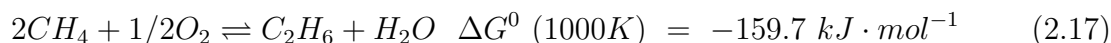
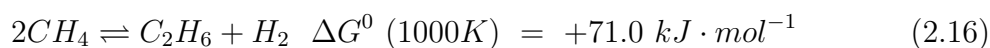


This discussion in terms of direct vs. indirect synthesis gas formation has been somewhat alleviated by introducing spatially resolved measurements through autothermally operated *Pt* and *Rh* coated foam catalysts [8, 34]. It was shown that in the oxidation zone partial and total oxidation reactions proceed in parallel as described by Eq. 2.11. After total consumption of oxygen, water becomes co-reactant

to methane and more synthesis gas is produced by steam reforming. CO_2 is formed in small amounts in the oxidation zone but CO_2 reforming does not occur under autothermal conditions.

Oxidative coupling of methane over oxide catalysts

The coupling of methane to ethane is a reaction of strong economic interest as ethane can be dehydrogenated to ethylene which is a highly valuable chemical intermediate. The dehydrogenative coupling of methane to ethane is thermodynamically unfavored (Eq. 2.16), but an oxidative coupling is thermodynamically feasible (negative Gibbs free energy) (Eq. 2.17) [35]:



Numerous oxide catalysts, in particular strong basic oxides, are active for methane oxidative coupling in a temperature range between 600 – 900 °C. Besides ethane, ethylene is formed and therefore the yield is often specified in terms of C2 products.

The reaction mechanism on many oxides is discussed in terms of a coupled heterogeneous homogeneous mechanism. By using matrix isolation EPR spectroscopy [36, 20], Lunsford et al. showed methyl radical desorption from alkaline doped earth alkaline oxides. The results for Na doped CaO [36] and Li doped MgO [20] catalysts are reproduced in Fig. 2.4 I and II respectively. The authors discovered a correlation between the $CH_3\cdot$ radical production, the C2 yield and the dopant concentration. The authors concluded that gas phase coupling of $CH_3\cdot$ radicals is a major pathway for the formation of C2 products. To understand the role of the alkaline dopant, Ito and Lunsford studied also the Li/MgO catalyst using EPR. By thermal quenching of the catalyst operated at temperatures between 700 °C to 800 °C they showed that $[Li^+O^-]$ defects were present under reaction conditions and concluded that these centers probably facilitate $CH_3\cdot$ radical formation at the surface [37]. After desorption in the gas phase the $CH_3\cdot$ radicals couple to ethane which is further dehydrogenated to ethylene.

Feng et al. used Molecular Beam Photoionization Mass spectrometry for a direct quantification of methyl radicals using NO as internal standard [38]. The comparison

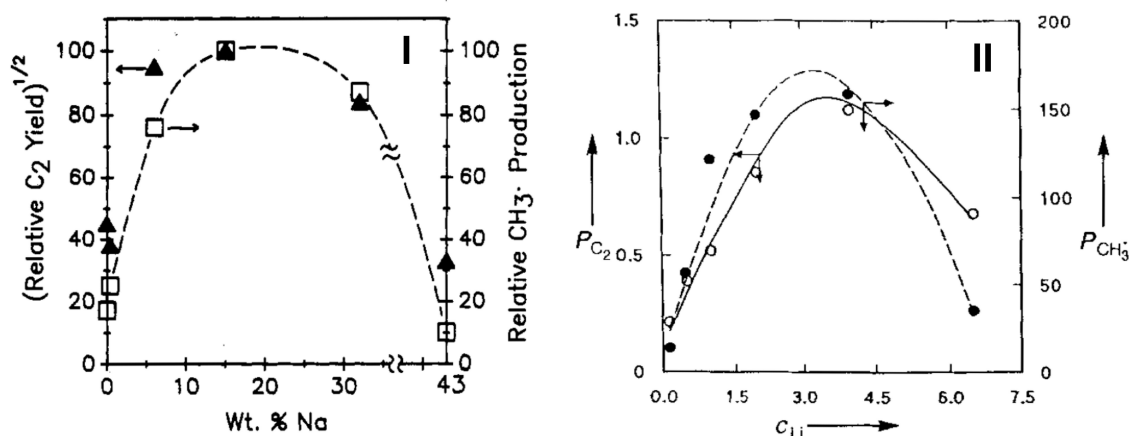


Figure 2.4: I Relative C₂ yield and methyl formation rate as function of the Na⁺ loading - adopted from [36]; II Variation in C₂ and CH₃· productivity as a function of the lithium content at 700 °C - adopted from [20].

of the production of these radicals and the C₂ production, see Fig. 2.5, reveals C₂ formation purely by homogeneous recombination. Neither heterogeneous production of ethane or ethylene, nor deep oxidation of the radicals could be observed [39].

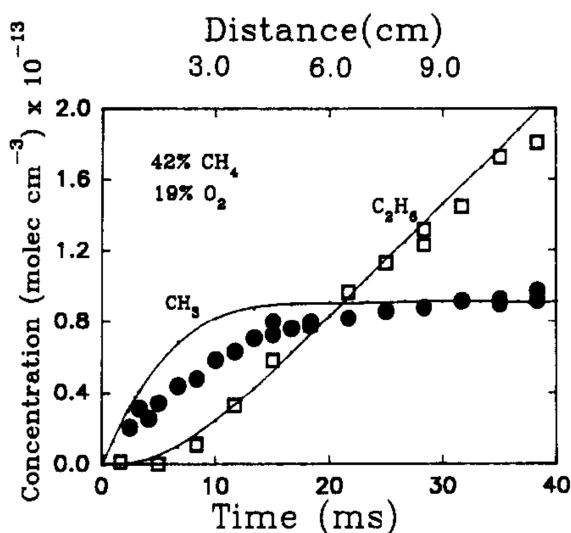


Figure 2.5: Plot of CH₃· and C₂H₆ concentration as function of catalyst contact time - adopted from [39].

Oxidative coupling of methane on Pt

C₂ products are also observed if methane oxidative coupling is conducted on platinum catalysts but the yields at typical oxidative coupling temperatures (600 – 800 °C) are close to zero. Both on Pt/Rh gauzes [40] and coated monoliths [12] no C₂

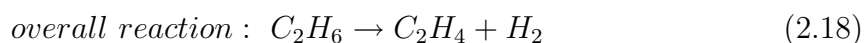
hydrocarbons are observed below 1000 °C and only CO , CO_2 , H_2 and H_2O are formed. If the the temperature is increased to more than 1000 °C traces of C_2 coupling products appear [40] but their formation pathway remains unclear. Lunsford was able to quantify methyl radicals over oxide catalysts at 800 °C [37], but has not found any evidence for these radicals over a platinum surface at temperatures of about 900 °C [41]. He concluded that the role of platinum is to provide a catalytic surface for the oxidation reactions, but not to release radicals. In numerical simulations of the methane CPO on a Pt gauze C_2 production was found to occur downstream the gauze by coupling of methyl radicals in the gas phase [42, 43]. The authors stated that these $CH_3\cdot$ radicals are also produced in the gas phase downstream the gauze and do not desorb from the platinum surface.

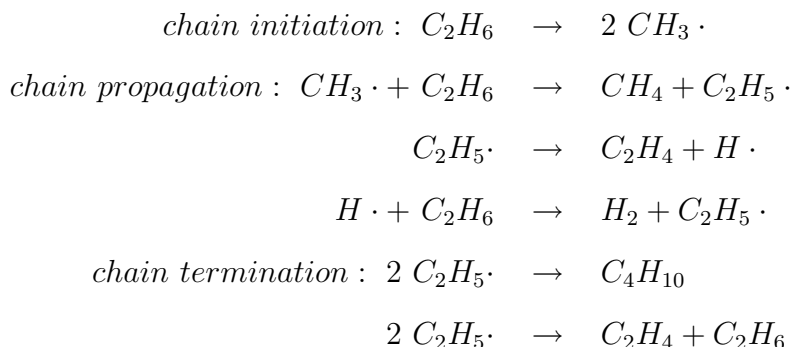
2.1.3 Non-Catalytic Methane Activation: Methane Pyrolysis and Methane Combustion

Methane pyrolysis

Pyrolysis is defined as the thermal decomposition of organic compounds [44] in absence of any oxidant. Even though the present work focusses on catalytic oxidation of methane on Pt , pyrolysis reactions are briefly reviewed in the following as they can proceed in oxygen deficient regions of the reactor. In several experiments described in Section 4 temperatures as high as 1300°C were achieved and methane was used in excess so that pyrolysis reactions have to be taken into account as possible sources of reaction products.

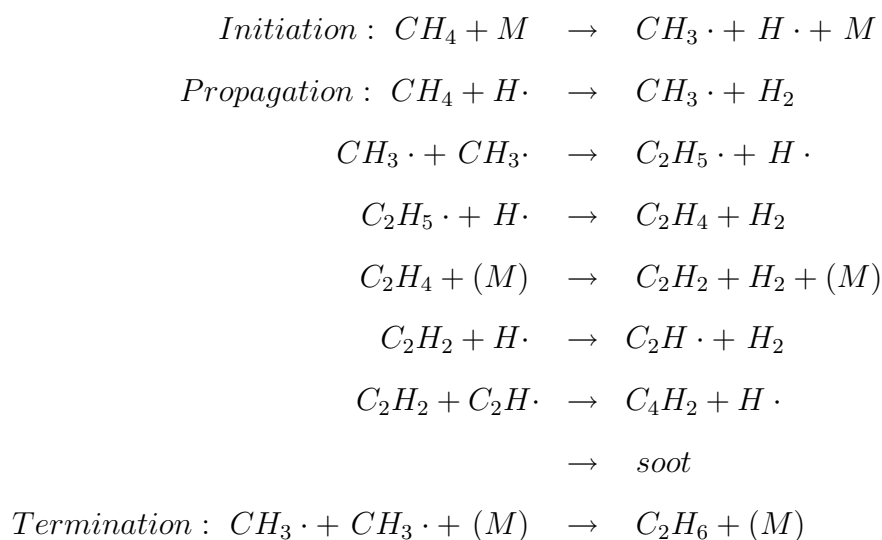
As a simple example the pyrolysis of ethane to ethylene and hydrogen is shown in Eq. 2.18. As can be seen, the term pyrolysis comprises a network of radical reactions in the gas phase consisting of chain initiation, chain propagation and chain termination reactions:





During chain propagation, a new radical is created for each consumed radical. In chain termination reactions radicals are lost due to the radical recombination in the gas phase or destruction at a wall. As the overall reaction is endothermic, energy must be continuously supplied to sustain it.

The initial step in methane pyrolysis is the homolytic $C - H$ bond cleavage. High temperatures are necessary to break this bond as the bond dissociation energy is about $435 \text{ kJ} \cdot \text{mol}^{-1}$ [6]. The main products are hydrogen, acetylene, ethylene and small amounts of higher hydrocarbons. As the complete reaction mechanism is too complex to list it here (157 reactions between 48 different species [45]) only selected important reactions in the methane pyrolysis network are given below (M denotes an inert collision partner):



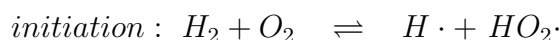
Methane pyrolysis has been thoroughly investigated. Even at low temperatures of 1038 K ($765 \text{ }^\circ\text{C}$) measurable conversions are obtained with a high selectivity to ethane [46]. The author describes the initial steps of soot and tar formation with cyclopentadiene as intermediate. The intensive soot formation was one of the main

reasons not to use methane as chemical feedstock in the low temperature conversion in the past.

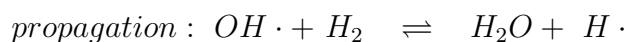
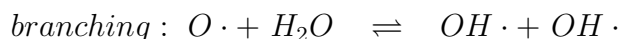
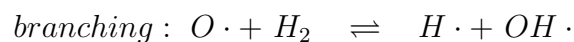
Methane pyrolysis has also been described with mathematical models. Thermodynamic equilibrium calculations including and excluding solid carbon predict a product composition as shown in Fig 2.6 and 2.7 respectively. At temperatures, where acetylene and benzene are produced in significant yields (temperatures from 1800 °C to 3000 °C); graphite and hydrogen are the thermodynamically stable products [47]. The formation of solid carbon can be suppressed by rapid heating and product cooling, as well as addition of hydrogen [48]. In this case higher amounts of acetylene are formed (Fig 2.7). Several industrial acetylene production processes follow this strategy (Huels [49], DuPont [50]).

Non-catalytic combustion of methane

The non-catalytic (gas phase) combustion of methane proceeds, like methane pyrolysis via a network of radical chain reactions. An important difference to pyrolysis is that the methane combustion is exothermic and can proceed self-sustained upon ignition. Furthermore chain branching can occur which can lead depending on composition temperature and pressure to an explosion. A simple and well understood example for a combustion reaction is the combustion of hydrogen [51]. In the $H_2 - O_2$ system the initiation occurs mainly by the reaction



Upon initiation chain branching and propagation reactions may occur:



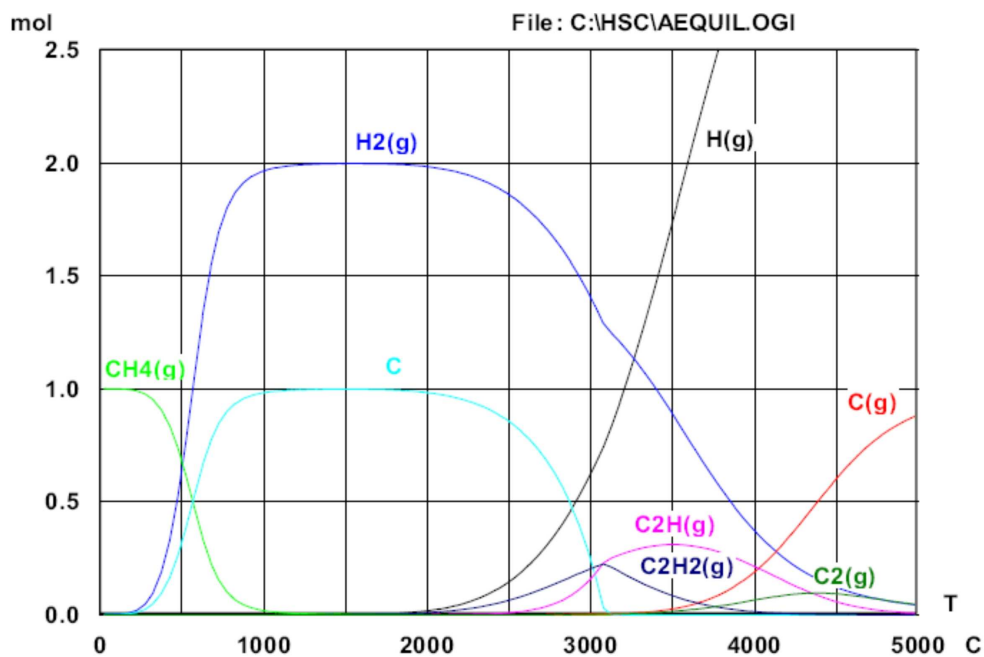


Figure 2.6: Methane pyrolysis products with solid carbon phase - adopted from [47].

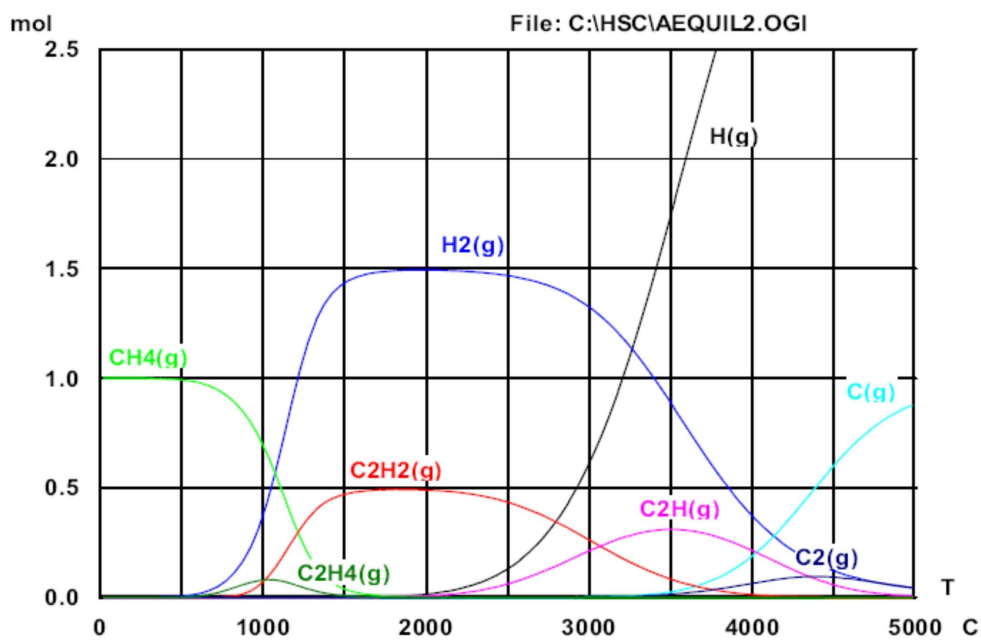
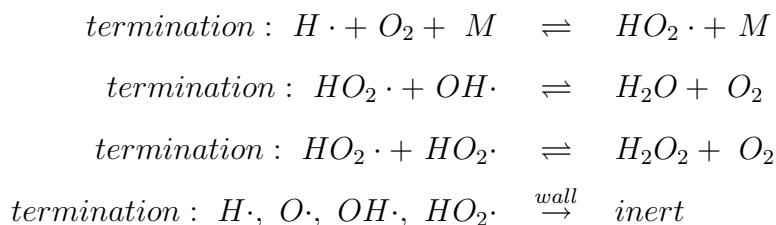


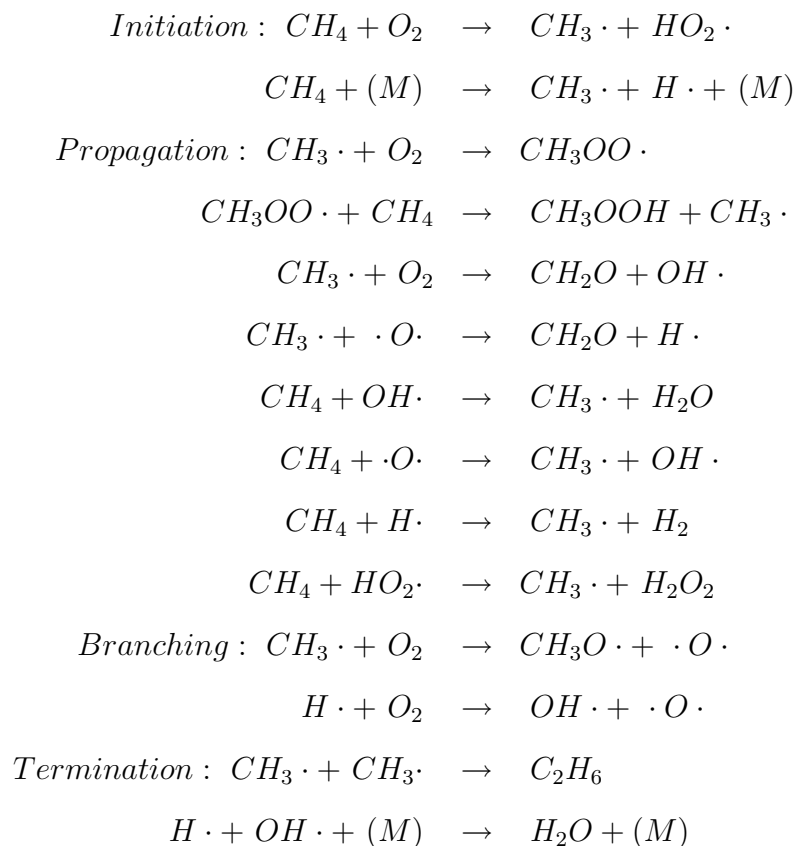
Figure 2.7: Methane pyrolysis products excluding solid carbon phase - adopted from [47].

The chain branching steps compete with a chain-terminating sequence of reactions, involving primarily:



The first termination reaction is actually a chain propagation but can be considered terminating as the $HO_2 \cdot$ radical is much less reactive than $H \cdot$, $O \cdot$ and $OH \cdot$ radicals.

As for methane pyrolysis, the methane combustion mechanism is too complex to reproduce it here. Several basic and important reactions for methane combustion are presented below:



In general the main gas phase radicals are $OH \cdot$, $HO_2 \cdot$, $CH_3 \cdot$ and $CH_3OO \cdot$ with $CH_3OO \cdot$ and $OH \cdot$ being the important chain carriers at temperature of only a few hundred K and $HO_2 \cdot$ being dominant above 1000 K [52]. As reviewed by Mackie [53]

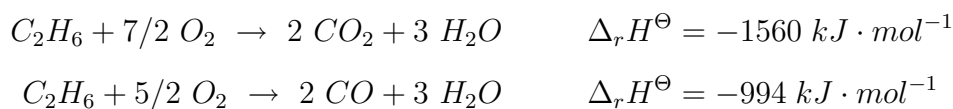
the nature of the methane oxidation products (coupling products, oxygenates or total oxidation products) is determined by the relative concentration of key radicals (e.g. $OH\cdot$, $H\cdot$, $HO_2\cdot$, $R\cdot$, $RO_2\cdot$) in the gas phase (R =organic fragment).

2.1.4 Interaction of Catalytic and Non-Catalytic Reactions in Methane Oxidation

As described above, heterogeneously catalyzed high temperature reactions are often insufficiently described by surface reaction steps only. In many cases surface and gas phase reactions can proceed in parallel and interact with each other by exchange of heat and/or exchange of reactive species.

Coupling by exchange of heat

Energetic coupling by exchange of heat is often observed during partial oxidation processes, where a large amount of reaction heat is produced and raises the temperature of the gas phase above the catalyst until gas phase reactions become possible. A technical process utilizing this is the dehydrogenation of ethane to ethylene over a platinum catalyst [54]. In a first step part of the ethane is oxidized over the catalyst, producing a lot of heat due to the exothermicity of these reactions:



The reaction heat increases the temperature of the gas phase above the catalyst and the homogeneous dehydrogenation of ethane to ethylene becomes feasible:

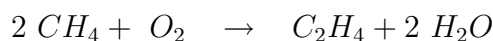


The authors of [54] state that ethylene is not produced heterogeneously, as the desorption step would be too slow compared to further dehydrogenation to surface carbon which in turn is oxidized to CO_2 . Contrary to this view Zerkle [55] showed, that the production of ethylene changes from nearly homogeneous for very lean mixtures to almost heterogeneous under very fuel rich conditions. This example illustrated that there is need in the understanding of coupling processes between catalytic (surface)

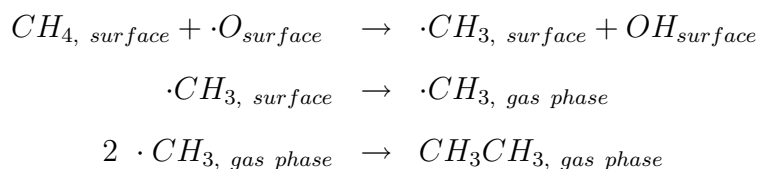
and non-catalytic (gas phase) reactions by heat exchange. This holds in particular for industrial processes where ignition of undesired gas phase reactions may lead to explosions [56].

Coupling by exchange of radicals - Radical desorption from the catalyst

A different kind of coupling between catalytic (surface) and non-catalytic (gas phase) reactions occurs via exchange of radicals. The oxidative coupling of methane to ethylene over lithium doped magnesium oxide is the prime example for this kind of coupling:



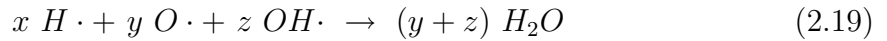
As discussed in Section 2.1.2, Lunsford et al. detected methyl radicals during this reaction using matrix isolation EPR spectroscopy [57]. The formation of C_2 coupling products could be correlated with the detection of methyl radicals in the gas phase, leading to the conclusion that ethane is formed via methyl radical recombination in the gas phase [20], followed by dehydrogenation to ethylene:



The release of reactive intermediates may occur under high temperature conditions also over other catalysts and for different gas mixtures. During methane CPO on noble metal catalysts gas phase reactions were found to reduce the selectivity to synthesis gas by about 2 % behind the catalyst at 1188 K and 1 MPa [12]. Unfortunately, the only radical species, which could be experimentally verified over *Pt* surfaces during reactions and tracked by simulations were $OH\cdot$ radicals [58]. Their experimental detection was accomplished by Laser Induced Fluorescence Spectroscopy but the simulations showed that these radicals were only formed by reactions in the gas phase. Contradicting results were reported by Marks and Schmidt [59] who showed that $OH\cdot$ radicals desorb from a *Pt* surface during catalytic combustion of various fuels.

Coupling by exchange of radicals - Radical losses at the catalyst

Radicals, participating in gas phase radical chain reactions, can also be destroyed at a surface, be it catalytic or inert. For example, the ignition temperature of hydrogen/air mixtures is higher over catalytically active surfaces compared to inert surfaces [60]. Depending on the species, produced gas phase radicals can diffuse to the wall and may become destroyed, e.g. by recombination to water [61] (Eq. 2.19):



The result of this radical scavenging is a zone directly above the catalytic surface, where no self accelerated reactions can occur. Its height depends on the radical species and its diffusivity. This might be the reason why non-catalytic gas phase reactions are not observed at pressures below 1 MPa on Pt coated reticulated foam catalysts which have pore sizes in the range of a few hundred μm [12].

The dependence of the rate of gas phase radical chain reactions on pressure is quite complicated. On the one hand, gas density increases with pressure leading to more intermolecular collisions compared to wall collisions. Radical generation and branching reactions are supported. On the other hand increasing pressure enhances also the number of three body collisions (Z) according to Eq. 2.20 [62] with N_1 , N_2 and N_3 denoting the concentrations of the three species and σ the binary collision cross sections.

$$Z = N_1 N_2 N_3 (4\pi\sigma_{1,2}^2) (4\pi\sigma_{2,3}^2) \delta \left[\sqrt{RT \frac{m_1 + m_2}{2\pi m_1 m_2}} + \sqrt{RT \frac{m_2 + m_3}{2\pi m_2 m_3}} \right] \quad (2.20)$$

As gas phase radical recombinations require a third collision partner to carry away excess kinetic energy chain terminating reactions become also more efficient at higher pressure [63].

2.2 Molecular Beam Threshold Ionization Mass Spectrometry

Chapter 2.2 introduces shortly the principles of molecular beams, their generation and their application for sampling of reactive intermediates from chemically reacting flows. The chapter finishes with a discussion of the mass spectrometric detection of gas phase radicals by threshold ionization and the quantitative analysis of threshold ionization data.

2.2.1 Molecular Beam Principles

A molecular beam is formed when a gas expands through a nozzle or orifice from a high pressure region into a low pressure background. The pressure conditions influence strongly the attributes of the molecular beam. Molecular beams can be classified by means of their Knudsen number in the orifice. The Knudsen number (Kn) describes the ratio of the mean free path of the molecules ($\bar{\lambda}$) to the geometric dimensions of the vessel, in this special case to the orifice diameter - d_n .

$$Kn = \frac{\bar{\lambda}}{d_n} \quad (2.21)$$

Knudsen numbers above 0.5 represent molecular flow regimes, where the mean free path of the molecules is larger than the orifice diameter. Beams produced in this region are called effusive beams. The directionality of effusive beams is determined by the collision of the molecules with the orifice walls rather than by collisions between the molecules. Knudsen numbers between 10^{-2} and 0.5 are called 'Knudsen type flows' and are rarely used. Knudsen numbers lower than 10^{-2} specify gas dynamic expansions where the directionality of the beam is determined by collisions between the molecules and the flow is driven by the pressure gradient.

The Maxwell mean free path $\bar{\lambda}$ [m] can be calculated by Eq. 2.22 from the collision cross section σ [m^2] and the particle density N [m^{-3}]:

$$\bar{\lambda} = \frac{1}{\sqrt{2} \cdot N \cdot \sigma} \quad (2.22)$$

Assuming ideal gases, the particle density can be calculated from temperature and pressure:

$$N = \frac{p}{kT} \quad (2.23)$$

If conditions typical for this work are inserted ($p = 101300 \text{ Pa}$, $T = 298 - 1573 \text{ K}$) and N_2 is assumed as probe molecule ($\sigma = 1.4 \cdot 10^{-19} \text{ m}^2$) the mean free path results to $2 \cdot 10^{-7} \text{ m}$ at 298 K and $1.1 \cdot 10^{-6} \text{ m}$ at 1573 K . The diameter of the sampling orifice of the system used in this work was about $125 \mu\text{m}$ leading to the following Knudsen numbers:

$$\begin{aligned} Kn_{298 \text{ K}} &= 1.6 \cdot 10^{-3} \\ Kn_{1573 \text{ K}} &= 8.8 \cdot 10^{-3} \end{aligned}$$

The flow regime is therefore always continuous.

If the pressure ratio between the high and the low pressure side $G = p_{high}/p_{low}$ is higher than the critical pressure ratio G^* given by Eq. 2.24, the particles in the molecular beam reach supersonic speed during the expansion:

$$G^* = \left(\frac{(\gamma + 1)}{2} \right)^{\frac{\gamma}{\gamma-1}} \quad (2.24)$$

In Eq. 2.24, $\gamma = C_p/C_v$ denotes the adiabatic exponent which is $\gamma = 7/5$ for diatomic ideal gases. Taking again N_2 as probe molecule G^* calculates to 1.9 and is in general for all types of gases smaller than 2.1 [64]. During this study the reactor was operated at atmospheric pressure ($p_{high} \approx 1000 \text{ mbar}$) and the expansion chamber was operated at about $p_{low} \approx 10^{-3} \text{ mbar}$. For this pressure ratio G calculates to 10^6 which is much larger than G^* . It can be concluded, that the used molecular beam in this work was always supersonic.

The structure of a supersonic gas expansion is shown in Figure 2.8 [65]. If the gas expansion behind the orifice is not restricted by any walls, as it was also the case in the present work, the term ‘free jet expansion’ is frequently used. During the expansion the particle density inside the beam decreases steeply and the molecules reach several times the speed of sound. At a certain distance from the orifice, the collisions of the beam molecules with the background gas molecules results in the formation of shock waves. The location of the formed mach disk (x_M), the shock

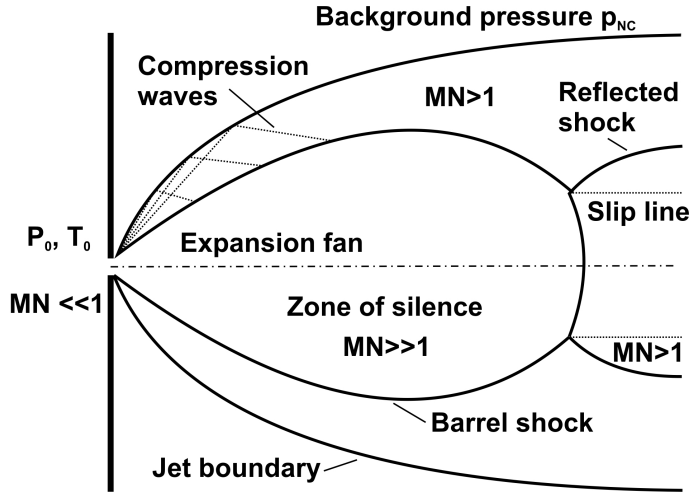


Figure 2.8: General structure of a supersonic free jet expansion with MN denoting the mach number - adopted from [65].

wave perpendicular to the expansion direction, can be calculated from Eq. 2.25 using $p_0 = 101300 \text{ Pa}$, $p_{NC} = 3 \cdot 10^{-1} \text{ Pa}$, $d_n = 125 \cdot 10^{-6} \text{ m}$:

$$x_M = d_n \cdot 0.67 \cdot \sqrt{\frac{p_0}{p_{NC}}} = 0.0487 \text{ m} \simeq 49 \text{ mm} \quad (2.25)$$

The Mach disk is therefore located 49 mm downstream the orifice. The thickness of the mach disc (and also of the barrel shocks) is approximately 0.5 to 0.75 times the mach disk distance [65] - about 30 mm . This implies that there is no real shock wave structure formed in the expansion chamber of the MBMS used in this work rather than a slow change in the beam attributes.

The molecular beam itself is formed in this work by cutting out the center part of the expansion using an arrangement of two differentially pumped metal cones termed skimmer and collimator (Fig. 2.9).

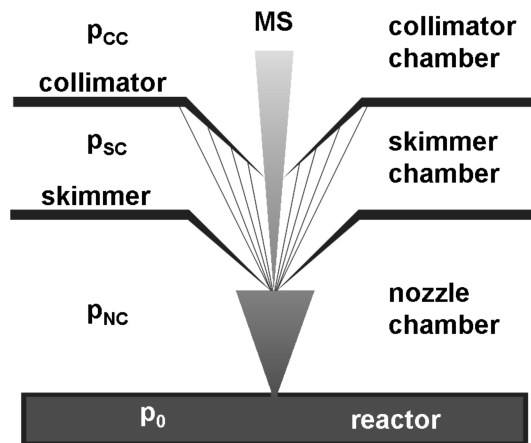


Figure 2.9: Sketch of the formation process of the molecular beam with a combination of skimmer and collimator cone in a three stage differentially pumped vacuum system.

2.2.2 Molecular Beam Characterization

The adiabatic expansion of molecules into a vacuum background leads to intermolecular collisions and to the exchange of energy between the molecules. In general, undirected translation energy (thermal energy) is transformed into directed translation in beam direction. As long as the mean free path is small compared to the wall distances intermolecular collisions occur and energy is exchanged. Along the expansion coordinate the intermolecular collision frequency drops and at a certain position virtually no intermolecular collisions occur anymore. This is called the quitting surface of the system. The lowest temperature of the expanded gas is defined by the Mach number reached during expansion up to the quitting surface. The maximal reachable Mach number can be calculated using Eq. 2.26 [66]:

$$MN_{max} = \sqrt{\left(\frac{2}{\gamma - 1}\right) \left[\left(\frac{p_0}{p_1}\right)^{\frac{\gamma-1}{\gamma}} - 1\right]} \quad (2.26)$$

For argon with an adiabatic exponent $\gamma = 5/3$ and for nitrogen with $\gamma = 7/5$ this results in $MN_{max} = 27.4$ and $MN_{max} = 16$ respectively.

The ratio between the temperature upstream the expansion orifice (T_0) and somewhere in the expansion (T_1) is related to the Mach number at this point by Eq. 2.27 [67]:

$$\frac{T_0}{T_1} = 1 + \frac{\gamma - 1}{2} \cdot MN^2 \quad (2.27)$$

For example, if T_0 corresponds to a reactor temperature of $1300 \text{ }^\circ\text{C} = 1573 \text{ K}$, Eq. 2.26 and 2.27 can be used to calculate the final temperature of the beam constituents. If values for *Ar* are inserted ($\gamma = 5/3$, $MN_{max} = 27.4$) the *Ar* atoms can be theoretically cooled down to $1573 \text{ K}/250 \text{ K} \approx 6.3 \text{ K}$.

Up to the quitting surface the temperatures parallel and perpendicular to the beam are equal, as energy can be exchanged by collisions. Behind this point no collisions take place, the speed of the molecules remains constant and the temperature parallel to the beam does not change anymore. The temperature perpendicular to the beam decreases further, as the geometric spherical expansion continues with a maximum rate proportional to r^{-2} . The average temperature behind the quitting surface will therefore be somewhat lower than the one calculated by Eq. 2.27.

The position of the quitting surface can be estimated as the distance at which the continuum expansion reaches the maximum Mach number MN_{max} . For axisymmetric

expansions at distances larger than 0.5 orifice diameters, the dependence of the Mach number on the distance from the orifice can be calculated from a correlation such as the one shown in Eq. 2.28 [68]:

$$MN = \left(\frac{x}{d}\right)^{\gamma-1} \cdot \left[C_1 + \frac{C_2}{(x/d)} + \frac{C_3}{(x/d)^2} + \frac{C_4}{(x/d)^3} \right] \quad (2.28)$$

If the constants $C_1 - C_4$ for monoatomic and diatomic gases are inserted ($C_1 = 3.232$, $C_2 = -0.7563$, $C_3 = 0.3937$, $C_4 = -0.0729$ and $C_1 = 3.606$, $C_2 = -1.742$, $C_3 = 0.9226$, $C_4 = -0.2069$ respectively [68]) the position of the quitting surface can be calculated. For Ar with $MN_{max} = 27.4$ and N_2 with $MN_{max} = 16$ the (x/d) values calculate to 24 and 40 respectively. As the adiabatic exponent becomes smaller for larger molecules it can be assumed that the distance of the quitting surface is always smaller than $(x/d = 80)$. In the present work an orifice with a diameter of 0.125 mm was used which translates into a quitting surface distance for Ar and N_2 of 3 mm and 5 mm respectively. To sample always behind the quitting surface where all relaxation processes are terminated, the skimmer was placed in all experiments at a distance of 10 mm from the orifice.

According to Fenn [69] each molecule experiences on average 1000 collisions during the expansion. Because relaxation of translational and rotational degrees of freedom require only about 1 and 100 collisions respectively they will be fully relaxed up to the quitting surface. Vibrations on the other hand require on average 1000000 collisions to relax and will therefore be frozen but not relaxed at the quitting surface.

Of particular importance for the present work is that heavier species tend to enrich along the center of a molecular beam whereas lighter species tend to move outwards [70]. This particularity makes molecular beams interesting for species separation [71] but imposes severe limitations on their applicability as a sampling tool simply because the beam composition at the place of analysis does not represent the composition of the sampled gas mixture. Several effects may be responsible for this separation phenomenon and an understanding of these effects is necessary if data quantification is required.

Four separation effects are discussed in the literature. The most effective mechanism is the separation due to pressure diffusion [72]. During the expansion process the pressure drops very steeply over the first few nozzle distances. The lighter species

are accelerated more strongly transverse to the beam than heavier species and will therefore become depleted in the beam center.

The second effect, leading to a mass separation, is molecular diffusion [73]. Assuming the same mean velocity for the heavier and the lighter gas species, the lighter ones have a larger thermal velocity spread in all directions. Their diffusion perpendicular to the beam is therefore faster than that of the heavier compounds leading again to their depletion in the beam center.

Thirdly, skimmer shock separation leads also to an increase of the heavier components [74] in the beam center. As the skimmer represents a barrier, a shock wave is formed at the skimmer entrance. Heavier components can easier penetrate this shock wave due to their higher kinetic energy. In the present work, skimmer induced separation is probably of minor importance as the background pressure was with 10^{-3} mbar too low to form a distinct shock wave structure.

The fourth effect known as background gas penetration [75] has the opposite sign and can increase the concentration of lighter gas species in the beam center. Background gas penetration can become important if the particle density in the molecular beam is not much higher than in the vacuum background. In this case, background gas molecules will diffuse into the beam, lighter ones faster than heavier ones leading to an enrichment of the first.

For the conditions used in the present work, enrichment of heavier species in the beam center clearly dominates. Greene et al. [72] conducted an extensive experimental study on mass separation effects in molecular beam sampling of gas mixtures at atmospheric pressure. Firstly, the authors calibrated their mass spectrometer at low pressures using pure components. Secondly, diluted multi-component mixtures were sampled from atmospheric pressure by means of a molecular beam and the calculated signals from the partial pressures and the beforehand determined sensitivities were compared to the experimentally obtained signals. To quantify the mass separation effects the authors calculated for each solute-solvent combination an enrichment factor α using (Eq. 2.29):

$$\alpha = \frac{\left(\frac{\text{calculated signal}}{\text{observed signal}}\right)_{\text{component}}}{\left(\frac{\text{calculated signal}}{\text{observed signal}}\right)_{\text{solvent}}} \quad (2.29)$$

As can be seen from Fig. 2.10 there is indeed a strong enrichment of heavier species

in the molecular beam with respect to N_2 which was the solvent in these experiments. If the values reported in Fig. 2.10 are applied to the mixtures that have been

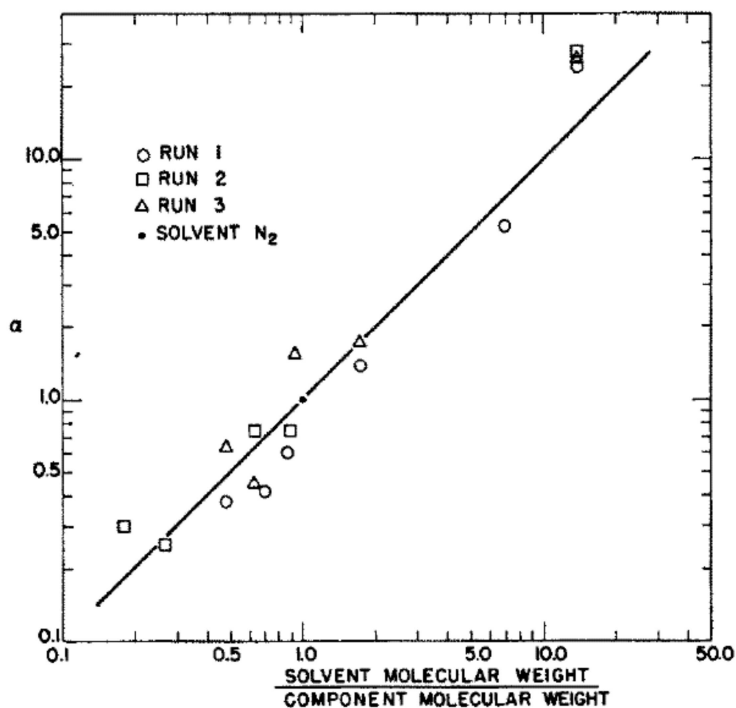


Figure 2.10: Mass separation factors α of various compounds diluted in nitrogen.

investigated in the present work with mean molar masses between $18 - 22 \text{ g} \cdot \text{mol}^{-1}$ (cf. Chapter 4) it can be expected that the concentration of H_2 and He will be underestimated by a factor of 2 – 3 whereas CO_2 will be overestimated by a factor of 2.

In summary, mass separation effects in molecular beam sampling have to be taken into account but can be minimized by using low background pressures and a skimmer with sharp edges and small cone angle. Furthermore the mass spectrometer signals should be calibrated with sample mixtures of similar molar mass as the mixtures to be analyzed.

2.2.3 Molecular Beam Applications

Molecular beams are frequently used tools in science. In UHV experiments, molecular beams provide excellent conditions for studying adsorption, desorption and reaction processes on model surfaces. Whereas high particle densities can be realized in a molecular beam and at the sample surface, the surrounding vacuum chamber still

achieves UHV conditions [76]. By stepwise adsorption of two reactants [77] or two crossed molecular beams [78] basic atomic and kinetic parameters can be determined. The cooling properties of molecular beams are used in molecular physics for high resolution spectroscopy. A third field of application to which also the current work belongs to is molecular beam sampling of chemically reacting systems at pressures in the *mbar* to *bar* range (e.g. flames [79], plasmas [80], reactors [66, 81]). Here the molecular beam enables quenching of highly reactive species such as radicals (cooling rates up to $10^8 \text{ K} \cdot \text{s}^{-1}$) and provides an interfaces between the high pressure application and a mass spectrometer which requires high vacuum for operation.

2.2.4 Threshold Ionization Mass Spectrometry

Mass spectrometry of free radicals relies on the selective ionization of the radicals in presence of a number of interfering species [82]. Generally, gas ionization can be achieved with a variety of methods such as chemical ionization, photoionization or electron impact ionization. Whereas the extent of molecular fragmentation is low for the former two methods (soft ionization) electron impact leads to strong molecular fragmentation and is therefore considered a hard ionization method.

During this work electron impact ionization (EI) was used. As the name implies, electrons of sufficient energy collide in this ionization method with the gas molecules and expel electrons from their valence orbitals (Eq. 2.30):



As the ionization process is very fast, the ionized molecules are left in a state of high potential energy leading to secondary bond breaking. As an example a mass spectrum of butane is shown in Fig. 2.11 obtained with an ionization energy of 70 eV [83]. The energy of 70 eV is often chosen, as the cross section for the electron impact ionization has its maximum between 50 eV and 150 eV for most species [84]. Figure 2.12 shows how the total ionization cross section varies as function of the ionization energy for *He*, *N₂* and *CH₄*.

The aim of this work was to identify and quantify gas phase radicals in a large excess of interfering background molecules. As an example relevant to methane

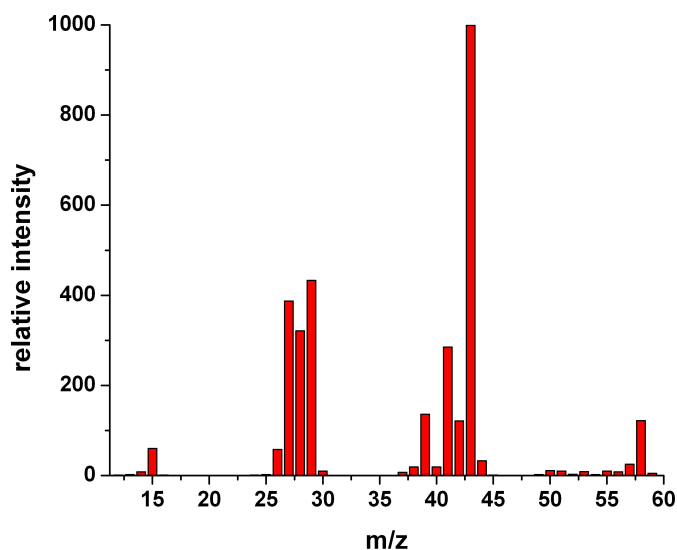


Figure 2.11: Electron impact ionization mass spectrum of butane, showing strong fragmentation (the molpeak at $m/z = 58$ amu has only small intensity) - adopted from [83].

oxidation and oxidative coupling, the problem of how to detect methyl radicals $CH_3\cdot$ at $m/z = 15$ amu in presence of the interfering molecules CH_4 and C_2H_6 is illustrated in Figure 2.13. As can be seen, the signal of CH_3^+ ions resulting from ionization of $CH_3\cdot$ radicals overlaps on mass $m/z = 15$ amu with the signal of CH_3^+ ions from methane and ethane fragmentation. As the latter two are reactant and product respectively and have orders of magnitude higher concentrations than the reactive $CH_3\cdot$ radicals, the signal at 15 amu will be dominated by contributions from methane and ethane fragmentation. Consequently, a specific detection of $CH_3\cdot$ radicals using the standard ionization energy of 70 eV would be impossible.

The method of threshold ionization for the detection of radicals takes advantage of the difference between the ionization potential of the radical of interest and the appearance potentials of interfering fragment ions. The appearance potential of an ion A^+ formed by dissociation of a molecule AB is always higher than the ionization potential of the corresponding radical A namely by the amount of the dissociation enthalpy of the $A - B$ bond (Eq. 2.31) [82]:

$$AP(A^+/AB) = IP(A) + \Delta_d H(A - B) \quad (2.31)$$

Applied to the system $CH_3\cdot / CH_4 / C_2H_6$ this translates into Eqs. 2.32-2.33:

$$AP(CH_3^+/CH_4) = IP(CH_3\cdot) + \Delta_d H(H_3C - H) \quad (2.32)$$

$$AP(CH_3^+/C_2H_6) = IP(CH_3\cdot) + \Delta_d H(H_3C - CH_3) \quad (2.33)$$

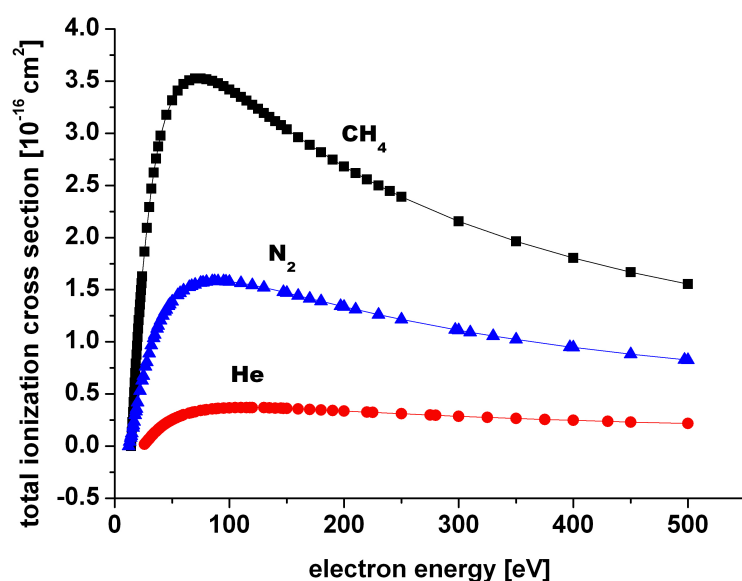


Figure 2.12: Total electron ionization cross sections for He , N_2 and CH_4 as function of the electron energy - the maximum is observed between 50 eV and 150 eV .

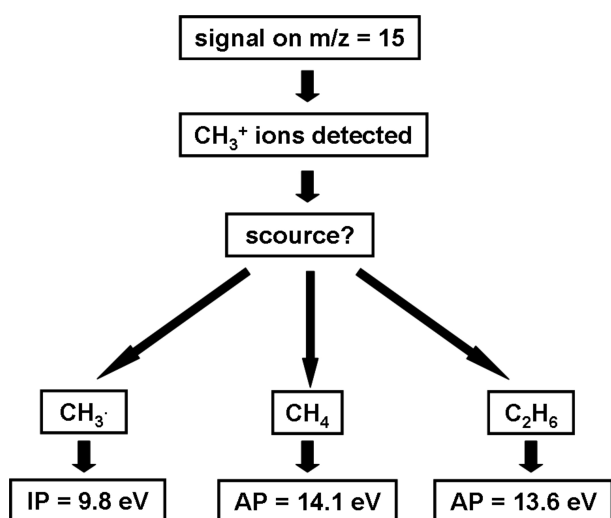


Figure 2.13: Possible sources of the signal at $m/z = 15$ amu , either by ionization of the sought $CH_3\cdot$ radicals or by fragmentation of other molecules like CH_4 and C_2H_6 .

The bond energies lie in the range of about 4 eV for $C-H$ bonds and 3 eV to 4 eV for $C-C$ bonds. If the energy of the ionizing electrons is now selected higher than the IP of the radical, but lower than all AP 's of interfering fragment ions it is possible to detect the radical selectively even in large excess of the interfering molecules. This technique is called threshold ionization. In Fig. 2.14 the measurement of methyl radicals in excess of methane is shown. The energy of the ionizing electrons was varied and the peak area of the $m/z = 15$ amu peak was measured. The onset of ionization at about 10 eV corresponds to the IP of methyl radicals, whereas the change in slope at about 14 eV corresponds to methane fragmentation.

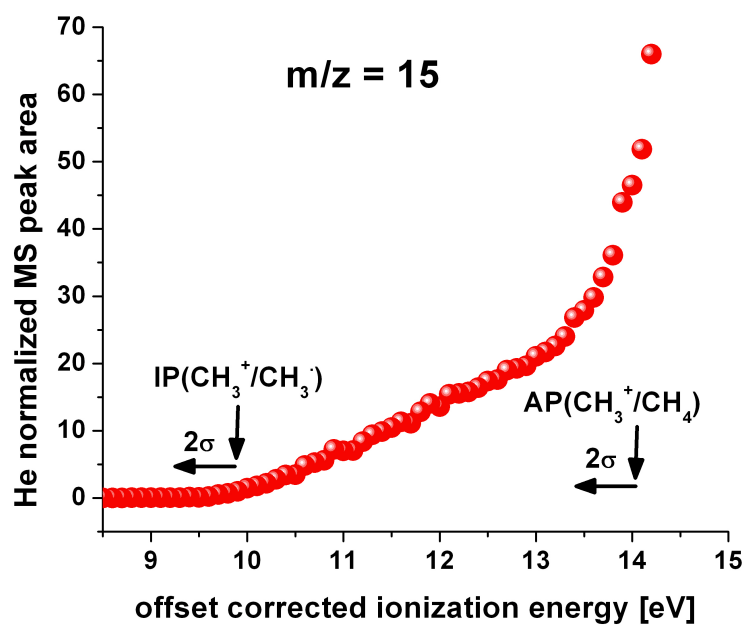


Figure 2.14: Threshold ionization measurements of methyl radicals in an excess of methane - additionally the IP of the radical and the AP from methane fragmentation are shown.

Part III

Experimental

Chapter 3

Experimental

3.1 Molecular Beam Mass Spectrometry

Molecular Beam Mass Spectrometry (MBMS) is a dedicated method to detect and quantify highly reactive species, e.g. radicals, in chemically reacting flow environments. It has been used in the past to detect radicals in flames [79, 85], plasmas [86] and CVD applications [87]. In the current work, the MBMS technique has been adapted to sample, detect and quantify gas phase radicals from a high temperature catalytic wall reactor in which the catalytic partial oxidation of methane is conducted at atmospheric pressure.

The setup was build to connect a catalytic wall reactor to a threshold ionization mass spectrometer. The three stage pumped vacuum system ensures on the one hand a stabilization of reactive intermediates, arising from the reactor, by supersonic expansion and on the other hand a pressure lowering by ten orders of magnitude (atmospheric pressure inside the reactor to 10^{-7} *mbar* at the mass spectrometer). A detailed description of the design and the physical principle of the MBMS is given in the following Sections 3.1.1-3.1.4.

3.1.1 Reactor

The heart of the catalytic wall reactor placed in the main vacuum chamber of the MBMS is a 100 *mm* long platinum tube with an inner diameter of 4.4 *mm* and

an outer diameter of 5.0 mm (wall thickness 0.3 mm) (Fig. 3.1). The tube ends are conically shaped (2°) and fit gas tightly into two copper clamps which hold the reactor in place, compensate for length changes due to thermal expansion and provide electrical contact for resistive heating of the tube. For the investigated stoichiometries ($\dot{V}_{CH_4}/\dot{V}_{O_2} = 1.2 - 4.0$), the methane catalytic oxidation on *Pt* starts between $500^\circ C$ and $600^\circ C$ and after ignition, the reactor can be operated autothermally or with additional electrical heating. With heating powers up to 350 W, temperatures of $1300^\circ C$ could be reached. At $1300^\circ C$, losses due to platinum vaporization [88] or formation of volatile oxides [89] are still insignificant. However, the copper clamps had to be water cooled to avoid melting and oxidation of the *Pt/Cu* interface. Resistive heating of the *Pt* tube was only possible because of its small length. As stainless steel, from which all connections to the reactor were made (water and gas supplies), has an electric conductivity similar to *Pt*, all connections had to be significantly longer than the *Pt* tube itself to minimize their resistive heating (≥ 500 mm):

$$Pt = 9.71 \cdot 10^6 \text{ S} \cdot \text{m}^{-1} \text{ [90]}$$

$$Fe = 10.6 \cdot 10^6 \text{ S} \cdot \text{m}^{-1} \text{ [90]}$$

The three stainless steel mounting rods (Fig. 3.2, number 2) which were of the same length as the *Pt* tube were electrically isolated from the copper clamps.

To quench and stabilize reactive gas phase species for mass spectrometric analysis, a small fraction of the reacting mixture inside the *Pt* tube was expanded from reactor pressure ($1000 \text{ mbar} \leq p_r \leq 1200 \text{ mbar}$) through a small sampling orifice in the tube wall into a vacuum background ($\leq 5 \cdot 10^{-3} \text{ mbar}$). An orifice diameter between

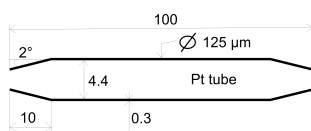
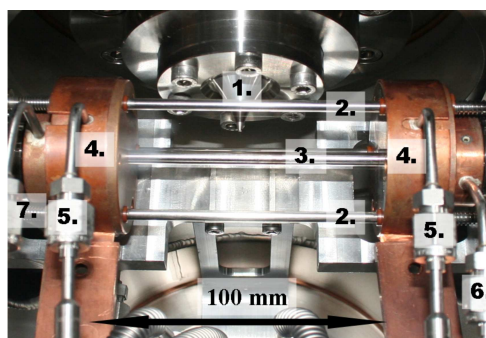


Figure 3.1: Shape and dimensions of the *Pt* reactor tube.



1. skimmer cone
2. mounting rods
3. Pt reactor tube
4. copper clamps
5. cooling water
6. gas out
7. gas in

Figure 3.2: Picture of high temperature tubular catalytic wall reactor in the main vacuum chamber of the MBMS.

100 μm and 125 μm was found to be a good compromise between strong signals (large diameters) and available pumpage in the vacuum chamber. The orifices were manufactured by laser drilling (Frey GmbH, Berlin), giving excellent wall smoothness as shown in Fig. 3.3.

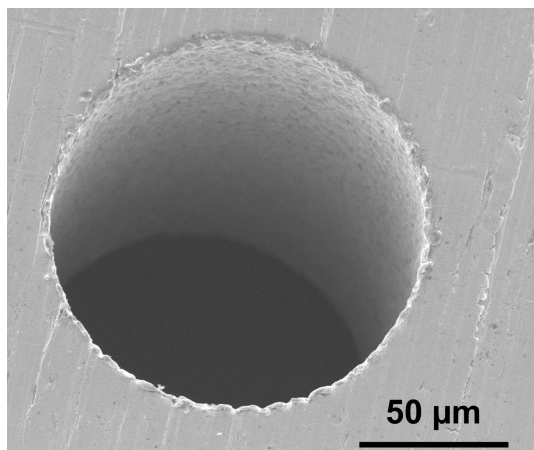


Figure 3.3: *Laser drilled orifice for molecular beam sampling from the high temperature tubular flow reactor (tilted by 15 ° for wall view).*

3.1.2 Vacuum System

A pressure reduction from 10^3 mbar (reactor pressure) to about 10^{-7} mbar (operating pressure for the mass spectrometer) is hardly achievable within one step. As shown in Fig. 3.4, a differentially pumped three stage vacuum system consisting of sampling orifice, skimmer cone and collimator cone was used to achieve ten orders of magnitude pressure reduction and to form the molecular beam. A picture of the MBMS is shown in Figure 3.5.

The first vacuum chamber, henceforth called reactor chamber, contained the reactor. It was evacuated by a large turbomolecular pump (TMU 1601 PCH Pfeiffer ($1400 \text{ l} \cdot \text{s}^{-1} \text{ N}_2$)), as the gas discharge into the reactor chamber was high (cf. calculations in Chapter 4, Section 4.1.1) and the pressure had to be kept below 10^{-2} mbar to avoid shock wave formation behind the sampling orifice which would disturb the molecular beam (cf. Section 2.2.1).

A skimmer cone, located about 10 mm above the reactor orifice, cut out the centerline of the free jet expansion to form a molecular beam. The vacuum chamber above the skimmer (henceforth called skimmer chamber) was evacuated by a smaller turbomolecular pump (TMU 261 - Pfeiffer). Finally, a collimator cone, located above

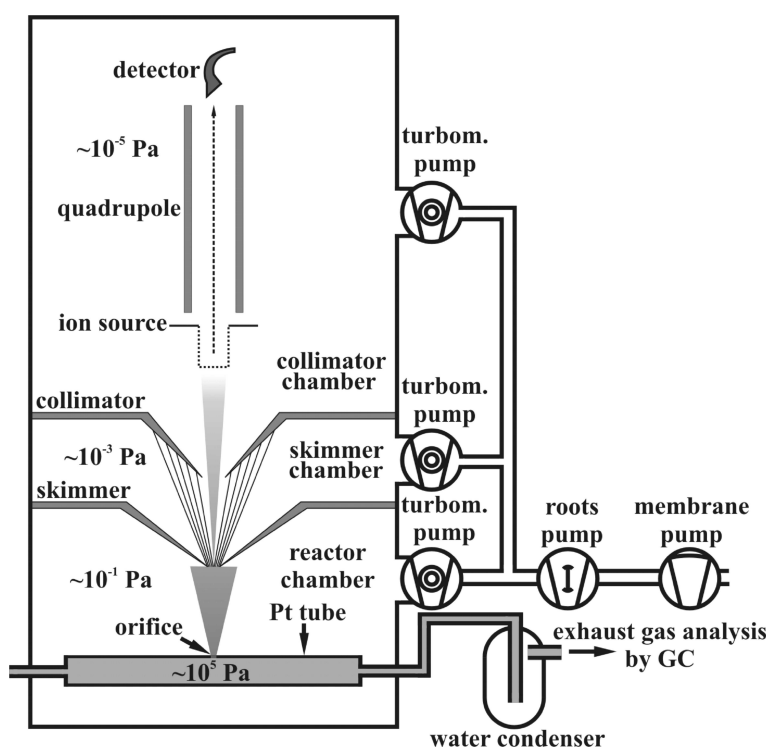
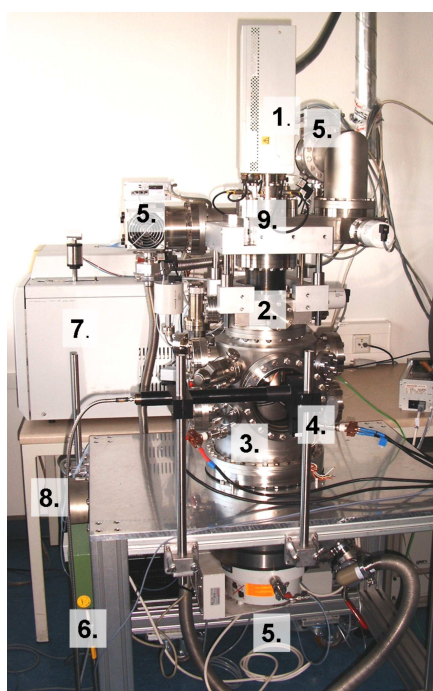


Figure 3.4: Sketch of the experimental setup to measure gas phase radicals in the catalytic partial oxidation of methane.



1. Mass spectrometer electronics
2. Skimmer chamber
3. Reactor chamber
4. Pyrometer scanner
5. Turbomolecular pump
6. Pyrometer electronics
7. Gas chromatograph
8. Reactor pressure gauge
9. Collimator chamber with MS

Figure 3.5: Picture of the experimental setup to measure gas phase radicals in the catalytic partial oxidation of methane.

the skimmer reduced the pressure to a value where the mass spectrometer could be operated. This vacuum chamber, henceforth called collimator chamber, was also pumped by a smaller turbomolecular pump (TMU 261 - Pfeiffer). All three turbomolecular pumps were pre-pumped by a strong oil-free booster pump with $35 \text{ m}^3 \cdot \text{h}^{-1}$ (RP35C Vario - Vaccumbrand). Using this three stage differentially pumped sampling systems, the following pressures were achieved under operation:

$$\begin{aligned} p_{\text{reactor}} &= \textit{between 1000 and 1200 mbar} \\ p_{\text{reactor chamber}} &= 5 \cdot 10^{-3} \textit{ mbar} \\ p_{\text{skimmer chamber}} &= 5 \cdot 10^{-5} \textit{ mbar} \\ p_{\text{collimator chamber}} &= 5 \cdot 10^{-7} \textit{ mbar} \end{aligned}$$

Pressures were measured with Pirani gauges at the booster pump and with cold cathode gauges in all three vacuum chambers. Another Pirani gauge was used at the reactor chamber to follow shutdown and start up of the vacuum system.

3.1.3 Mass Spectrometer

The quadrupole mass spectrometer used in the MBMS was a HIDEN HAL IV EPIC Low Energy, from Hiden Analytical Limited, UK. The mass spectrometer was equipped with an ionizer designed for molecular beam inlet and threshold ionization, a triple quadrupole mass filter for masses up to 510 amu and an electron multiplier as detector. For threshold ionization experiments full mass spectra were measured at increasing electron energies but at constant electron current in the ionizer.

3.1.4 Pyrometer

Temperature measurements are conducted with optical pyrometry. The usage of a thermocouple turned out to be impractical, as it allows only measuring one single spot. Essential for the data analysis is the knowledge about the complete profile, which helps to identify reaction zones.

The following theory, describing the basic principles of pyrometry / ratio pyrometer, is taken from Müller and Renz [91].

The spectral radiation energy of a black body is given by Planck's law:

$$E_{\lambda,b}(T) = \frac{C_1}{\lambda^5 [\exp(C_2/\lambda T) - 1]} \quad (3.1)$$

With C_1 and C_2 : Planck's radiation constants; λ : wavelength; T : absolute temperature of the black body.

For values of $\lambda \cdot T$ lower than $3125 \mu m \cdot K$ Wien's approximation can be used with an error less than 1 %. The pyrometer wavelength in this study is about $1.6 \mu m$, at maximum used temperatures of $1573 K$. Therefore $\lambda \cdot T$ is about $2500 \mu m \cdot K$ and the approximation valid, resulting in Eq. 3.2:

$$E_{\lambda,b}(T) = \frac{C_1}{\lambda^5 [\exp(C_2/\lambda T)]} \quad (3.2)$$

This formula can be used to derive the measured signal $I_\lambda(T)$ of a radiation pyrometer at a distinct wavelength:

$$I_\lambda(T) = \frac{K \epsilon_\lambda}{\lambda^5 \exp(C_2/\lambda T)} \quad (3.3)$$

With ϵ_λ is the monochromatic emissivity of the measured object, K a pyrometer specific geometric constant.

Unfortunately, the emissivity of platinum changes with temperature [92], but ratio pyrometry eliminates this problem. Using two wavelength close to each other, equals the emissivity, and therefore also its changes. The true object temperature T is connected to the measured pyrometer temperature T_R by the ratio of the intensities according to:

$$T_R = \left(\frac{1}{T} + \frac{\ln(\epsilon_1/\epsilon_2)}{C_2(\lambda_2^{-1} - \lambda_1^{-1})} \right)^{-1} \quad (3.4)$$

As λ_1 , λ_2 and C_2 are constant and $\epsilon_1 = \epsilon_2$ the object temperature is only dependent from the measured by a constant factor k , that contains these values. The pyrometer has to be calibrated only once. Simultaneously several additional effects, as the non uniform reflectivity of the mirror and the adsorption by the glass window, can be corrected by using the complete setup during calibration.

During this work temperature profiles of the Pt reactor tube were measured by contact free ratio pyrometry. In a ratio pyrometer, the radiative power is measured at two wavelengths close to each other ($1.52 \mu m$ and $1.64 \mu m$) and the temperature is calculated from the ratio of these two measurements which eliminates the emissivity

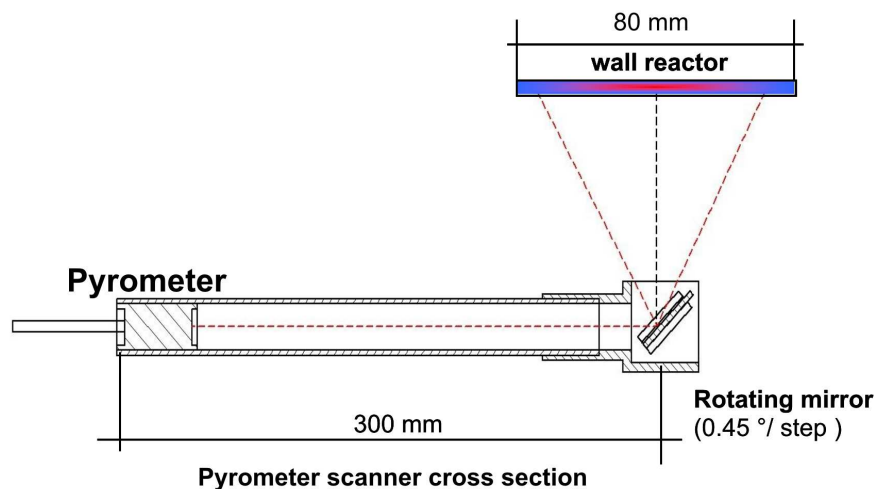


Figure 3.6: Sketch of the pyrometer setup including a 0.45° stepper motor for an effective spatial resolution of 4 mm on the platinum tube.

dependence of the measurement. Fig. 3.6 shows a sketch of the pyrometer setup. The pyrometer optic has a focus length of 600 mm and the measurement spot is scanned along the tube by a rotating mirror mounted on a stepper motor with $0.45^\circ/\text{step}$. This translates into tube temperature profiles with a spatial resolution of 4 mm , just slightly larger than the spot diameter of about 3 mm .

3.2 Gas Supply and Reactor Off-Gas Analysis

All gases were supplied from Westfalen (O_2 purity 5.0, CH_4 purity 3.5, Ar purity 5.0, He purity 5.0, N_2 purity 5.0). The feed gases were dosed and mixed by mass flow controllers (Bornkhorst Hi-Tech). The reactor off-gases were analyzed by gas chromatography. For the development of the analytical method the following problems had to be solved. Firstly, separation and detection of H_2 , CO_2 , CO , N_2 , and O_2 was necessary. Secondly $C_1 - C_4$ aliphatic hydrocarbons and benzene had to be separated and detected. To accomplish these tasks, two columns, a Hayesep A and a Molsieve column, were used in the GC according to the flow scheme shown in Fig. 3.7. The final GC method comprised four steps which are explained in the following:

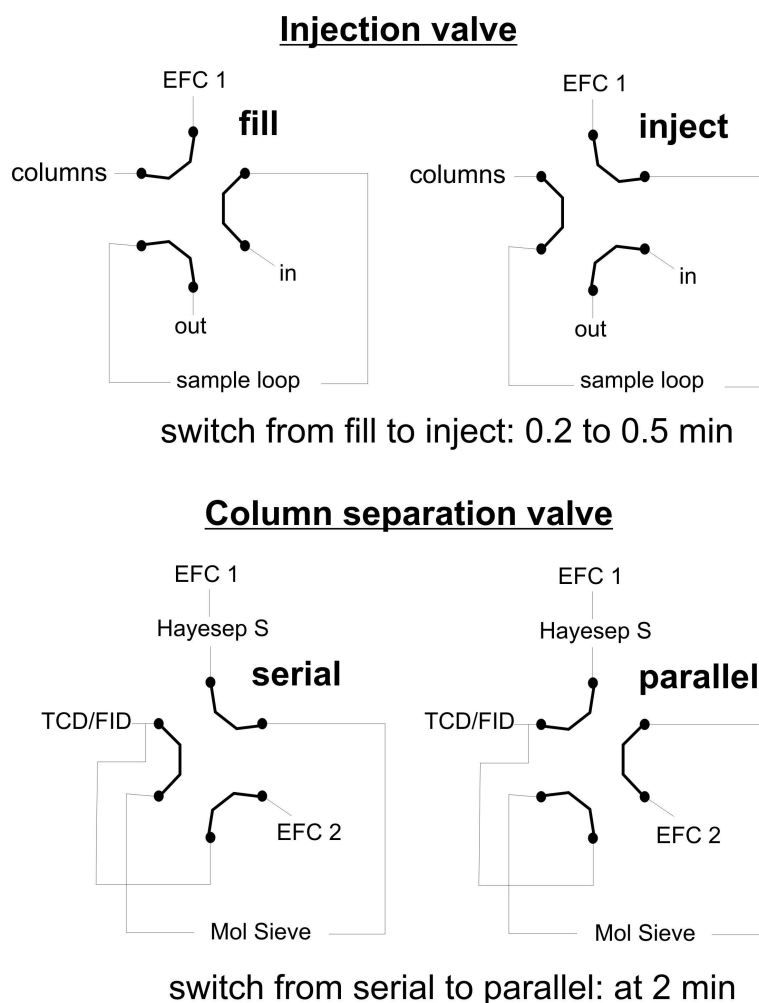


Figure 3.7: GC gas flow and switch scheme.

fill (Fig. 3.7a): The first 0.2 *min* of each GC run were used to allow for measurement of a baseline. As a small fraction of the reactor off-gas stream was permanently flowing through the sample loop of the GC, these first 0.2 *min* were also necessary to make sure that the sample loop contained a representative sample after changing reactor conditions.

inject (Fig. 3.7b): After 0.2 *min* filling time, the injection valve was switched to direct the He flow from EFC1 through the sample loop, injecting the sample loop content into the chain of columns (Hayesep S followed by Molsieve). This injection period lasted 0.3 *min*. At 0.5 *min* the injection was finished and the injection valve turned back into the fill position.

serial (Fig. 3.7c): At the beginning of the separation process (0.5 *min*), all gases

entered at first the Hayesep S column where the hydrocarbons and CO_2 were retained whereas the inert gases, CH_4 , O_2 , H_2 and CO passed through quickly and entered the Molsieve column. This part of the separation process lasted from 0.5 – 2 *min*.

parallel: After 2 *min*, the column separation valve was switched so that now Hayesep S and the Molsieve column operate in parallel. The flow of the *He* carrier through the Molsieve column was provided by the electronic flow controller 2. The effluents of both columns were connected to two detectors in series; firstly a thermal conductivity detector (TCD) and secondly a flame ionization detector (FID). O_2 , H_2 , CO and CO_2 were detected with the TCD detector and all hydrocarbons were detected with the FID detector. The latter measures the ion density in a clean hydrogen flame, which increases drastically when hydrocarbons are burned in the flame. O_2 , H_2 and CO , which had passed through the Hayesep S without separation were now separated in the Molsieve column, whereas all hydrocarbons were separated in the Hayesep S.

To demonstrate the viability of the above described GC method, a test mixture with C1 to C6 alkanes, C2 to C4 alkenes, CO_2 , CO , N_2 , O_2 and H_2 was analyzed. Fig. 3.8 shows the FID and Fig. 3.9 the TCD detector signal.

As can be seen, all C2 and C3 hydrocarbons as well as H_2 , CO_2 , O_2 and CO are well separated. From the five different C4 species only four could be separated, but as nearly no C4 are expected during the reaction, this compromise could be made. Water elutes in a very broad and poorly reproducible peak, which makes the peak unsuitable for quantitative analysis. As the GC columns can be damaged by operation in strong hydrous atmospheres (column bleeding), water was removed before analysis by passing the reactor effluent stream through a condenser operated at 15 °C leading to about 1 Vol% to 3 Vol% residual water in the gas stream. For quantification water was calculated from the oxygen or hydrogen balance. Due to the use of packed columns, the time for one GC analysis was with about 25 *min* comparably long, in particular because of *benzene*, which will elute from the column in the C6 region. However, using packed columns ensured a more robust system in comparison to capillary columns in terms of contaminations and stability against water.

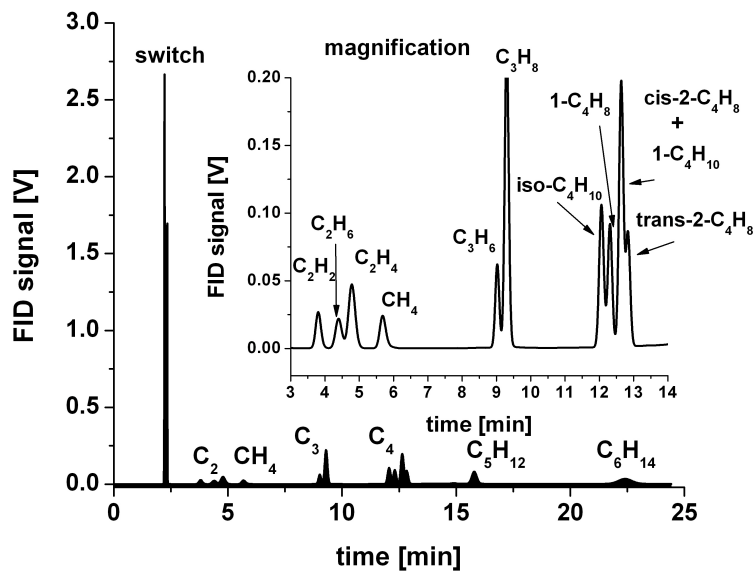


Figure 3.8: FID signal of the hydrocarbons for the GC separation efficiency demonstration.

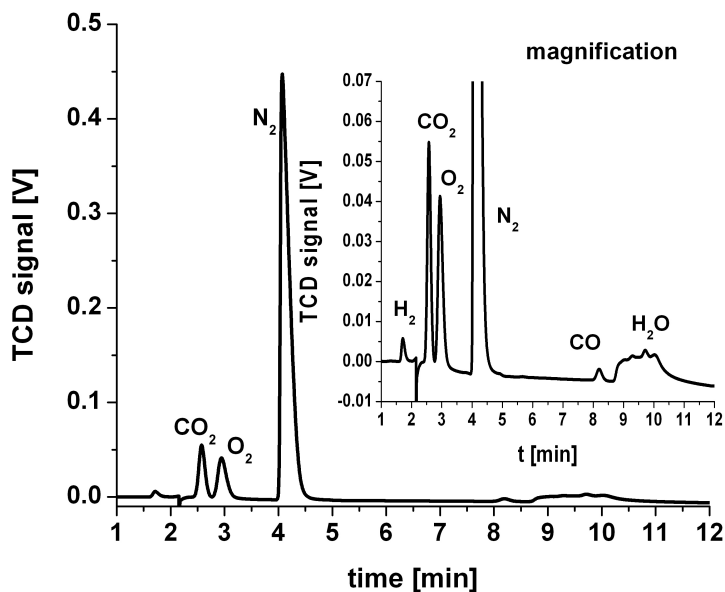


Figure 3.9: TCD signal of main compounds for the GC separation efficiency demonstration.

Part IV

Results & Discussion

Chapter 4

Results and Discussion

Chapter 4 will focus on experimental results and their discussion. After presenting important key data of the experimental setup showing performance and limits of the MBMS system, experiments on the catalytic partial oxidation of methane on Pt are presented and discussed.

4.1 Key Data of the Experimental Setup

4.1.1 Gas Flow through Orifice

The orifice represents a significant ‘leak’ inside the reactor vacuum chamber, and adequate pumping is necessary to maintain low pressures inside the nozzle chamber. According to Horn et al. [93] the first pumping stage was designed to maintain the pressure in the reactor chamber under operation below $4 \cdot 10^{-3}$ mbar, to avoid shock wave formation in front of the orifice.

Secondly, the reactor inlet gas flow must be much higher than the loss through the orifice, otherwise a stable flow profile can not develop inside the reactor and the sampling process will disturb the reaction. The mass flux j_m in $kg/(m^2 \cdot s)$ through the sampling orifice calculates for a frictionless flow according to Equation 4.1 [94]:

$$j_m = \rho \cdot v = -\frac{dp}{dv} = p_0 \left(\frac{2\gamma}{\gamma - 1} \frac{\bar{M}}{RT_0} \left[\left(\frac{p}{p_0} \right)^{\frac{2}{\gamma}} - \left(\frac{p}{p_0} \right)^{\frac{1+\gamma}{\gamma}} \right] \right)^{\frac{1}{2}} \quad (4.1)$$

In Eq. 4.1, p_0 corresponds to the pressure inside the reactor, p to the pressure in the reactor vacuum chamber, \bar{M} is the mean molar mass of the gases inside the reactor, T_0 the reactor gas temperature, $\gamma = C_p/C_v$ the adiabatic exponent and R the universal gas constant.

It can be shown that by decreasing p , j_m reaches a maximum value j_m^* at $p/p_0 < 0.5$ which calculates to [94]:

$$j_m^* = \rho^* \cdot v^* = p_0 \left(\frac{2}{\gamma + 1} \right)^{\frac{1}{\gamma-1}} \left(\frac{2\gamma}{\gamma + 1} \frac{\bar{M}}{RT_0} \right)^{\frac{1}{2}} \quad (4.2)$$

In the free jet expansion from the reactor into the reactor vacuum chamber p/p_0 approaches 0, hence, the mass flux through the orifice can be calculated by Eq. 4.2 and the mass-, molar- and volumetric flow rates (\dot{q}_m , \dot{F} and \dot{V} respectively) by Eqs. 4.3-4.5:

$$\dot{q}_m = j_m^* \cdot \frac{\pi}{4} d_n^2 \quad (4.3)$$

$$\dot{F} = \frac{\dot{q}_m}{\bar{M}} \quad (4.4)$$

$$\dot{V} = \dot{F} \cdot \frac{RT_0}{p_0} \quad (4.5)$$

Exemplarily, the flow of He through the reactor orifice with diameter d_n at room temperature and atmospheric pressure can be calculated for the following values:

$$d_n = 100 \cdot 10^{-6} \text{ m}$$

$$p_0 = 101300 \text{ Pa}$$

$$\gamma = 5/3 \approx 1.67$$

$$\bar{M} = 0.004 \text{ kg} \cdot \text{mol}^{-1}$$

$$R = 8.314 \text{ J} \cdot \text{mol}^{-1} \cdot \text{K}^{-1}$$

$$T_0 = 298 \text{ K}$$

with the results

$$j_m^* = 93.5 \text{ kg} \cdot \text{m}^{-2} \cdot \text{s}^{-1} \quad (4.6)$$

$$\dot{q}_m = 7.34 \cdot 10^{-7} \text{ kg} \cdot \text{s}^{-1} \quad (4.7)$$

$$\dot{F} = 1.84 \cdot 10^{-4} \text{ mol} \cdot \text{s}^{-1} \quad (4.8)$$

$$\dot{V} = 4.49 \cdot 10^{-6} \text{ m}^3 \cdot \text{s}^{-1} = 270 \text{ ml} \cdot \text{min}^{-1} \quad (4.9)$$

For comparison, the volumetric flow rate \dot{V} was also determined experimentally. Without an inlet gas flow and an opened reactor outlet to atmosphere, air was sucked into the reactor and nitrogen and oxygen were present in the molecular beam. When *He* was fed to the reactor N_2 and O_2 stayed detectable as long as the volumetric flow rate through the orifice was greater than the *He* inlet volumetric flow rate. \dot{V}_{He} corresponds then to the volumetric *He* flow rate, at which neither nitrogen nor oxygen were detected anymore. The results of this experiment are presented in Fig. 4.1.

The initial increase of the N_2 and O_2 signals up to $100 \text{ ml} \cdot \text{min}^{-1}$ reflects the initially decreasing mean molar mass of the gas mixture \bar{M} , as $\dot{V} \propto \bar{M}^{-1/2}$ (cf. Eqs. 4.2 and 4.5). Even though the mole fractions of N_2 and O_2 decrease, the absolute molecular flow through the nozzle increases and with that the N_2 and O_2 signals. Additionally, the enrichment of heavier gases in a mixture of light and heavy species may have an effect (cf. Section 2.2.2). From $150 \text{ ml} \cdot \text{min}^{-1}$ *He* flow on the mass scans were started above 4 amu to avoid overflow of the detector as the *He* signal got too intense. As can be seen in Fig. 4.1, about $250 \text{ ml} \cdot \text{min}^{-1}$ *He* are needed to remove the air signals which is in good agreement with the calculated value of flows $270 \text{ ml} \cdot \text{min}^{-1}$, facing the fact that the simplifying assumption of frictionless flow was made. Calculations at 1573 K show, that the flow of *He* through the nozzle is reduced to $3.197 \cdot 10^{-7} \text{ kg} \cdot \text{s}^{-1}$, meaning by a factor of 2.3.

To calculate the gas losses through the sampling orifice under reaction conditions, a typical gas mixture during a methane CPO experiment is assumed. Table 4.1 lists the species, their corresponding mole fractions taken from Section 4.2.1 and their degrees of freedom f , as well as the resulting adiabatic exponent γ . With $\bar{M} = \sum X_i M_i$ and $\bar{\gamma} = \sum X_i \gamma_i$ the nozzle gas flow is only $50 \text{ ml} \cdot \text{min}^{-1}$, corresponding to standard conditions. The inlet volume flow is about $1000 \text{ ml} \cdot \text{min}^{-1}$ (STP), therefore only 5% of the reactive flow is lost through the nozzle. During the experiment changes in temperature are only in the range between 1273 K and 1573 K , mean molar mass changes are between $0.018 \text{ kg} \cdot \text{mol}^{-1}$ (1573 K with high hydrogen selectivity) and $0.022 \text{ kg} \cdot \text{mol}^{-1}$ (1273 K , high CO_2 and water selectivity). Within these limits, the nozzle loss is always below 6 % and the disturbance of the gas flow inside the reactor tube by the sampling process can be neglected.

Table 4.1: Possible degrees of freedom for the main gas components at 1573 K

| vibration | deg. | $\tilde{\nu}/\text{cm}^{-1}$ | Θ_v | excited | f_T | f_R | f_v | f_{total} | γ |
|---|------|------------------------------|------------|------------|-------|-------|-------|-------------|----------|
| <i>CH₄ [X = 0.037]</i> | | | | | | | | | |
| <i>sym. str.</i> | 1 | 2917 | 4196.9 | <i>no</i> | | | | | |
| <i>deg. deform.</i> | 2 | 1534 | 2207 | <i>no</i> | 3 | 3 | 0 | 6 | 8/6 |
| <i>deg. str.</i> | 3 | 3019 | 4343.7 | <i>no</i> | | | | | |
| <i>deg. deform.</i> | 3 | 1306 | 1879 | <i>no</i> | | | | | |
| <i>CO₂ [X = 0.047]</i> | | | | | | | | | |
| <i>deg. deform.</i> | 2 | 667.5 | 960.4 | <i>yes</i> | | | | | |
| <i>sym. str.</i> | 1 | 1388.4 | 1997.6 | <i>no</i> | 3 | 2 | 2 | 7 | 9/7 |
| <i>anti. str.</i> | 1 | 2350.1 | 3381.3 | <i>no</i> | | | | | |
| <i>H₂O [X = 0.296]</i> | | | | | | | | | |
| <i>sym. str.</i> | 1 | 3657 | 5261.7 | <i>no</i> | | | | | |
| <i>deform.</i> | 1 | 1595 | 2294.9 | <i>no</i> | 3 | 3 | 0 | 6 | 8/6 |
| <i>anti. str.</i> | 1 | 3756 | 5404.1 | <i>no</i> | | | | | |
| <i>CO [X = 0.208]</i> | | | | | | | | | |
| <i>str.</i> | 1 | 2143 | 3083.3 | <i>no</i> | 3 | 2 | 0 | 5 | 7/5 |
| <i>H₂ [X = 0.298]</i> | | | | | | | | | |
| <i>str.</i> | 1 | 4380 | 6301.9 | <i>no</i> | 3 | 2 | 0 | 5 | 7/5 |
| <i>C₂H₂ [X = 0.027]</i> | | | | | | | | | |
| <i>CH str.</i> | 1 | 3374 | 4854.5 | <i>no</i> | | | | | |
| <i>CC str.</i> | 1 | 1974 | 2840.2 | <i>no</i> | | | | | |
| <i>CH str.</i> | 1 | 3289 | 4732.2 | <i>no</i> | 3 | 2 | 4 | 9 | 11/9 |
| <i>CH bend.</i> | 2 | 612 | 880.5 | <i>yes</i> | | | | | |
| <i>CH bend.</i> | 2 | 730 | 1050.3 | <i>yes</i> | | | | | |
| <i>He [X = 0.088]</i> | | | | | | | | | |
| | | | | | 3 | 0 | 0 | 3 | 5/3 |

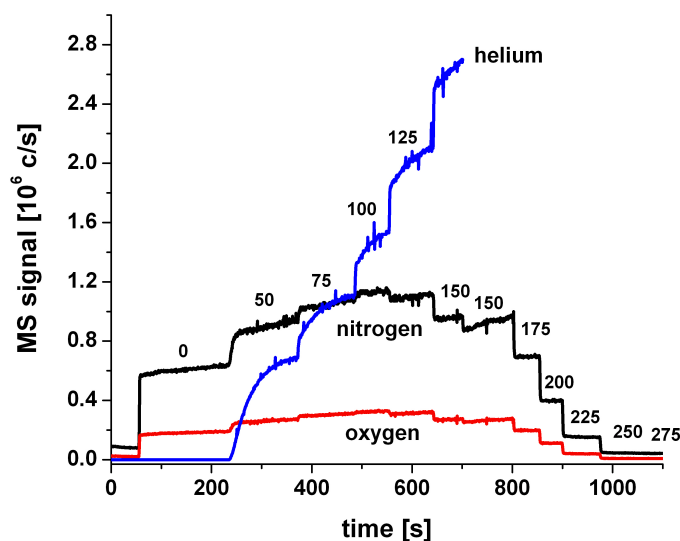


Figure 4.1: Determination of the He volumetric flow rate through the sampling orifice.

4.1.2 Enrichment of Heavier Species in the Molecular Beam Center

As described in Section 2.2.2, there are processes both in the free jet expansion and the molecular beam formation that tend to enrich heavier species in the centerline of the molecular beam altering the sample composition in the ionizer with respect to the reactor tube. As a numerical prediction of these effects is difficult, experiments with sample mixtures were conducted to study their influence on the current application.

In a first experiment, a mixture of $450 \text{ ml} \cdot \text{min}^{-1} He$ ($M = 4 \text{ g} \cdot \text{mol}^{-1}$) and $50 \text{ ml} \cdot \text{min}^{-1} Ar$ ($M = 40 \text{ g} \cdot \text{mol}^{-1}$) was used. The profile of the free jet expansion and the separation effects were studied by shifting the orifice horizontally in steps of 0.1 mm with respect to the skimmer. With orifice and skimmer perfectly aligned, sampling from the centerline of the free jet expansion occurs, whereas a shift between orifice and skimmer leads to sampling from outer regions of the expansion. These measurements were performed at four different temperatures ($25 \text{ }^\circ\text{C}$, $600 \text{ }^\circ\text{C}$, $1000 \text{ }^\circ\text{C}$ and $1300 \text{ }^\circ\text{C}$). To study the profile of the free jet expansion, the total pressure in the collimator chamber was plotted against the relative shift between orifice and skimmer whereas separation effects are revealed by plotting the Ar and He MS signals and

most importantly the Ar/He signal ratio versus shift positions. The results are shown in Figure 4.2.

Fig. 4.2 *I.* shows that the profile of the free jet expansion is flat near the centerline but drops steeply if $y/d > 0.2$, with y being the displacement between orifice and skimmer. This results is in good agreement to literature [95]. It can also be seen that the expansion becomes narrower with increasing temperature in the reactor tube. Furthermore, the measurements presented in Fig. 4.2 *I.* are of practical merit as they indicate that it is very easy to position the orifice underneath the skimmer by using the collimator chamber pressure as indicator.

The changes in the MS signals of both gas components are shown in Fig. 4.2 *II.* and Fig. 4.2 *III.* Indeed, the beam profile of the lighter component He is wider than that of Ar . He , which is present in the mixture in large excess ($X_{He} = 0.9$) behaves as can be expected from Eq. 4.2, i.e. the signal decreases with increasing temperature ($F \propto (T_0)^{-1/2}$). Contrary to He , the Ar signal levels out at temperatures higher than $600\text{ }^\circ C$ which can be attributed to an enrichment of Ar in He with temperature.

The enrichment factor, which is reflected by the Ar/He peak ratio 4.2 *IV.* depends on both, temperature and displacement between orifice and skimmer. Between $25\text{ }^\circ C$ and $1300\text{ }^\circ C$ the Ar/He peak ratio increases from 0.8 to 1.6, i.e. by a factor of 2. The variation with displacement is less pronounced. At $1300\text{ }^\circ C$, the enrichment factor increases only by about 15 % going from 0.3 mm to -0.3 mm displacement.

From the results presented in Figure 4.2 it can be concluded that the enrichment of heavier species occurs in the sampling process but that its influence on the signal intensities can be minimized by performing the calibration procedure at a temperature close to the measurement temperature and by sampling the free jet expansion from the plateau region of the free jet expansion. For a real measurement the enrichment effect will be further reduced as the enrichment factor, according to Dun et al. [96], - increases in first approximation linearly with the ratio of the molecular weight. The average molecular mass of the mixture under reaction conditions is between $18\text{ g}\cdot\text{mol}^{-1}$ and $22\text{ g}\cdot\text{mol}^{-1}$. Hence, the enrichment effect can be neglected for species with molecular masses in the range CH_4 to C_2H_6 as long as the calibration is performed at about $1000\text{ }^\circ C$. Only for relatively light and heavy gases (H_2 and CO_2 respectively) enrichment or depletion can become significant.

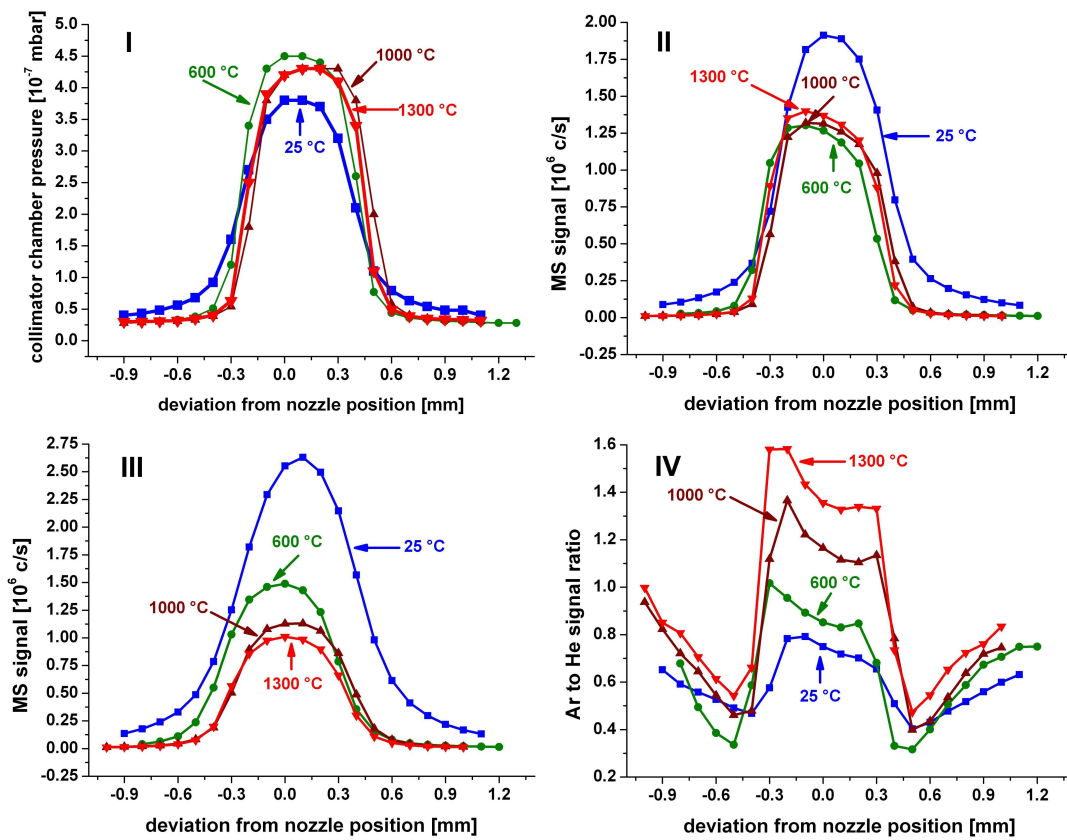


Figure 4.2: Orifice-skimmer shift experiments with $50 \text{ ml} \cdot \text{min}^{-1}$ Ar and $450 \text{ ml} \cdot \text{min}^{-1}$ He at four different temperatures: I. total pressure dependency; II. Axial MS signal of Ar; III. Axial MS signal of He; IV. Axial Ar to He ratios.

In a second experiment the temperature dependence of the enrichment factor for a real mixture was simulated by using a sample gas with the following composition:

$$\begin{aligned} N_2 &= 1100 \text{ ml} \cdot \text{min}^{-1} \text{ for e.g. } CH_4, H_2O, CO, O_2 \\ He &= 200 \text{ ml} \cdot \text{min}^{-1} \text{ for e.g. } H_2, He \\ Ar &= 50 \text{ ml} \cdot \text{min}^{-1} \text{ for e.g. } CO_2, Ar \end{aligned}$$

The temperature was changed in the following order:

$$25 \text{ }^\circ\text{C} \rightarrow 1034 \text{ }^\circ\text{C} \rightarrow 731 \text{ }^\circ\text{C} \rightarrow 25 \text{ }^\circ\text{C} \text{ (for reproduction)}$$

The resulting MS intensities are shown in Fig. 4.3. Normalizing these data to either *Ar* or *He*, results in a maximum deviation of 15 % in the temperature range between 25 °C and 1034 °C. The deviation is expected to be much lower in the temperature region from 1000°C to 1300°C, after performing the calibration at 1000°C.

4.1.3 Offset and Energy Spread of the Mass Spectrometer

To analyze threshold ionization data, offset and energy spread of the ionizing electrons have to be determined. Fig. 4.4, taken from Reference [97], presents threshold ionization data of various noble gases, which have been measured using a system designed and optimized for electron impact cross section measurements. Fig. 4.5 shows for comparison threshold ionization data measured with the used instrument employing an electron impact ionizer without additional energy filtering of the ionizing electrons. As can be seen without further analysis, the onset of the ionization curve in Fig. 4.5 is not sharp as in Fig. 4.4 but rather rounded in consequence of a convolution between the true ionization efficiency curve $P_i(E)$ and the Gaussian electron energy spread of the ionizing electrons in the ionizer [8].

When using a heated filament as electron source the energy of the ionizing electrons after acceleration is:

$$E = U + V \quad (4.10)$$

V denotes the applied potential and U any ill defined energy contributions. As the filament glows, one contribution to U is thermal energy. According to Honig [98] the thermal energy spread can be expressed by a Maxwellian distribution - Eq. 4.11

$$dN_e(U) = \frac{4 \cdot \pi \cdot m \cdot A}{h^3} U \exp\left(-\frac{\Phi + U}{kT}\right) dU \quad (4.11)$$

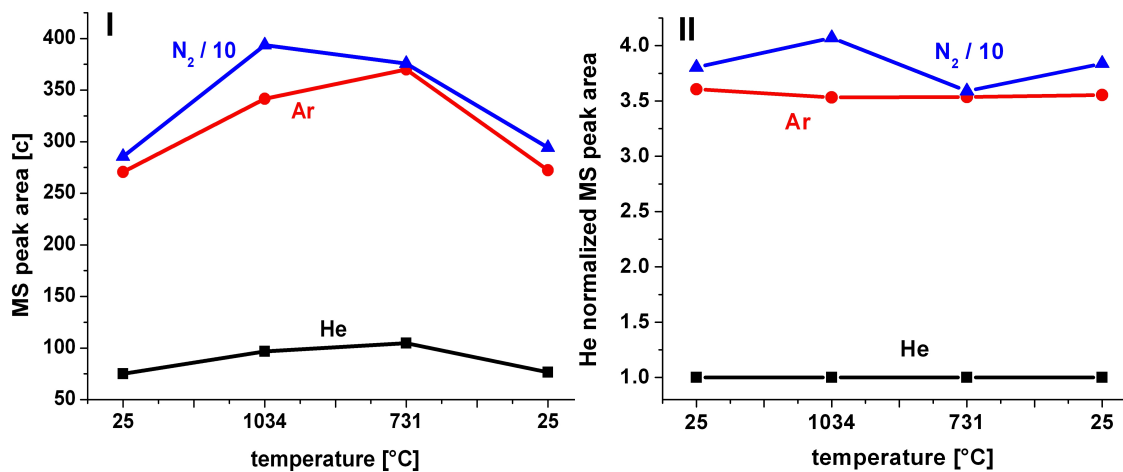


Figure 4.3: Temperature dependent MS signal evolution of a mixture of 50 ml · min⁻¹ Ar, 200 ml · min⁻¹ He and 1100 ml · min⁻¹ N₂: I. visible temperature effect on raw data; II. nearly no enrichment effect on He normalized data.

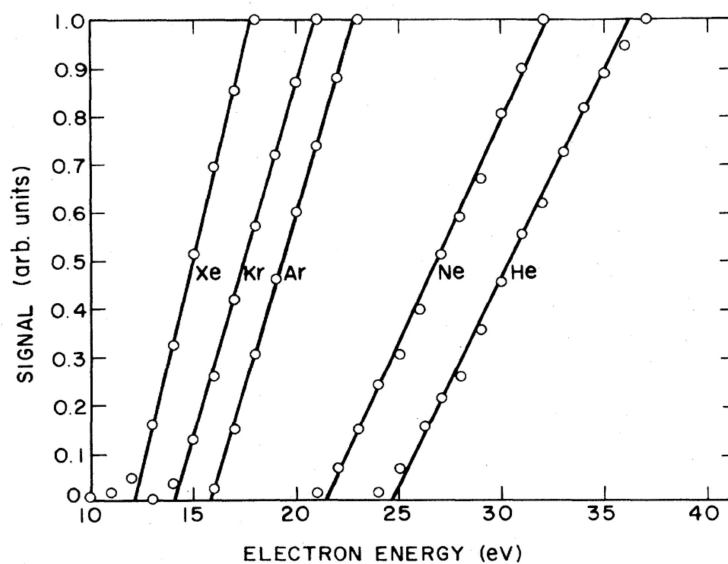


Figure 4.4: Rare gas electron ionization curves near the threshold - adopted from [97].

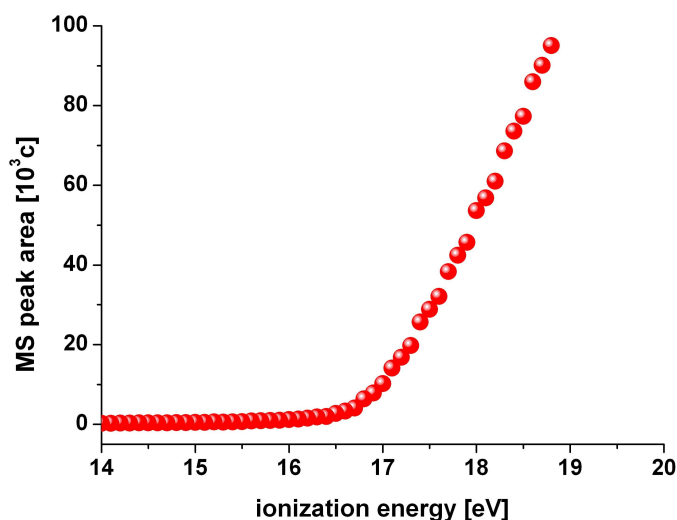


Figure 4.5: Electron ionization data of pure *Ar* near the threshold, obtained with the used Mass Spectrometer in this work.

where $dN_e(U)$ denotes the number of electrons of energies between U and $U + dU$ per sec, U the thermal energy of electrons, m the electron mass, A the surface area in cm^2 and Φ the work function of the filament. If temperature gradients exist along the heated filament the thermal energy spread becomes more complicated as T becomes a function of position.

More important than thermal energy contributions to U are probably potential gradients inside the source which can be expressed by a Gaussian type spread function,

$$m(U) = \frac{1}{\sigma \cdot \sqrt{2\pi}} \cdot \exp\left(-\frac{U^2}{2\sigma^2}\right) \quad (4.12)$$

where U denotes the energy of the electrons and σ the standard deviation. Additional contributions to U are potential drops along the filament, filament contaminations and contact potential between filament and source chamber. Together with the work function of the filament Φ , the latter effects contribute also to the observed energy offset [99]. As a consequence of above discussion it is very difficult to calculate energy spread and offset but it will be shown in the following that these parameters can be determined experimentally.

The single ionization of atoms close to the threshold can be approximated by

Wannier's threshold law [100] Eq. 4.13:

$$P_i(E) = C \cdot (E - IP)^{1.127} \quad E \geq IP \quad (4.13)$$

Later Geltman showed [101], that the exponent in Eq. 4.13 corresponds roughly to $n - 1$, with n being the number electrons involved in the ionization process. In photoionization for example, $n = 1$ because the electron is removed by interaction of an atom with a photon. Hence, as $n - 1 = 0$, the cross section for photoionization at the threshold is a step function. For single ionization by electron impact, two electrons are involved, $n = 2$, $n - 1 = 1$ and the ionization cross section increases linearly from the ionization potential on. For double ionization by electron impact, $n = 3$, $n - 1 = 2$ and a quadratic threshold law is expected.

Different procedures have been described to determine energy spread and offset experimentally, most of them are based on single ionization of light elements. If electron impact is used, as in the present work, the linear part above the threshold can be extended until it intersects the energy axis. The point of intersection corresponds then to the ionization potential (method used by e.g. Koffel [102]). This method works in some cases [103] but in the majority of cases it gives erroneous results [98]. A more sophisticated method was described by Morrison [104]. He showed mathematically that the second derivative of the measured ionization efficiency returns the electron energy spread function, reflected about the vertical axis.

In the present work, the second derivative was only used to determine the shape of the electron spread function. The results show that the electron energy spread follows a Gaussian distribution (Fig. 4.6, right panel) with a maximum at 16.8 eV and a standard deviation of 0.32 eV.

The numerical values of energy offset and spread were determined by fitting Eq. 4.14 directly to the threshold data, as smoothing, necessary for calculating the derivatives from the experimental data, would have increased the energy spread determined from the second derivative.

$$i(V) = \frac{C}{\sigma\sqrt{2\pi}} \sum_{j=0}^{\infty} \text{Exp} \left(-\frac{(IP + j \cdot \Delta E - V)^2}{2\sigma^2} \right) \cdot (j \cdot \Delta E)^{1.127} \cdot \Delta E \quad (4.14)$$

Using the literature ionization potential of Ar, the energy offset of the mass spec-

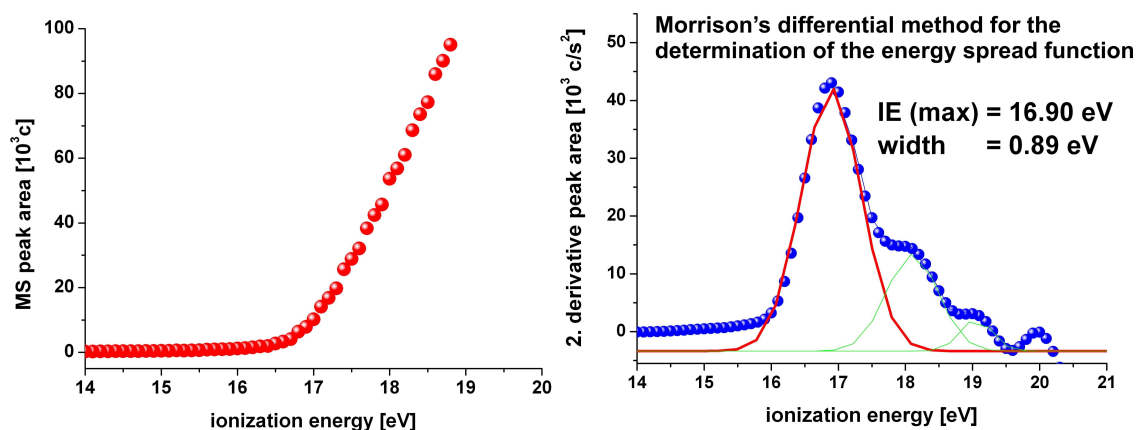


Figure 4.6: Electron Ionization MS peak areas of *Ar* next to the threshold and the resulting 2nd derivative - giving information about peak shape, energy spread and offset of the MS.

trometer results to:

$$\textit{literature value} = 15.8 \text{ eV} \quad [97]$$

$$\textit{measured IP} = 16.8 \text{ eV}$$

$$\textit{energy of fset} = 1.0 \text{ eV}$$

With respect to the energy spread, the 2σ criterion is applied as it describes an interval $IP(AP) \pm 2\sigma$, in which 95 % of the electrons have their energy. The threshold ionization measurements of the internal standard *Ar* have been repeated for different reaction conditions. On average, the electron energy offset was found to be 1.1 eV and the energy spread $\sigma = 0.31$ eV. Accordingly all experimentally determined ionization potentials of atoms and molecules in the sections below will be specified as:

$$IP(\textit{species}) = IP(\textit{measured}) - \textit{offset} \pm 2\sigma = IP(\textit{measured}) - 1.1 \text{ eV} \pm 0.62 \text{ eV} \quad (4.15)$$

The stability of the offset and energy spread can be demonstrated by a comparison to values, calculated using the same mass spectrometer in 2003 [93]. The offset was found to be 1 eV and the energy spread $\sigma = 0.3$ eV, in very good agreement with the now measured values. The only noticeable influence onto these data has the filament and its undefined state of contamination. In the very first minutes of operation the mass spectra changes slightly as a result of the changing work function of the filament. The actual experiment was started after at least 30 min of

filament stabilization. Consequentially from the data analysis no changes, neither in the MS signal intensities, nor in the onset of the threshold ionization data for the internal standards (*Ar* or *He*) were observed after stabilization for the complete set of experiments.

4.1.4 Quantification of Radicals by Threshold Ionization

The method of radical quantification in a mass spectrometer by threshold ionization is based on the work of Singh et. al. [105]. The radicals are quantified by reference to an ion, which is the product of a direct ionization process rather than being generated by fragmentation and which lies very close in mass to the radical ion (e.g. CH_4^+ for the ion CH_3^+ generated from the methyl radical $CH_3\cdot$).

The detector signal of any ion in the mass spectrometer depends on a variety of variables:

$$\frac{A^{CH_3\cdot \rightarrow CH_3^+}}{A^{CH_4 \rightarrow CH_4^+}} = \frac{\beta(CH_3^+) \cdot t(15amu) \cdot \Theta(15amu) \cdot l_{cage} \cdot I_e \cdot \lambda^{CH_3\cdot \rightarrow CH_3^+} \cdot n_{CH_3\cdot}^{ionizer}}{\beta(CH_4^+) \cdot t(16amu) \cdot \Theta(16amu) \cdot l_{cage} \cdot I_e \cdot \lambda^{CH_4 \rightarrow CH_4^+} \cdot n_{CH_4}^{ionizer}} \quad (4.16)$$

With A = detector signal, β = extraction efficiency of the ion from the ionizer, t = species mass-to-charge ratio dependent energy filter transmission efficiency, Θ = species mass-to-charge ratio dependent detector sensitivity, l = length of the ionizer cage, I_e = emission current of the ionizer, λ = slope of the electron impact ionization cross section at the threshold and n = species number density in the ionizer.

As ionizer current I_e and length l are equal for both species and the mass-to-charge ratio dependent quantities (β , t and Θ) are nearly equal for CH_3^+ and CH_4^+ Eq. 4.16 simplifies to:

$$\begin{aligned} \frac{A^{CH_3\cdot \rightarrow CH_3^+}}{A^{CH_4 \rightarrow CH_4^+}} &= \frac{\lambda^{CH_3\cdot \rightarrow CH_3^+} \cdot n_{CH_3\cdot}^{ionizer}}{\lambda^{CH_4 \rightarrow CH_4^+} \cdot n_{CH_4}^{ionizer}} \\ \Rightarrow n_{CH_3\cdot}^{ionizer} &= \frac{A^{CH_3\cdot \rightarrow CH_3^+}}{A^{CH_4 \rightarrow CH_4^+}} \cdot \frac{\lambda^{CH_4 \rightarrow CH_4^+}}{\lambda^{CH_3\cdot \rightarrow CH_3^+}} \cdot n_{CH_4}^{ionizer} \end{aligned} \quad (4.17)$$

If mass separation effects are neglected, which is a good approximation according to the findings in Section 4.1.2, than the number density of species x in the ionizer is proportional to the number density of species x in the reactor tube which in turn

calculates from the molar flow rate of x (\dot{F}_x), the total molar flow rate of all species \dot{F}_{total} and the total particle density n_{total} in the reactor

$$n_x^{ionizer} \propto n_x^{reactor} = \frac{\dot{F}_x}{\dot{F}_{total}} \cdot n_{total} \quad (4.18)$$

If Eq. 4.18 is inserted in Eq.4.17, \dot{F}_{total} and n_{total} cancel on each side and the molar flow rate of $CH_3\cdot$ radicals can be related to the molar flow rate of CH_4 molecules in the reactor:

$$\dot{F}_{CH_3\cdot,reactor} = \frac{A^{CH_3\cdot \rightarrow CH_3^+} \cdot \lambda^{CH_4 \rightarrow CH_4^+}}{A^{CH_4 \rightarrow CH_4^+} \cdot \lambda^{CH_3\cdot \rightarrow CH_3^+}} \cdot \dot{F}_{CH_4^{reactor}} \quad (4.19)$$

Finally, if molar flow rate of CH_4 can be calculated from the molar flow rate of the internal standard Ar \dot{F}_{Ar}^{in} using the response factor $R_{CH_4/Ar}^{cal}$ and the signal intensities for methane and argon ($S_{CH_4}^{25eV}$, S_{Ar}^{25eV}) at an ionization energy far above the ionization threshold.

$$\dot{F}_{CH_3\cdot} = \frac{A^{CH_3\cdot \rightarrow CH_3^+} \cdot \lambda^{CH_4 \rightarrow CH_4^+}}{A^{CH_4 \rightarrow CH_4^+} \cdot \lambda^{CH_3\cdot \rightarrow CH_3^+}} \cdot \dot{F}_{Ar}^{in} \cdot \frac{S_{CH_4}^{25eV}}{S_{Ar}^{25eV} \cdot R_{CH_4/Ar}^{cal}} \quad (4.20)$$

Eq. 4.20 allows to calculate the flow rate of methyl radicals $\dot{F}_{CH_3\cdot}$ at the sampling position from values which can be determined experimentally or taken from the literature. To minimize mass discrimination effects the calibration of CH_4 in Ar to determine $R_{CH_4/Ar}^{cal}$ has been performed at around 1000 °C. Instead of using just one point, the slopes of the ionization efficiency curves were determined from a linear fit of 20 – 40 data points above the threshold.

4.1.5 Detection Limits by using Threshold Ionization

A radical can be selectively detected by threshold ionization in a matrix of interfering molecules, if the energy of the ionizing electrons can be chosen to be higher than the ionization potential of the radical but lower than the appearance potential of any interfering molecular ion. In the system $CH_3\cdot / CH_4$ this is possible over an energy range of about 4.17 eV above the threshold as:

$$IP(CH_3^+ / CH_3\cdot) = 9.84 \text{ eV} \quad [106]$$

$$AP(CH_3^+ / CH_4) = 14.01 \text{ eV} \quad [107]$$

Unfortunately, the detection limit for radicals by threshold ionization can not be determined directly, as calibration samples containing highly reactive radicals can

not be prepared. To arrive at an estimate of the detection limit of radicals by threshold ionization, calibration mixtures of stable species have been measured. In a first experiment, a ‘worst case’ scenario was simulated by quantitative determination of CO in N_2 . Both ions CO^+ and N_2^+ are detectable on the same nominal mass ($m/z = 28 \text{ amu}$) but their ionization potential difference of 1.5 eV is only slightly larger than the electron energy spread of the ionizing electrons ($\pm 0.6 \text{ eV}$). Fig. 4.7 presents the energetic situation.

$$IP(CO) = 14.07 \text{ eV} \quad [108]$$

$$IP(N_2) = 15.58 \text{ eV} \quad [109]$$

In a second experiment, an ‘ideal’ scenario was simulated by detecting CH_4 in N_2 .

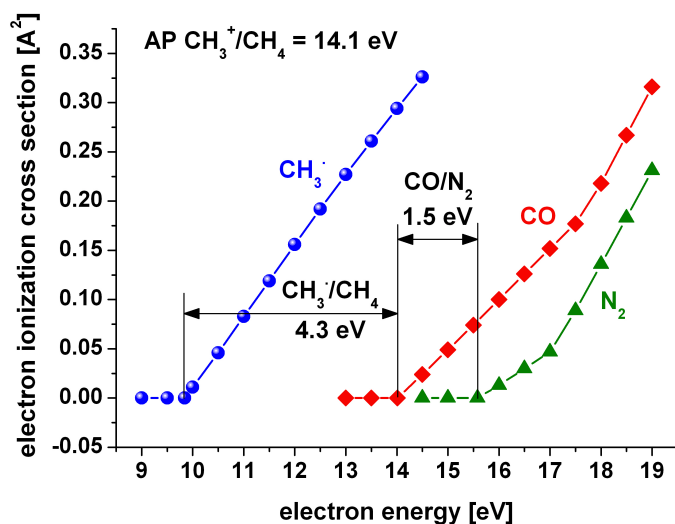


Figure 4.7: Electron ionization cross sections of CO [110] in N_2 [110] and CH_3 [111] in CH_4 [112]; CH_4 was omitted, as it overlaps with CO . The ionization potential difference in CO/N_2 is much smaller than in CH_3/CH_4 .

Here, CH_4^+ is detected at 16 amu and N_2^+ at 28 amu meaning that no spectral interferences occur at all and the full threshold region of methane ionization can be used.

‘Worst Case’ Scenario: CO/N_2

Facing an energy offset and energy spread of 1.1 eV and 0.6 eV respectively (cf. Section 4.1.3), a first threshold ionization measurement was performed with N_2 in Ar to identify an ionization energy, where the background from N_2 ionization is low and does not influence the CO signal. It was found that at an ionization energy

of 15.1 eV the N_2 signal was close to zero. This energy corresponds - background corrected - to the ionization potential of CO . The CO signal itself is then produced only from electrons from the higher energy tail of the Gaussian energy distribution, resulting in small but nearly undisturbed CO signals. CO/N_2 mixtures were prepared with nominal CO concentrations from 0.2 Vol% = 2000 ppm to 2 Vol% = 20000 ppm. The total gas flow was adjusted to $1000 \text{ ml} \cdot \text{min}^{-1}$. The actual concentration values were determined with an infrared analyzer and are listed in Table 4.2. The measured concentration values and the corresponding peak areas are listed in Tab. 4.3. The data were analyzed with the software *DINTEST* 2003 for evaluation of the detection limit and the results are shown in Fig. 4.8.

The calibration is strictly linear and the confidence interval is so narrow that it is hardly visible in Fig. 4.8. The detection limit was estimated to about 140 ppm, and if the outlier at 10640 ppm is removed, even to 80 ppm. The limit of quantification is 510 ppm with the value at 10640 ppm included and about 290 ppm if this value is removed. The linear regression intercept does not include zero as there is still some background from N_2 ionization. This experiment, simulating a ‘worst case’ scenario in terms of radical detection, shows, that radical concentrations of 80 ppm or higher can be detected with 95 % statistical certainty. Nevertheless, as the energy difference in case of $CH_3 \cdot / CH_4$ is much larger than in the system CO/N_2 (4 eV vs. 1.5 eV respectively), a larger excess energy can be used in methyl radical detection and the detection limit should be lower than 80 ppm. To arrive at an estimate of the detection limit in this more favorable case, CH_4 has been determined in N_2 as a second model system.

‘Ideal’ Scenario: CH_4/N_2

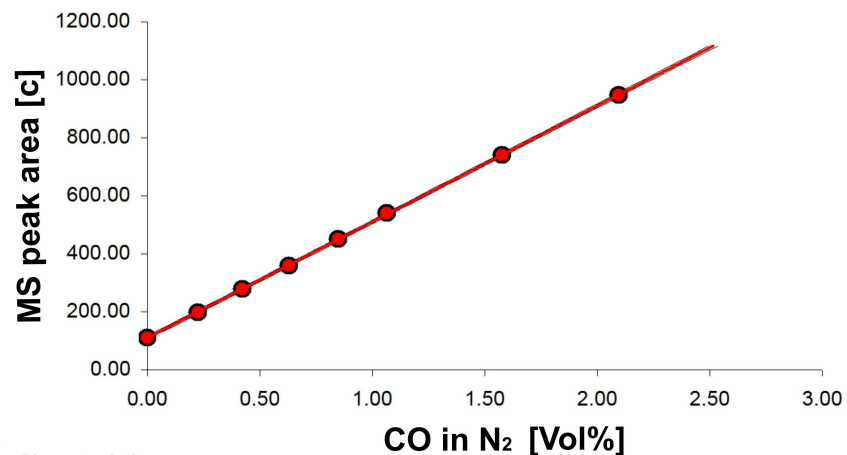
The theory of the quantification of threshold ionization data was explained in Section 4.1.4. As example, the threshold ionization data from 50 ppm CH_4 in Ar are presented in Fig. 4.9 I. For the quantification only the linear region of the ionization efficiency curve (3 eV above the energy corrected threshold) is used, symbolized by the blue line. The slope of this line corresponds to the A in Eq. 4.16-4.20. Fig. 4.9 II shows a dataset of concentrations from 10 – 75 ppm. The concentration values were determined by GC. With known methane concentrations the slopes can be plotted

Table 4.2: Parameters for the determination of the detection limit of CO in N_2

| $c(CO)$ set [ppm] | $\dot{V}(CO)$ [$ml \cdot min^{-1}$] | $\dot{V}(N_2)$ [$ml \cdot min^{-1}$] | $c(CO)$ measured [ppm] |
|-------------------|---------------------------------------|--|------------------------|
| 0 | 0 | 1000 | 0 |
| 2000 | 2 | 998 | 2260 |
| 4000 | 4 | 996 | 4240 |
| 6000 | 6 | 994 | 6290 |
| 8000 | 8 | 992 | 8480 |
| 10000 | 10 | 990 | 10640 |
| 15000 | 15 | 985 | 15760 |
| 20000 | 20 | 980 | 20960 |

Table 4.3: Results for the analysis of CO in N_2

| c [ppm] | 0 | 2260 | 4240 | 6290 | 8480 | 10640 | 15760 | 20960 |
|------------------|-------|-------|-------|-------|-------|-------|-------|-------|
| MS peak area [c] | 110.1 | 198.8 | 278.9 | 359.6 | 450.6 | 540.8 | 740.7 | 947.4 |

**Characteristics**

| | | | |
|------------------------------|---------|-----------------------------------|-------|
| Slope a | 400.497 | Number of measurements n | 1 |
| Intercept b | 109.786 | Standard error of estimate S_y | 2.447 |
| Correlation coefficient r | 1.0000 | Standard error of procedure S_x | 0.006 |
| Result uncertainty | 33.33 % | Sum of squared deviations | 3.467 |
| Probability of error (alpha) | 5.00 % | Quantile (one-sided) | 1.943 |
| | | Quantile (two-sided) | 2.447 |

Analytical limits according to DIN 32645

| | | |
|-----------------------|------------|-----------------|
| Limit of detection | 0.014 Vol% | |
| Limit of quantitation | 0.051 Vol% | (approximation) |
| | 0.051 Vol% | (exact) |

Figure 4.8: Linear regression of the MS peak area over concentration data with confidence band and statistical analysis CO in N_2 .

over concentrations, resulting in the calibration plot shown in Figure 4.9 **IV**.

As first it is obvious, that the usage of the signals of the first 3 eV behind the threshold gives much more intense signals compared to the detection of CO in N₂ in Section 4.1.5. The lowest used methane concentration of 10 ppm is still well quantifiable. The blue circles in this plot represent measurements performed in a second experimental series, showing only slight deviations and demonstrate the stability of the method.

For the quantification of radicals, where no stable source is available and the sampling orifice discharge is a function of composition and temperature, an internal standard (e.g. Ar) is necessary. Additionally, electron ionization cross sections at the threshold region are necessary (λ 's in Eq. 4.16-4.20). The cross sections for the methyl radical, methane and acetylene are shown in Figure 4.9 **III** and were taken from the literature (Ref. [111], [112] and [113] respectively). The ionization cross sections are handled in the same way as the threshold ionization MS signals, meaning that the slope of the linear region (e.g. 3 eV above the threshold) is used instead of just a single value at a fixed ionization energy. After each threshold ionization energy scan, a full mass spectrum was measured at 25 eV to obtain the values of $S_{CH_4}^{25eV}$ and S_{Ar}^{25eV} . Finally a CH₄ in Ar calibration at a reactor temperature of about 1000 °C and an ionization energy of 25 eV was measured to determine the response factor $R_{CH_4/Ar}^{cal}$ which is also required in Eq. 4.20:

$$R_{CH_4/Ar}^{cal} = \frac{S_{CH_4}}{S_{Ar}} \cdot \frac{\dot{F}_{Ar}}{\dot{F}_{CH_4}} = 0.9 \quad \text{for Ar as internal standard} \quad (4.21)$$

With the availability of energy dependent cross section data the quantification of nearly every gas compound is possible. The only constraints are the existence of a stable species producing a molecular ion with nearly the same mass as the analyte (CH₄ for CH₃·) in a direct ionization process and the absence of spectral interferences at the threshold. The latter prevents the detection of OH· radicals in the catalytic partial oxidation of methane, as the ionization threshold of the radical detected at 17 amu overlaps with the ionization threshold of CH₄ whose isotope ¹³C¹H₄ has also the mass 17 amu. ($IP(OH) = 13.2$ eV [114] and $IP(CH_4) = 12.6$ eV [115]).

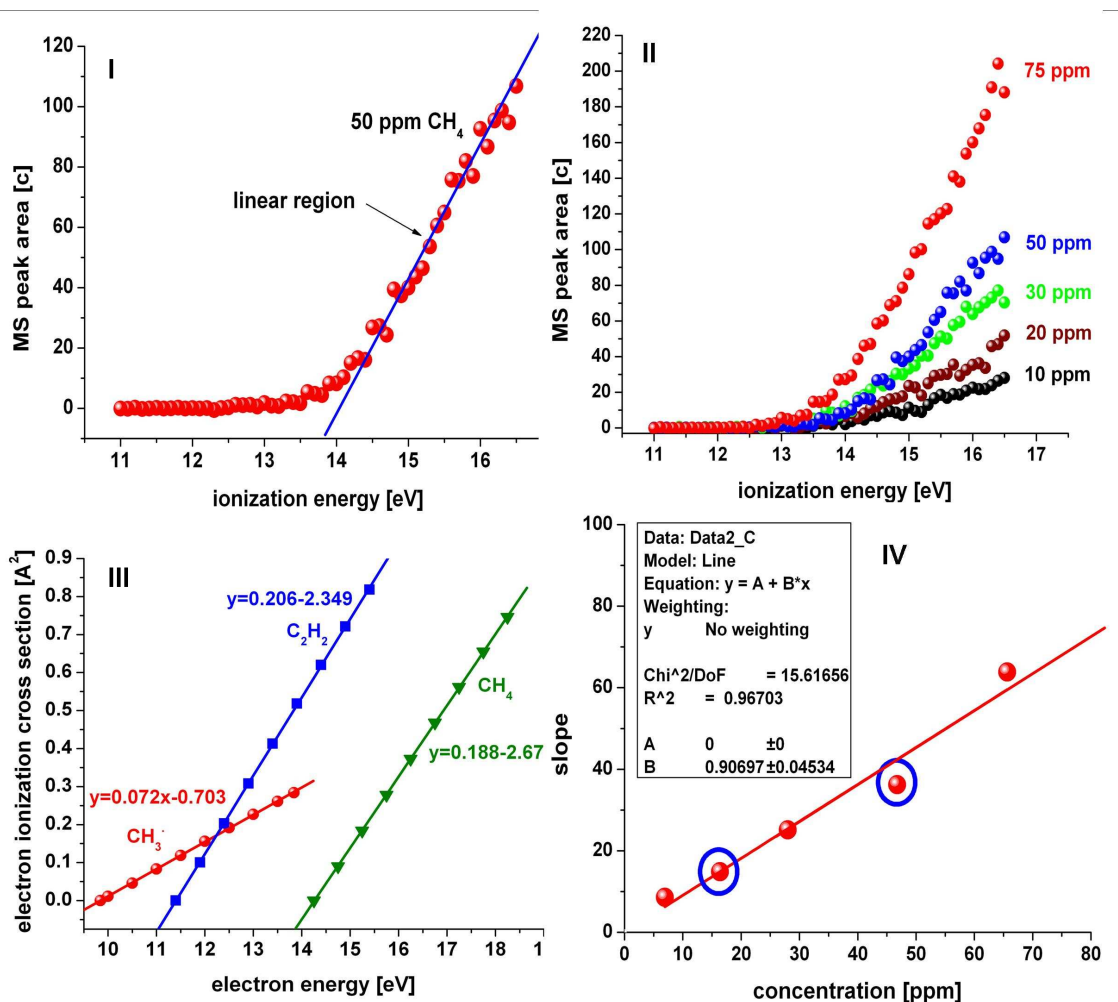


Figure 4.9: **I:** demonstration of the linear fit of threshold ionization MS data about 3 eV behind the threshold with 50 ppm CH_4 in Ar; **II:** threshold ionization MS data of five different, low CH_4 concentrations; **III:** linear fit of the electron ionization cross section data behind the threshold from $CH_3\cdot$ [111], CH_4 [112] and C_2H_2 [113]; **IV:** calibration of 10 ppm to 75 ppm CH_4 in Ar to demonstrate the stability of the method (the data with and without the blue circles represent two series of measurements) and the very low detection limit (< 10 ppm).

4.1.6 GC Calibration

The composition of the gases leaving the reactor was determined by GC. For the calibrations different concentrations of every compound were prepared by dilution in nitrogen or helium. The true concentrations were determined by measurement of the individual gas flows by a film-flow-meter (HORIBA Semiconductor). The calibration data were fitted by a straight line with the intercept set to zero:

- O_2 in He from 10 Vol% to 60 Vol%
- CH_4 in He from 10 Vol% to 60 Vol%
- H_2 in He from 4.4 Vol% to 50 Vol%
- N_2 in He from 25 Vol% to 75 Vol%
- CO from 3.44 Vol% to 7.02 Vol% → Lambda Mix
- CO_2 from 14.1 Vol% to 14.9 Vol% → Lambda Mix
- C1 to C6 alkanes from 0.01 Vol% to 0.1 Vol% → N17 and N18 Mix
- C2 to C4 alkenes from 0.01 Vol% to 0.1 Vol% → N19 and N20 Mix

The dynamic range of a Flame-Ionization-Detector (FID) covers typically seven orders of magnitude [116]. During the calibration process with methane it could be shown, that for the instrument used in this work, the linear range was at least four orders of magnitude. Measurements spanning a range from 0.01 Vol% to 50 Vol% deviated only by about 0.1 %. Table 4.4 summarizes the calibration results with y denoting the detector signal in mV and x the concentration in Vol%.

Some hydrocarbons produced during the experiments could not be quantified by the above described calibration procedure, as no reference substances were available (e.g. highly unsaturated C3 and C4 compounds). However, as the signal of the FID depends in a first approximation only on the number of carbon atoms in an organic compound [117], a calibration per C-atom is possible. The maximum difference for the three regularly calibrated C2 hydrocarbons (acetylene, ethylene and ethane) was about 13 %, for the five C4 compounds about 6 %. As the concentration accuracy of the calibration mixtures was about ± 10 % this difference is within the error bars. Therefore the approximation is valid as long as the molecule contains only C and H atoms. The data for calibration per carbon atom are shown in Table 4.5.

Table 4.4: GC calibrations of available compounds

| TCD - calibration | FID - calibration alkanes | FID - calibration alkenes |
|----------------------|------------------------------|-----------------------------------|
| $CO : y = 38.82x$ | $CH_4 y = 6120.8x$ | $C_2H_2 : y = 11482x$ |
| $CO_2 : y = 101.34x$ | $C_2H_6 : y = 11232x$ | $C_2H_4 : y = 12871x$ |
| $H_2 : y = 1.38x$ | $C_3H_8 : y = 25383x$ | $C_3H_6 : y = 25029x$ |
| $O_2 : y = 67.2x$ | $i - C_4H_{10} : y = 37839x$ | $1 - C_4H_8 : y = 39960x$ |
| $N_2 : y = 87.91x$ | $n - C_4H_{10} : y = 38230x$ | $cis - 2 - C_4H_8 : y = 39838x$ |
| $CH_4 : y = 43.55x$ | $n - C_5H_{12} : y = 50499x$ | $trans - 2 - C_4H_8 : y = 37922x$ |
| | $n - C_6H_{14} : y = 59361x$ | |

Table 4.5: GC calibrations per C-atom

| C3 | C4 | C5 | C6 |
|--------------|--------------|--------------|--------------|
| $y = 25200x$ | $y = 38750x$ | $y = 50500x$ | $y = 60000x$ |

4.1.7 Identification of Unknown Components by GC-MS

Whenever the methane oxidation was conducted at very high temperatures (up to 1300 °C) unknown peaks occurred in the gas chromatogram. As the production of oxygenates from methane is very unlikely, they were expected to be higher hydrocarbons. To quantify these unknown constituents using the above discussed calibration methods, at least the number of carbon atoms had to be determined. Based on the retention time of the peak in the chromatogram the number of carbon atoms could be roughly estimated. However, further analysis was necessary to clarify the molecular origin of the unknown peaks. For this purpose a very small fraction of the GC column effluent was sampled into a second mass spectrometer (Pfeiffer QMS 200) connected directly to the GC line upstream of the TCD and FID detectors (Fig. 4.10). A part of the separated gas stream entered the mass spectrometer only a few ms before being detected in the FID. Therefore a direct correlation of the GC peak and the fragmentation pattern was possible.

Important for a correct identification of the unknown molecules by means of their fragmentation pattern was the MS scan time. The FWHM (Full Width at Half Maximum) of the GC peaks was between 7 s and 12 s. The scan time of the MS had to be much smaller than this time, as otherwise some fragments would have been collected

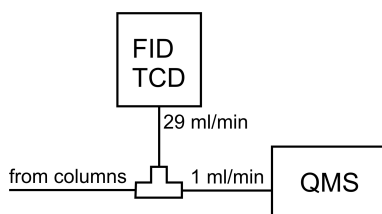


Figure 4.10: Sketch of the GC / MS combination for the identification of unknown GC peaks.

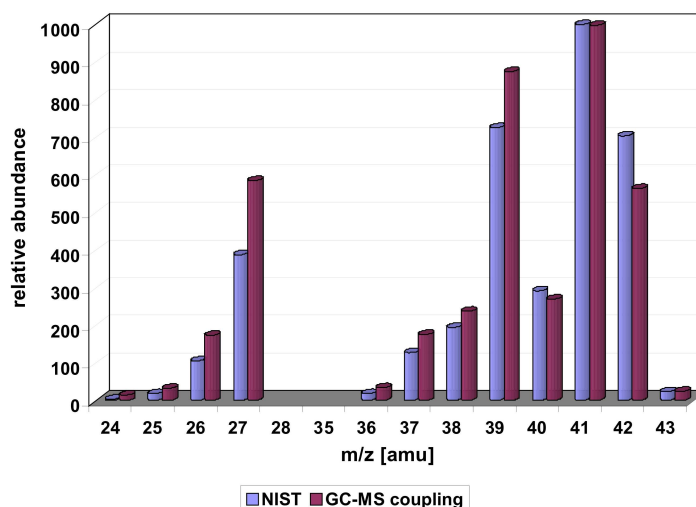


Figure 4.11: Comparison between reference (taken from NIST [118]) and measured propene fragmentation pattern.

at the front of the GC peak and others at the top leading to a wrong fragment intensity ratio and to false identification. With an optimized program a complete scan from 1 *amu* to 80 *amu* could be achieved in less than 4 *s*. This ensured, that groups of MS peaks (neighboring masses) were not affected by peak profile concentration changes and differences between multiple groups were small. To verify the applicability of the method, a sample mixture with known constituents (various alkenes with about 1000 *ppm*) was measured. Fig. 4.11 shows exemplarily the observed fragmentation pattern of propene peak and a comparison to a fragmentation pattern from the literature (NIST database [118]) which agree well enough to allow an identification. For very similar molecules (e.g. different C_4H_8 isomers) the identification by the MS fragmentation pattern was supplemented by sample chromatograms from the individual columns and injections of pure substances. Identified products and results will be shown in Section 4.4.3.

4.1.8 Standardless GC Quantification

Analysis of the reactor exhaust gases by gas chromatography was done after water removal from the effluent stream using the calibration data reported in Section 4.1.6. The water amount in the gas stream was reaction dependent and unknown, so that

the total gas volume change by water removal was different from experiment to experiment. Using an internal standard was not possible, as Ar was overlapping with O_2 in the Molsieve column and He was the carrier gas. N_2 could not be used as internal standard as it would have interfered with the CO detection in the MS.

This problem was solved by using the molecular carbon flow rate as internal standard. During the methane CPO no oxygenates and only *ppm* concentrations of larger molecules (benzene and higher ring systems) were formed. Carbon deposition in the tube was negligible. All carbon containing products were gaseous and could be quantified by GC after water removal. From these concentration values and the known inlet flow rates of methane and oxygen ($\dot{F}_{CH_4}^{in}$ and $\dot{F}_{O_2}^{in}$ respectively) the flow rates of all other species could be calculated as will be shown in the following:

For the carbon containing species an atom balance gives:

$$\dot{F}_C^{in} = \dot{F}_C^{out} = \dot{F}_{CH_4}^{in} \quad (4.22)$$

As every carbon containing species x can be detected by gas chromatography the carbon atom concentration in the effluent gas after water removal amounts to:

$$c_C^{total} = \sum \nu_x \cdot c_x \quad (4.23)$$

In 4.23, c_x denotes the concentration of the species x in *Vol%* and ν_x the number of C atoms in x . Individual flow rates for every carbon containing species can be calculated using:

$$\dot{F}_x = \frac{\dot{F}_C^{in}}{c_C^{total}} \cdot c_x \quad (4.24)$$

Assuming ideal gas behavior, the flow rates of non C containing molecules (O_2 , H_2 ...) can be calculated analogously, e.g.:

$$\dot{F}_{O_2} = \frac{\dot{F}_C^{in}}{c_C^{total}} \cdot c_{O_2} \quad (4.25)$$

Finally, the molar flow rate of water can be calculated from an oxygen atom balance:

$$\dot{F}_{H_2O}^{out} = 2 \cdot \dot{F}_{O_2}^{in} - \dot{F}_{CO}^{out} - 2 \cdot \dot{F}_{CO_2}^{out} - 2 \cdot \dot{F}_{O_2}^{out} \quad (4.26)$$

With all flow rates known the selectivities (S) and conversions (X) can be determined:

$$S_x = \frac{\dot{F}_x \cdot \nu_x}{(\dot{F}_{CH_4}^{in} - \dot{F}_{CH_4}^{out})} \quad (4.27)$$

$$X_{CH_4} = \frac{(\dot{F}_{CH_4}^{in} - \dot{F}_{CH_4}^{out})}{\dot{F}_{CH_4}^{in}} \quad (4.28)$$

The accuracy of the method has been determined in two ways. Firstly the hydrogen atom balance, i.e. the difference between the molar flow of H atoms in the reactor ($4 \cdot \dot{F}_{CH_4}^{in}$) and the molar flow of hydrogen atoms out of the reactor has been calculated to be below 10 %. Secondly, the calculated amount of water leaving the reactor (Eq. 4.26) was compared to the experimentally determined amount collected during a period of 2 h in the condenser. This difference was only 5 % (calculated $0.4 \text{ ml} \cdot \text{min}^{-1}$, measured $0.38 \text{ ml} \cdot \text{min}^{-1}$). In summary, the standardless GC quantification method proved to be applicable for this work, even though the error was slightly higher than by working with an internal standard (errors below 1 % possible).

4.1.9 Pyrometer Stability

The principles of optical pyrometry and the need for the application of ratio pyrometry in this work were explained in Section 3.1.4. The temperature of interest for the methane oxidation was of course that of the inner surface of the Pt tube. To determine the k -value so that the measurement of the pyrometer at the outer surface of the tube corresponds to the temperature of the inner surface of the tube, a thermocouple inside the reactor tube was used as reference. The thermocouple was positioned at the hottest point inside the tube and pressed against the tube wall to ensure good thermal contact. To avoid convective heat losses no gas flow was used inside the tube and the reactor chamber was evacuated. Furthermore the same optical pathway was used for the pyrometer calibration as in a real measurements (windows, mirrors, etc.). Figure 4.12 shows how closely the thermocouple and pyrometer readings match after adjusting the k -value. The deviation below $350 \text{ }^\circ\text{C}$ are due to the fact that this is the lowest temperature the pyrometer can measure. At higher temperatures the agreement is very good. Fig. 4.13 shows ten replications of full temperature profile scans along the tube to illustrate the reproducibility of the measurement. The temperature spikes $< 20 \text{ mm}$ and $> 85 \text{ mm}$ are caused by reflections from the copper clamps and are not real. The points in between reflect the real temperature profile of the tube. The reproducibility of the measurements is excellent, even at high scan rates (7 s/profile).

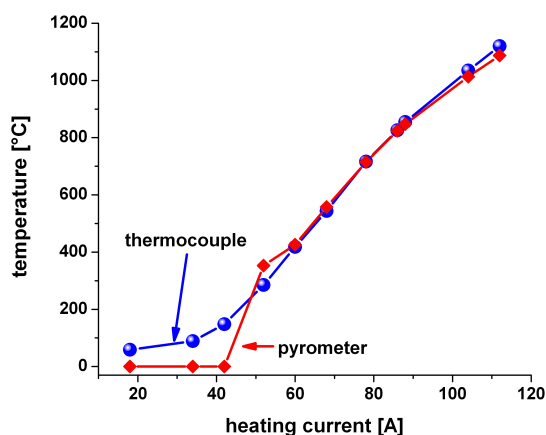


Figure 4.12: Comparison of thermocouple and pyrometer readings at the same position during heating of a platinum tube in vacuum.

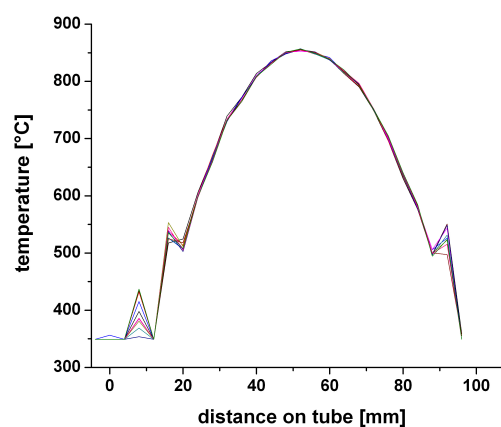


Figure 4.13: Overlay of 10 pyrometer spectra to demonstrate the stability and reproducibility of the measurement.

4.2 Description of Flow Parameters

4.2.1 Convective Mass Transport through the Reactor

Using a catalytic wall reactor (tube) with an inner diameter of 4.4 mm requires analyzing the influence of the mode of mass transport. A turbulent gas flow would provide good radial mixing of reactants and products along the reactor minimizing mass transport limitations. In laminar flow, a parabolic radial velocity profile develops in the tube and the rate of mass transport is only determined by diffusion from the bulk gas stream to the catalytically active tube wall. If diffusion processes are slower than the reaction rates at the surface, mass transport limitations arise. To estimate whether turbulent or laminar flow prevails in the reactor tube the Reynolds number was calculated for typical flow conditions using Eq. 4.29:

$$Re = \frac{\rho \cdot v \cdot D}{\eta} \quad (4.29)$$

In Eq. 4.29, ρ [$kg \cdot m^{-3}$] is the density, v [$m \cdot s^{-1}$] the velocity, D [m] the tube diameter and η [$Pa \cdot s$] the dynamic viscosity of the fluid medium. The dimensionless Reynolds number gives an indication of the relative importance of inertial and viscous forces in the fluid system. For Reynolds numbers below 2100 the flow in the tube can be

considered laminar whereas at higher values any appreciable disturbance (e.g. wall roughness) leads to turbulent flow.

During the reaction, gas composition and temperature change along the tube axis. Because of this, the Reynolds numbers were calculated for three different sets of gas temperature, composition and velocity.

- set A: reactor inlet conditions (298 K , reactant mixture)
- set B: conditions at reactor temperature maximum (1573 K , product mixture)
- set C: reactor outlet conditions (673 K , product mixture)

The temperature dependent dynamic viscosities were taken from the literature [119] and are listed in Table 4.6.

Table 4.6: Dynamic viscosities of reactants and products

| — | viscosity [$Pa \cdot s$] | viscosity [$Pa \cdot s$] | viscosity [$Pa \cdot s$] |
|-------------|----------------------------|----------------------------|----------------------------|
| T [K] | 298 | 673 | 1573 |
| CO | — | 0.000034 | 0.00007 |
| CO_2 | — | 0.00003 | 0.000051 |
| H_2 | — | 0.00001554 | 0.000026 |
| H_2O | — | 0.00002412 | 0.000058 |
| He | 0.00001941 | 0.00003436 | 0.000053 |
| CH_4 | 0.00001331 | 0.00002026 | 0.00003 |
| O_2 | 0.00002018 | — | — |

Reynolds Number at Reactor Inlet Conditions (298 K) - set A:

To calculate the Reynolds number for reactor inlet conditions a temperature of (298 K) was assumed. The gas density was calculated using Eq. 4.30 based on the composition listed in Table 4.7:

$$\rho = \frac{p \cdot \bar{M}}{R \cdot T} \quad (4.30)$$

Table 4.7: Reactor inlet gas composition

| species | flow [$ml \cdot min^{-1}$] | molecular mass [$kg \cdot mol^{-1}$] | mole fraction [X_i] |
|---------|------------------------------|--|-------------------------|
| total | 1022 | — | — |
| CH_4 | 500 | 0.016 | 0.489 |
| O_2 | 416 | 0.032 | 0.407 |
| He | 106 | 0.004 | 0.104 |

$$p = \text{pressure [Pa]} = 110000 \text{ Pa}$$

$$\bar{M} = \text{mean molecular mass [kg} \cdot \text{mol}^{-1}]$$

$$R = \text{universal gas constant [Pa} \cdot \text{m}^3 / (\text{mol} \cdot \text{K})] = 8.3145 \text{ [Pa} \cdot \text{m}^3 / (\text{mol} \cdot \text{K})]$$

$$T = \text{absolute temperature [K]} = 298 \text{ K}$$

The mean molar mass was calculated by Eq. 4.31 using the species mole fractions from Table 4.7. With the same mole fractions and the pure component viscosities from Table 4.6, the mixture viscosity was calculated by Eq. 4.32:

$$\bar{M} = \sum X_i \cdot M_i = 0.02126 \text{ [kg} \cdot \text{mol}^{-1}] \quad (4.31)$$

$$\eta = \sum X_i \cdot \eta_i = 1.674 \cdot 10^{-5} \text{ Pa} \cdot \text{s for } 298 \text{ K} \quad (4.32)$$

The density of the reactant gas mixture at 298 K is about

$$\rho_{298 \text{ K}} = 0.944 \text{ kg} \cdot \text{m}^{-3}$$

For the reactant stream the gas velocity v results direct from the tube dimensions and the flow, using:

$$L = \text{tube length} = 0.1 \text{ m}$$

$$D = \text{internal tube diameter} = 0.0044 \text{ m}$$

$$\dot{V} = \text{volume flow} = 1022 \text{ ml} \cdot \text{min}^{-1} = 1.70 \cdot 10^{-5} \text{ m}^3 \cdot \text{s}^{-1}$$

$$v = \frac{L}{t} \text{ with } t = \frac{V_{\text{tube}}}{\dot{V}} \rightarrow v_{298} = \frac{4 \cdot L \cdot \dot{V}}{\pi \cdot D^2 \cdot L} = 1.1 \text{ m} \cdot \text{s}^{-1} \quad (4.33)$$

With these values, the resulting Reynolds number for the inlet gas composition at 298 K calculates to:

$$Re_{298} = 270$$

Reynolds Number at Reactor Temperature Maximum (1573 K) - set B:

To calculate the Reynolds number at reactor temperature maximum, the gas composition shown in Table 4.8 was used which corresponds to the composition measured at 1573 K at the reactor outlet by GC.

Table 4.8: Molecular fractions of the constituents of the product gas streams

| species | molecular mass [$kg \cdot mol^{-1}$] | mole fraction [X_i] |
|----------|--|-------------------------|
| H_2O | 18 | 0.296 |
| CO | 28 | 0.208 |
| CH_4 | 16 | 0.037 |
| CO_2 | 44 | 0.047 |
| H_2 | 2 | 0.298 |
| C_2H_2 | 26 | 0.027 |
| He | 4 | 0.088 |

Using these mole fractions the mean molar mass and the mixture viscosity result to:

$$\begin{aligned}\bar{M}_{1573} &= 0.01863 \text{ g} \cdot \text{mol}^{-1} \\ \rho_{1573} &= 0.157 \text{ kg} \cdot \text{m}^{-3} \\ \eta_{1573} &= 4.77 \cdot 10^{-5} \text{ Pa} \cdot \text{s}\end{aligned}$$

The gas velocity is influenced by temperature and mole number changes and was calculated by Eq. 4.34 with the value at 298 K as reference.

$$v_{1573 \text{ K}} = v_{298 \text{ K}} \cdot \frac{1573 \text{ K}}{298 \text{ K}} \cdot \frac{X_{He,298 \text{ K}}}{X_{He,1573 \text{ K}}} = 6.9 \text{ m} \cdot \text{s}^{-1} \quad (4.34)$$

Inserting all these values in Eq. 4.29 results in a Reynolds number at reactor temperature maximum of

$$Re_{1573} = 100$$

Reynolds Number at Reactor Outlet Conditions (673 K) - set C:

To calculate the Reynolds number at reactor outlet conditions, the same composition as listed in Table 4.8 but a temperature of 673 K was used leading to the following values:

$$\begin{aligned}\bar{M}_{673} &= 0.01863 \text{ g} \cdot \text{mol}^{-1} \\ \rho_{673} &= 0.366 \text{ kg} \cdot \text{m}^{-3} \\ \eta_{673} &= 2.40 \cdot 10^{-5} \text{ Pa} \cdot \text{s} \\ v_{673 \text{ K}} &= 2.9 \text{ m} \cdot \text{s}^{-1} \\ \Rightarrow Re_{673} &= 195\end{aligned}$$

According to these Reynolds numbers varying between 100 and 270, the flow in the *Pt* tube is under all conditions well in the laminar flow region. Therefore, a concentration profile in radial direction might develop for fast reactions, as diffusion is the only transport mechanism from the centerline gas stream to the reacting walls. As will be presented in the following section, a comparison of characteristic diffusion times of reactants to the catalytic tube wall with characteristic times for convection and reaction will give insight into the problem of mass transport influence on the reaction.

4.2.2 Radial Mass Transport by Diffusion

To analyze whether oxygen breakthrough will occur in the *Pt*-tube because diffusive mass transport to the catalytic tube wall is slower than convective mass transport through the tube, one has to compare the characteristic time for the convective transport of the O_2 molecules $\tau_C[s]$ to the characteristic diffusion time of O_2 in radial direction $\tau_D[s]$ [120]. With $L = \text{tube length [cm]}$, $v = \text{gas velocity [cm} \cdot \text{s}^{-1}\text{]}$, $R_{\text{tube}} = \text{radius [cm]}$, $D = \text{diffusion coefficient [cm}^2 \cdot \text{s}^{-1}\text{]}$) these two characteristic times calculate to:

$$\tau_C = \frac{L_{\text{tube}}}{v} \quad (4.35)$$

$$\tau_D = \frac{R_{\text{tube}}^2}{D} \quad (4.36)$$

The convective transport times can be easily calculated using the three sample flows from Section 4.2.1 with linear velocities of $\approx 1.1 \text{ m}\cdot\text{s}^{-1}$, $\approx 3.2 \text{ m}\cdot\text{s}^{-1}$ and $\approx 6.9 \text{ m}\cdot\text{s}^{-1}$ corresponding to 298 K, 873 K and 1573 K conditions respectively. With a tube length of 10 cm this results in:

$$\tau_{C, 1.1 \text{ m}\cdot\text{s}^{-1}} = 91 \text{ ms}$$

$$\tau_{C, 3.2 \text{ m}\cdot\text{s}^{-1}} = 31 \text{ ms}$$

$$\tau_{C, 6.9 \text{ m}\cdot\text{s}^{-1}} = 14 \text{ ms}$$

The calculation of the characteristic diffusion time of O_2 is more complex, because first the diffusion coefficient must be known. Whereas the diffusion coefficient of a particular species can be easily calculated for binary mixtures, this is quite complicated for a multi component mixture. The procedure used in this work was adopted from Baerns et al. [121]. In a first step, all binary diffusion coefficients $D_{O_2,j}$ with j indicating all gas species but O_2 are calculated using Eq. 4.37

$$D_{O_2,j} = \frac{18.583 \cdot T^{3/2} \cdot [(M_{O_2} + M_j)/M_{O_2}M_j]^{0.5}}{p \cdot \sigma_{O_2,j}^2 \cdot \Omega} \quad \text{in } [cm^2 \cdot s^{-1}] \quad (4.37)$$

with:

$$T = \text{absolute temperature } [K]$$

$$M = \text{molecular mass } [kg \cdot kmol^{-1} = g \cdot mol^{-1}]$$

$$p = \text{total pressure } [10^5 \text{ Pa}]$$

$$\Omega = \text{collision integral}$$

$$\epsilon = \text{force constant } [J]$$

$$\sigma = \text{collision diameter for the Lennard – Jones – Potential } [pm]$$

The collision integral itself is a function of ϵ :

$$\Omega = f\left(\frac{kT}{\epsilon_{O_2,j}}\right) \quad (4.38)$$

with:

$$\epsilon_{O_2,j} = \sqrt{\epsilon_{O_2} \cdot \epsilon_j} \quad \text{and} \quad (4.39)$$

$$\sigma = 0.5(\sigma_{O_2} + \sigma_j) \quad (4.40)$$

Table 4.9 summarizes all data for the reactant and product species. To calculate

Table 4.9: Parameters to estimate the O_2 diffusion coefficient in the reaction mixture

| species | M [$g \cdot mol^{-1}$] | σ [pm] | ϵ [J] | $X_{reactant}$ | $X_{product}$ |
|----------|----------------------------|-------------------|-----------------------|----------------|---------------|
| CH_4 | 16 | 375.8 | $2.05 \cdot 10^{-21}$ | 0.489 | 0.037 |
| O_2 | 32 | 346.7 | $1.47 \cdot 10^{-21}$ | 0.407 | 0 |
| Ar | 40 | 354.2 | $1.30 \cdot 10^{-21}$ | 0.104 | 0.088 |
| CO | 28 | 369 | $1.27 \cdot 10^{-21}$ | 0 | 0.208 |
| CO_2 | 44 | 394.1 | $2.69 \cdot 10^{-21}$ | 0 | 0.047 |
| H_2O | 18 | 264.1 | $1.12 \cdot 10^{-20}$ | 0 | 0.296 |
| H_2 | 2 | 282.7 | $8.24 \cdot 10^{-22}$ | 0 | 0.298 |
| C_2H_2 | 26 | 403.3 | $7.73 \cdot 10^{-21}$ | 0 | 0.027 |

the multi component O_2 diffusion coefficient from the binary diffusion coefficients, the theory of Wilke [122] was used (Eqn. 4.41) with $D_{O_2,j}$ being the binary diffusion coefficient and X mole fractions.

$$D_{O_2} = \frac{1 - X_{O_2}}{\sum_{j=1, j \neq O_2}^{N-1} X_j / D_{O_2,j}} \quad (4.41)$$

In total four diffusion coefficients were calculated. Two for the reactant mixtures at 298 K and 873 K respectively, and two for the product compositions at 873 K and 1573 K:

$$\begin{aligned} D_{O_2}(298 \text{ K}, \text{ reactant mixture}) &= 0.21 \text{ cm}^2 \cdot \text{s}^{-1} \\ D_{O_2}(873 \text{ K}, \text{ reactant mixture}) &= 1.37 \text{ cm}^2 \cdot \text{s}^{-1} \\ D_{O_2}(873 \text{ K}, \text{ product mixture}) &= 1.69 \text{ cm}^2 \cdot \text{s}^{-1} \\ D_{O_2}(1573 \text{ K}, \text{ product mixture}) &= 4.54 \text{ cm}^2 \cdot \text{s}^{-1} \end{aligned}$$

The calculation of the characteristic diffusion times in radial direction and the comparison to the characteristic convection times at the corresponding temperatures are shown in Table 4.2.2. At 298 K and at 873 K, regardless whether a reactant or product mixture is assumed, the characteristic diffusion time of O_2 to the tube wall is always higher than the characteristic convection time through the tube. It can therefore be expected that O_2 conversion will be incomplete and that, provided fast O_2 consumption at the wall, pronounced radial gradients will develop. Only at very high temperatures (1573 K), O_2 diffusion is fast enough to compete with the axial convective transport and complete O_2 conversion can be expected.

Table 4.10: Comparison of characteristic times for axial convective and radial diffusive O_2 transport τ_C , τ_D respectively

| | v [$cm \cdot s^{-1}$] | τ_C [ms] | D_{O_2} [$cm^2 \cdot s^{-1}$] | τ_D [ms] | τ_C/τ_D |
|-------------------------|---------------------------|-------------------|-----------------------------------|-------------------|-----------------|
| 298 K, reactant mixture | 110 | 91 | 0.21 | 230 | 0.40 |
| 873 K, reactant mixture | 320 | 31 | 1.37 | 35 | 0.89 |
| 873 K, product mixture | 320 | 31 | 1.69 | 29 | 1.07 |
| 1573 K, product mixture | 690 | 14 | 4.54 | 11 | 1.27 |

4.3 Catalytic Partial Oxidation of Methane on *Pt*

4.3.1 Ignition Studies

In Section 4.3.1 the ignition of methane oxidation on *Pt* in the catalytic wall reactor is described. To follow product development during a temperature programmed reaction experiment it was necessary to limit heat generation by exothermic oxidation reactions. This was achieved by using a low flow rate of only $100 \text{ ml} \cdot \text{min}^{-1} CH_4$, $50 \text{ ml} \cdot \text{min}^{-1} O_2$ and $50 \text{ ml} \cdot \text{min}^{-1} He$ corresponding to synthesis gas stoichiometry ($C/O = 1.0$). Under these conditions, convective and radiative heat losses were higher than heat generation by exothermic reactions, allowing to perform a temperature programmed experiment. The temperature ramp was controlled by an EURO THERM controller (model: 3472) and the temperatures were measured directly under the skimmer. The product gas was analyzed by mass spectrometry in the tube center. Due to the very low flow rates the gas mixture has enough time to react before the orifice. Additionally a large fraction of the gas stream will escape through the orifice disturbing the laminar flow. This results in the observed total oxygen conversion. A set of MS signals corresponds to a product distribution at the related temperature.

A typical temperature profile is displayed in Fig. 4.14 and a photograph of the tube perimeter at the point of ignition is shown in Fig. 4.15. The corresponding *He* normalized mass spectrometer traces are displayed in Fig. 4.16 and Fig. 4.17.

Starting from $400 \text{ }^\circ C$ the temperature increases linearly. The onset of methane and oxygen conversion is observed at around $450 \text{ }^\circ C$ which agrees well with ignition temperatures reported by several authors for the same stoichiometry in the literature [123]. The actual reactor light off is delayed to about $580 \text{ }^\circ C$ as convective and

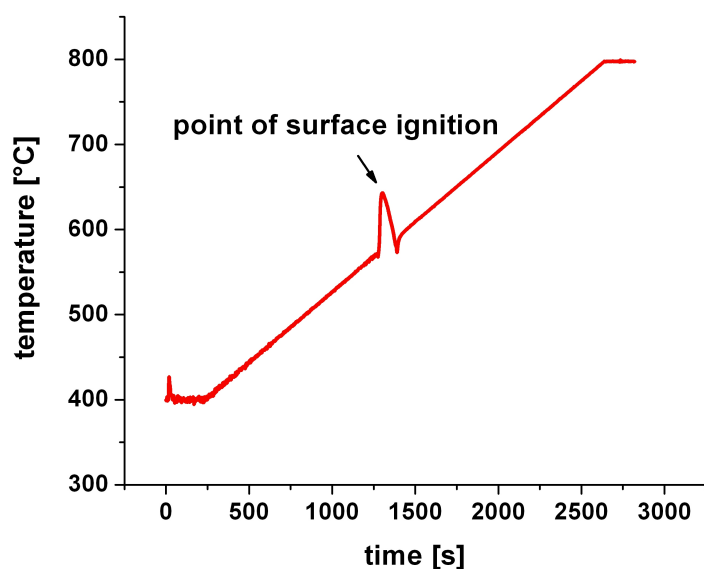


Figure 4.14: Temperature ramp of methane CPO ignition study - heating rate $10 \text{ K} \cdot \text{min}^{-1}$. Data were smoothed by a 20 point FFT filter.

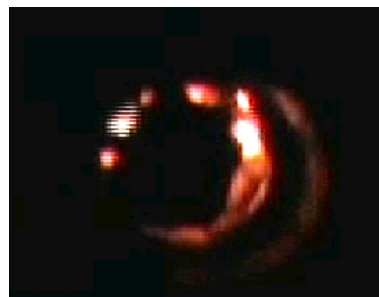


Figure 4.15: Snapshot of the surface ignition (view through the tube).

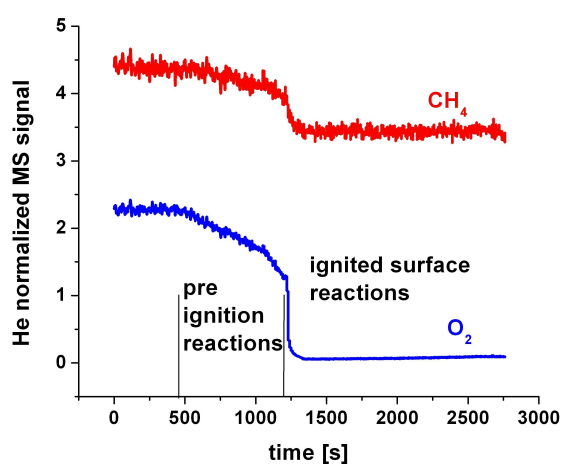


Figure 4.16: Reactant distribution during ignition. Moderate conversion before surface ignition visible. The ignition is represented by full oxygen conversion. Data were smoothed by a 5 point FFT filter.

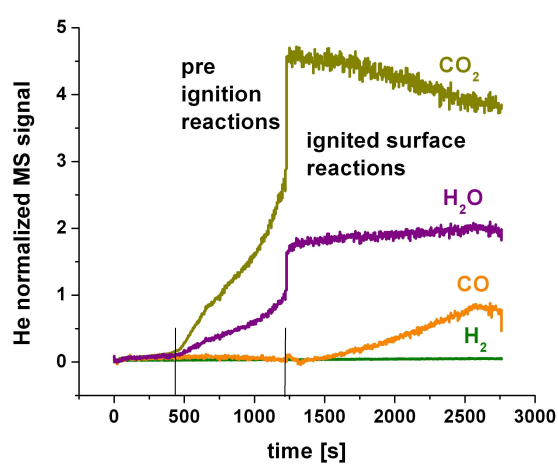
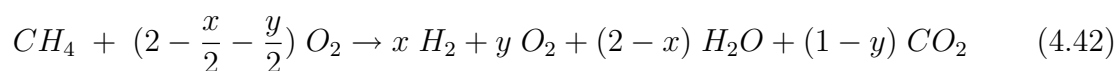


Figure 4.17: Background corrected product distribution during ignition. The CO signal was additionally reduced by the fragmentation of CO_2 on $m/z = 28$. Data were smoothed by a 5 point FFT filter.

radiative heat losses are high (cf. 2.1.2). The peak in the temperature ramp is due to the delayed response of the temperature controller to the sudden heat liberation at the ignition point.

With respect to product formation it can be seen from Fig. 4.17 that H_2O and CO_2 (total oxidation products) are formed during the ignition process. Before reactor light off, no partial oxidation products are formed. After light off, the CO trace starts to increase on the expense of the CO_2 signal. The shift from CO_2 to CO formation with increasing temperature reflects probably the thermodynamic shift from the highly exothermic total oxidation to the less exothermic partial oxidation. Hydrogen was only produced in minor amounts at temperatures up to 800 °C due to the very low activation energy for the surface OH formation of 11 $kJ \cdot mol^{-1}$ [10]. The overall reaction can be described with Eq. 4.42 [34]:



The values x and y depend strongly on the operation conditions, such as temperature.

Due to the low flow rates oxygen was always completely consumed after reactor light off. From Fig. 4.15 showing a snap shot view through the tube during ignition it can be seen that the ignition does not occur uniformly across the *Pt* surface rather than on a few distinct spots.

4.3.2 Reaction Zone Shifting

During ignition the reactor operates in transient mode and product formation can be followed as a function of temperature. In a second experiment, the reactor was operated stationary and product formation was studied by sampling the reaction zone at different points with respect to the fixed sampling orifice. Fig. 4.18 shows schematically the location of the sampling points on the temperature profiles and Figure 4.19 shows photographs (left panels) and mass spectra taken at the different points (right panels).

The mass spectrum at point **I** was measured right after ignition of a $C/O = 0.6$ reaction mixture containing 200 $ml \cdot min^{-1}$ CH_4 , 150 $ml \cdot min^{-1}$ O_2 and 2000 $ml \cdot min^{-1}$ He at a heating current of 112 A. The high He flow was necessary to shift the

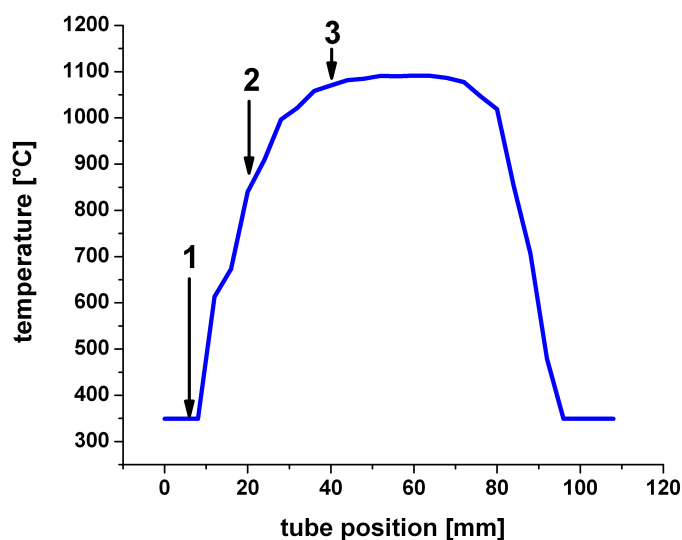


Figure 4.18: Qualitative tube temperature profile and sample points.

reaction zone downstream the skimmer. At point **I**, the reactant gases are not yet ignited below the orifice position but downstream and only reactants are visible in the mass spectrum.

The mass spectrum at point **II** was obtained after the reactor had reached steady state. To adjust sampling point **II** in the middle of the heating up zone, the heating current was slightly reduced to 101 *A*. This sampling point is located on a steep slope of temperature. Within some *mm* it increases by a few 100 *K*, resulting in a likewise change in the reactant and product distribution. At point **II** the reaction is ignited but a lot of O_2 is still left in the mixture. In agreement to the results of the ignition studies discussed in Section 4.3.1, H_2O , CO and CO_2 are the only products formed in presence of high concentrations of gas phase O_2 .

At point **III** which is close to the temperature maximum of the tube, a heating current of 130 *A* was used and the *He* flow was reduced to $1000 \text{ ml} \cdot \text{min}^{-1}$. The mass spectrum shows that the gas phase O_2 concentration has dropped to approximately half its value at point **II**. The CO/CO_2 peak ration has shifted from 1 at point **II** to nearly 3. There is still no H_2 formation at point **III**.

One drawback of this kind of experiments is the limited comparability between all three points. Although each point was measured under steady state conditions the transport and reaction rates are changed by varying flow rates, compositions and heating currents in these shift experiments. Therefore only a very qualitative picture

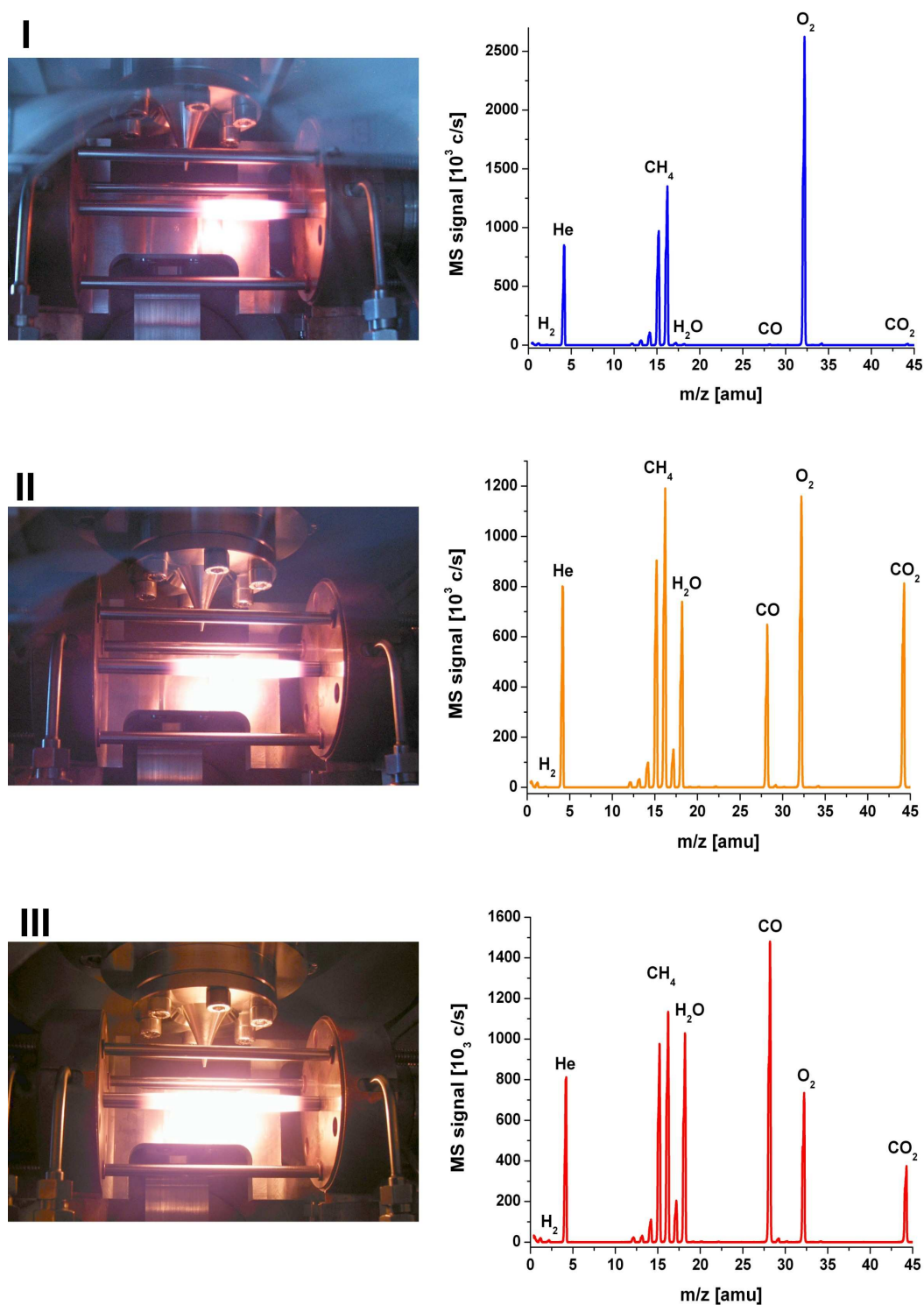


Figure 4.19: Photographs (left panels) and mass spectra (right panels) from reaction zone shifting experiments: I) Sampling at the reaction zone onset, II) Sampling between reaction zone onset and temperature maximum, III) Sampling at temperature maximum.

of the reaction sequence during the methane oxidation in the platinum tube can be derived:

First, the reactant gas stream enters the *Pt* tube at room temperature heats up. Between 450 °C and 500 °C surface oxidations start leading essentially to CO_2 and H_2O . After ignition at 580 °C CO is formed. With increasing temperature the CO/CO_2 ratio increases but H_2 is not observed as long as significant concentrations of gas phase O_2 are present.

4.3.3 Visual Examination of the Reaction Zones

A visual inspection of a catalyst tube after reaction revealed the presence of different regions, which correlated with the observed temperature and gas species distribution. In Fig. 4.20 a cut through a used *Pt/ 10% Rh* tube is shown. This metal mix was not used in the catalytic studies to minimize the catalyst complexity, but shows qualitatively equal behavior in the zoning - carbon coverage and surface reconstruction.

A more detailed study of the individual parts by SEM microscopy is given in Fig. 4.21. In Fig. 4.21 **I** the part of the reaction tube is shown, which is kept in the cooled copper clamps. No changes of the surface before and after the reaction were noticeable. Following the flow path the reactants were heated up and reactions become feasible. In 4.21 **II** a transition from an unchanged surface (upper part) over a region, where Rh_xO_y was detectable (bright stripe), to a carbon covered surface represents the ignition region of the surface reaction. Oxygen was present at least in the oxide containing area near the surface as the oxide otherwise became instable. As shown in 4.21 **III** the carbon layer was not dense. Pit formation, particle deposition and cracks in the surface indicate the beginning reconstruction of the surface. The

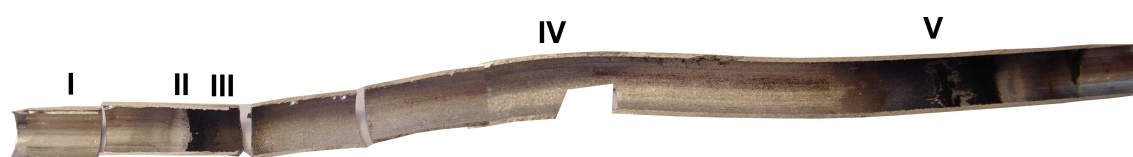


Figure 4.20: Cut through a *Pt/ 10% Rh* tube, used in the methane CPO reaction. Visible are several regions, part of them are visually covered with carbon. Gas flows from left to right.

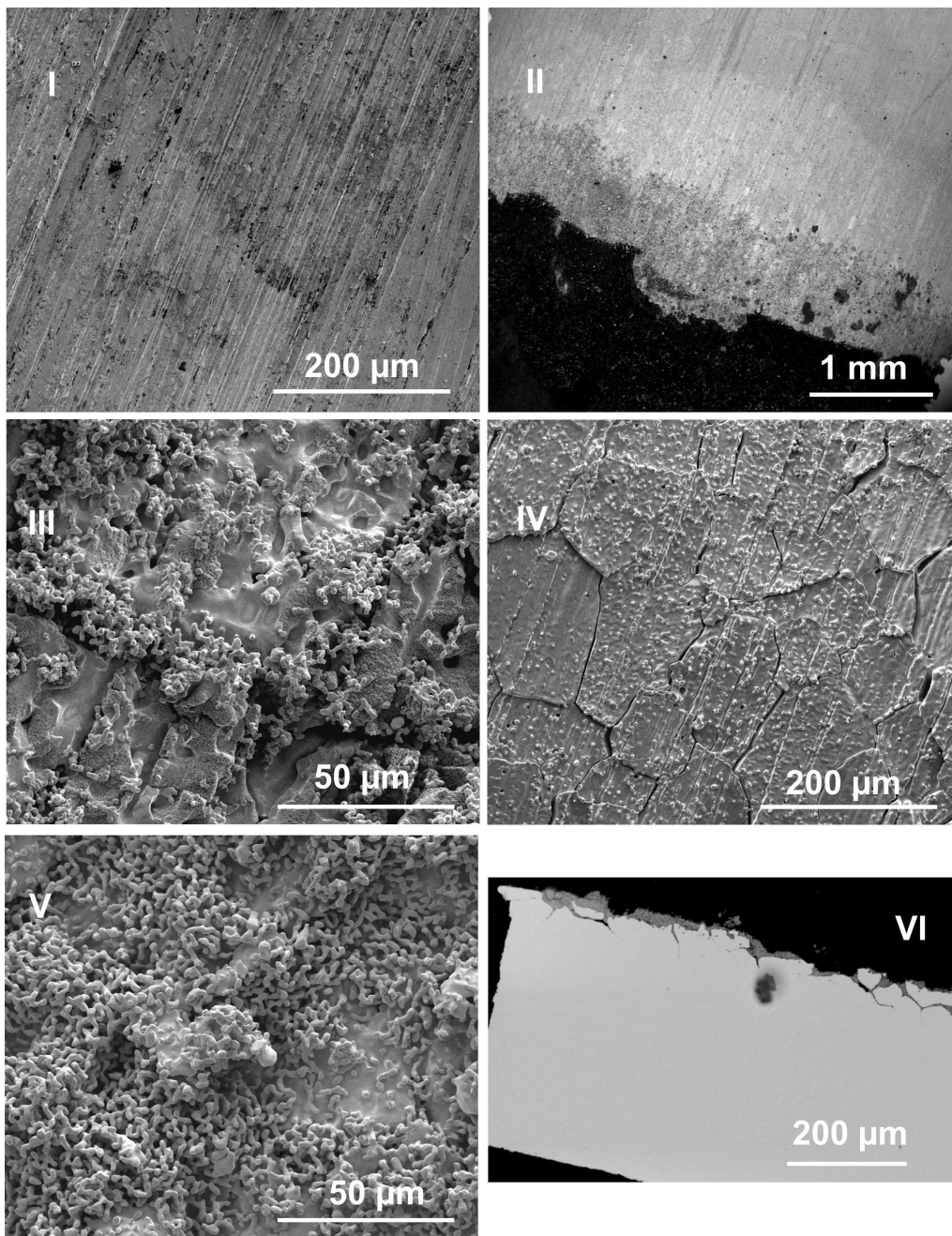
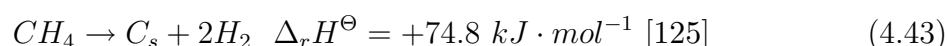


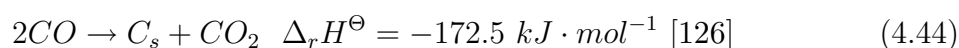
Figure 4.21: **I** shows the cold inlet region - only striations from the production process are visible. In region **II** the change into the reaction zone is displayed. The bright stripe contains Rh_xO_y , in flow direction carbon formation starts. The carbon film is not dense, but consists of partly carbon covered particles and small carbon deposits, shown in region **III**. At the hottest position the surface is massively destroyed, as shown in **IV** and in a cross section **VI**. The carbon deposits at the outlet, region **V**, are relatively equal to **III**.

rupture of the surface became most intense in 4.21 **IV** illustrating the hottest zone under reaction conditions. A noticeable material transport in outlet direction is shown by the elevated number of particles deposited in 4.21 **V**.

The occurrence of a solid carbon phase additionally to the gaseous products can be described by methane decomposition on the platinum surface Eq 4.43 [124]:



and by the Boudouard reaction, where also a connection between both carbon oxides is established Eq. 4.44 [124].



The formation of carbonaceous deposits is suppressed in region **IV** due to the very high temperatures where the Boudouard reaction is shifted towards *CO*. In the colder regions **III** and **V** its equilibrium moves towards *CO*₂ and *C*_s. Additionally this results in a less effective conversion of carbon produced by methane decomposition, elevating the influence of this reaction. On this account carbon is deposited in this regions.

The reconstructions of the metallic surface are manifold but are more influenced by the gas atmosphere than by the temperature. Fig. 4.22 shows the vacuum side of the tube in region **IV** - the hottest part. Clearly grain boundaries are visible, but the surface is intact. Only impurities (e.g. *Si*, *Ca* and *Mg*) segregate from the bulk to the surface, especially at the boundaries. The same region looks massively destructed at the catalytic active side (cf. Fig 4.21 **IV**). At the grain boundaries the surface is flake like cracked and at some positions these flakes are only loosely connected to the subjacent material.

The reconstruction of catalyst metal (*Pt* and *Rh*) surfaces has been extensively studied in ammonia oxidation [127, 128, 129]. In general the reconstruction of pure *Pt* catalysts was stronger than for mixtures with *Rh*. Beside the fact that surface reconstructions in hydrocarbon oxidation reactions are not that much studied, they are expected to occur on the pure platinum tube used in methane CPO during this study. The surface reconstruction and noticeable material transport become indeed even more important if less massive catalytic system, e.g. *Pt* gauzes or supported films and particles are studied over longer times.

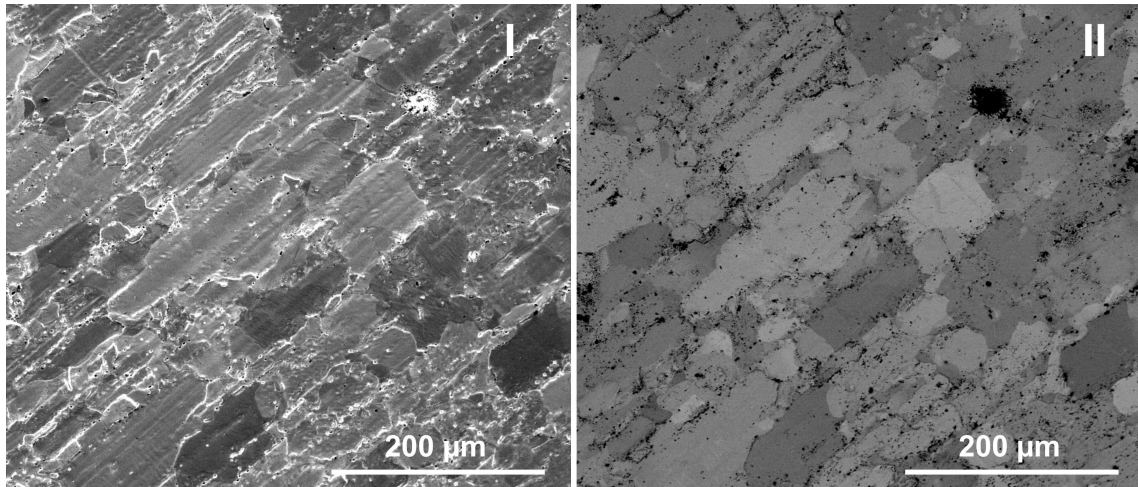


Figure 4.22: Region **IV** from the vacuum (outer) side. **I** shows the ETD detector picture, representing the topography, **II** the SSD detector, displaying more the elementary contrast.

The catalyst reconstruction under reaction conditions was not extensively studied during this work, but may be an interesting research objective during, e.g. the study of deactivation processes using supported platinum catalysts.

4.4 Catalytic Partial Oxidation of Methane - $C/O = 0.6$

To study the interaction of surface and gas phase reactions for the methane oxidation in the *Pt* catalytic wall reactor temperatures of up to 1300 °C had to be realized. As the electrical heating power was insufficient to reach this temperature, an oxygen rich gas mixture ($C/O = 0.6$) was used so that the liberated heat of reaction could be used to increase the temperature accordingly. The component gas flows and reactor pressure were as follows:

$$\begin{aligned}
 CH_4 &= 490 \text{ ml} \cdot \text{min}^{-1} \\
 O_2 &= 410 \text{ ml} \cdot \text{min}^{-1} \quad C/O = 0.6 \\
 He \text{ (Ar)} &= 100 \text{ ml} \cdot \text{min}^{-1} \\
 p_{\text{reactor}} &= 1100 - 1200 \text{ mbar}
 \end{aligned}$$

With these gas flows the reactor temperature could be varied between $1000\text{ }^{\circ}\text{C}$ (autothermal operation) and $1300\text{ }^{\circ}\text{C}$ (upper pyrometer temperature limit). In Fig. 4.23 five temperature profiles under different conditions are shown.

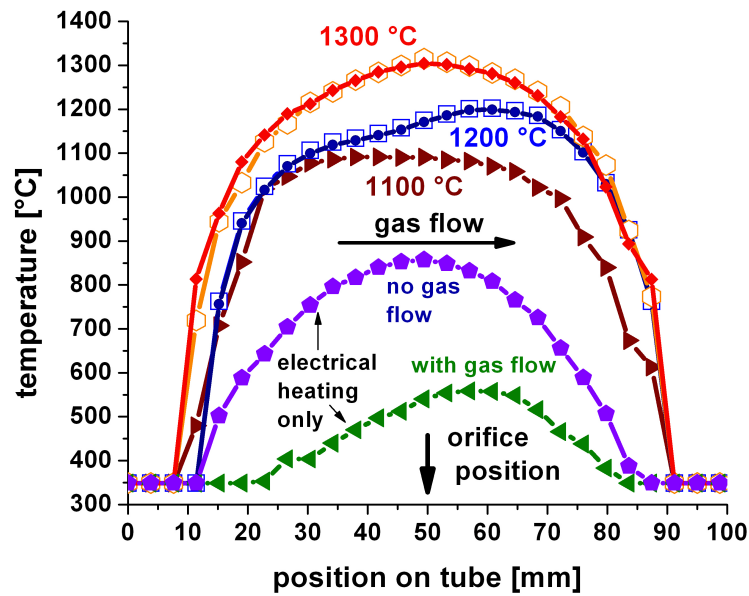


Figure 4.23: Axial temperature profiles for different maximum temperatures at $C/O = 0.6$ and $\dot{F}_{total} = 1000\text{ ml} \cdot \text{min}^{-1}$.

If the tube was only heated electrically and no gas was flown through it, a symmetrical temperature profile with a maximum at 50 mm of about $850\text{ }^{\circ}\text{C}$ resulted ('electrical heating only - no gas flow'). With gas flow convective heat transport lowered the maximum wall temperature ($550\text{ }^{\circ}\text{C}$) and shifted the temperature maximum in flow direction (60 mm). As ignition occurred between $550\text{ }^{\circ}\text{C}$ and $600\text{ }^{\circ}\text{C}$ the curve ('electrical heating only - with gas flow') presents a temperature profile right before ignition. After ignition and turning off the electrical heating, the reactor operated autothermally with a plateau from $25 - 65\text{ mm}$ slightly above $1000\text{ }^{\circ}\text{C}$ (curve not shown). Apart from a vertical offset, the shape of the profile did not change by increasing the maximum temperature to $1100\text{ }^{\circ}\text{C}$. At both temperatures, $1000\text{ }^{\circ}\text{C}$ and $1100\text{ }^{\circ}\text{C}$, the profile was rather flat and the temperature maximum was located close to the inlet where fresh reactants entered the tube. This implies a very high reaction rate as can be expected for methane oxidation on platinum. In contrast,

a further increase in temperature to about 1200 °C altered the temperature profile dramatically by generating a pronounced temperature maximum close to the tube outlet. The fact that the inlet temperature profile up to 30 mm remained unchanged indicates that this maximum is caused by additional exothermic reaction in the second half of the tube. Further heating to 1300 °C restored the symmetry of the profile around a maximum at 50 mm. To illustrate that the reaction produces a highly reproducible temperature profile, a second 1300 °C profile is shown in Figure 4.23 which was measured after several hours time on stream. Both profiles are nearly identical.

4.4.1 Product Gas Composition at $C/O = 0.6$

The measurement of stable product and reactant species was accomplished by gas chromatography. The selectivities given in this work have to be taken as integral selectivities after nearly the complete consumption of oxygen (reaction limiting component) at the reactor outlet. They are not suitable to evaluate reaction rates etc. but will indicate changes in the reaction mechanism itself. The same is true for the given conversions. Detailed kinetic experiments will follow in the future.

Figure 4.24 shows the conversion of methane and oxygen for the high temperature methane oxidation at $C/O = 0.6$:

Between 1000 °C and 1100 °C the oxygen conversion stayed nearly constant at about 85 %. The methane conversion increased in the same temperature range slightly from 46 % to 50 %. As shown by the product selectivities in Figure 4.25, the reactants are mainly converted to H_2O , CO , CO_2 and H_2 . It can be clearly seen that the selectivity to partial oxidation products CO and H_2 increases from 1000 °C and 1100 °C whereas that to CO_2 and H_2O decreases. This is in line with the earlier presented ignition studies (Section 4.3.1) and explains the slightly increasing CH_4 conversion in this range. The selectivity to coupling products (C_2H_6 , C_2H_4 , C_2H_2), summarized as C_2 in Fig. 4.25, is less than 1 % for temperatures below 1100 °C.

The incomplete O_2 conversion in the temperature range 1000 – 1100 °C is in contrast to most studies in literature, where oxygen is fully consumed at the reactor exit. The major different between literature and this study is the form of the catalyst.

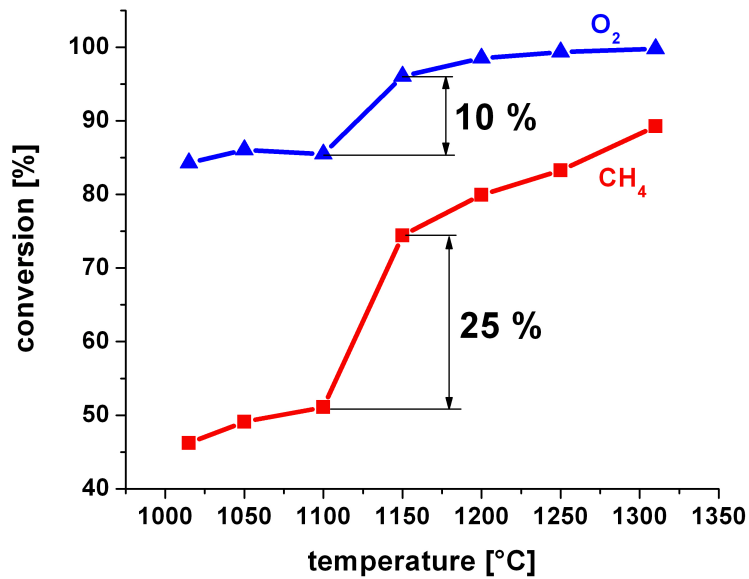


Figure 4.24: Oxygen and methane conversions as function of temperature at $C/O = 0.6$ and $\dot{F}_{total} = 1000 \text{ ml} \cdot \text{min}^{-1}$.

Other groups used mostly foams [34] or small channel monoliths [19] with hydraulic channel diameters in the range of a few $100 \mu\text{m}$. and gas hourly space velocities up to $4.4 \cdot 10^5 \text{ h}^{-1}$. In the present work, a *Pt* tube with a rather large diameter of 4.4 mm was used with a GHSV not higher than 100000. In this case, mass transport in radial direction is limited to diffusion and the characteristic O_2 diffusion times are in the range of the characteristic convection times through the tube leading to oxygen breakthrough (cf. Section 4.2.2). Keeping this picture in mind, the gas phase O_2 profile in the tube can be rationalized as shown in Figure 4.26.

The O_2 concentration in the gas stream will decrease in flow direction due to O_2 consumption at the wall. As diffusion limits the transport from the tube center to the *Pt* surface a pronounced radial O_2 profile will develop. The centerline stream will always contain more oxygen than the near surface region which is depicted in Fig. 4.26 by imaginary cuts close to the tube entrance (A), in the middle of the tube (B) and close to the tube exit (C). As the surface reactions are very fast oxygen is nearly fully consumed next to the wall. Of course, this derived picture is only qualitative, but it is supported by the data shown for $C/O = 0.6$, by the data shown later for other C/O ratios (Section 4.5) and by the calculations presented in Section 4.2.2.

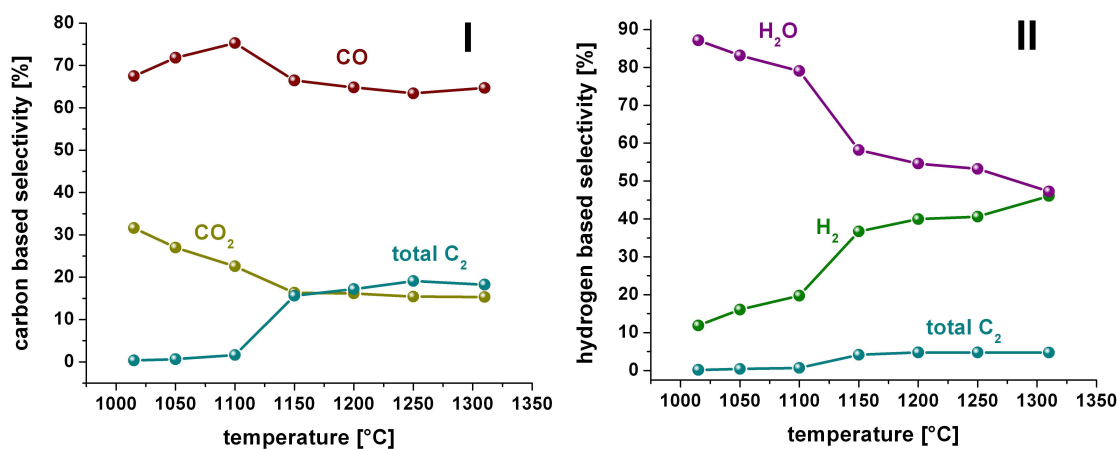


Figure 4.25: Product selectivities as function of temperature at $C/O = 0.6$ and $\dot{F}_{total} = 1000 \text{ ml} \cdot \text{min}^{-1}$. In **I** the carbon based selectivities are shown, in **II** the hydrogen based one. The H_2O molecular flow was calculated in respect to the hydrogen balance.

The trend of reactant conversion and product selectivities found between $1000 \text{ }^\circ\text{C}$ and $1100 \text{ }^\circ\text{C}$ is drastically interrupted if the temperature is increased above $1100 \text{ }^\circ\text{C}$. If the temperature is increased to $1150 \text{ }^\circ\text{C}$ a step like increase of O_2 and CH_4 conversion by 10% and 25% occurs respectively. At $1150 \text{ }^\circ\text{C}$ the O_2 conversion amounts to about 95% and approaches 100% above $1200 \text{ }^\circ\text{C}$. A step like change is also observed for the product selectivities. By going from $1100 \text{ }^\circ\text{C}$ to $1150 \text{ }^\circ\text{C}$ H_2 selectivity increases from 18% to 38% and H_2O selectivity drops from 80% to 55% . Most remarkable is the sudden onset of C_2 formation going from less than 1% at $1100 \text{ }^\circ\text{C}$ to about 15% $1150 \text{ }^\circ\text{C}$.

Surprisingly the selectivity to CO formation decreases by going from $1100 \text{ }^\circ\text{C}$ to $1150 \text{ }^\circ\text{C}$ which is against the thermodynamic trend favoring CO formation at high temperatures. As also the CO_2 selectivity drops, Fig. 4.25 might misleadingly indicate that the C_2 hydrocarbons are formed at the expense of CO and CO_2 . This is actually not the case. The CO and CO_2 selectivities drop between $1100 \text{ }^\circ\text{C}$ and $1150 \text{ }^\circ\text{C}$ because the methane conversion increases by 25% . If the CO and CO_2 molar flow rates are plotted against temperature instead of selectivities (Figure 4.27) it becomes clear that CO and CO_2 are actually produced above $1150 \text{ }^\circ\text{C}$. This behavior is attributed to ignition of gas phase reactions at about $1150 \text{ }^\circ\text{C}$ converting the remaining gas phase O_2 in the tube center and more CH_4 to CO_x , H_2 and C_2 coupling products. Parallel, CH_4 continues to be oxidized at the Pt surface with a

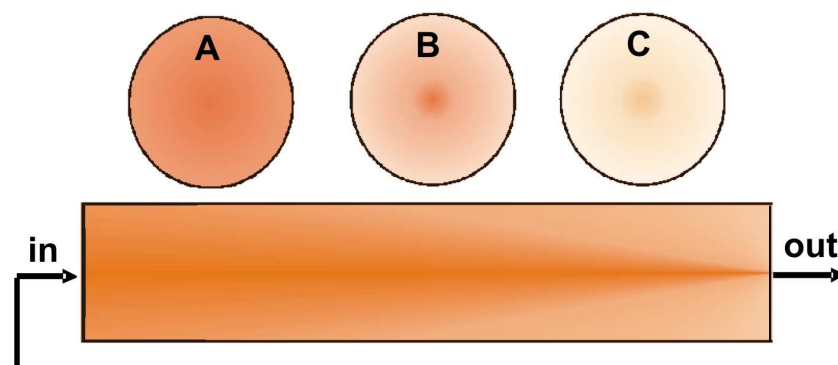


Figure 4.26: Estimated O_2 concentration profile as result of convective axial O_2 transport, radial O_2 diffusion and catalytic O_2 conversion at the Pt tube wall: (A) Radial O_2 profile close to entrance; (B) Radial O_2 profile in tube middle; (C) Radial O_2 profile close to tube exit.

product spectrum following the trends observed between $1000\text{ }^\circ C$ and $1100\text{ }^\circ C$.

4.4.2 Radical Detection and Quantification at $C/O = 0.6$

As discussed in Section 2.1.2, the oxidative coupling of methane is often believed to occur via recombination of methyl radicals in the gas phase. With Molecular Beam Mass Spectrometry and threshold ionization it was now possible for the first time to screen the gas phase above the catalyst for radicals at temperatures up to $1300\text{ }^\circ C$ and atmospheric pressure. All previous studies were limited to much lower temperatures ($725\text{ }^\circ C$) and pressures (1 Torr - cf. [36]).

From the results presented in Section 4.4.1, it could be expected that ignition of gas phase chemistry occurred somewhere between $1100\text{ }^\circ C$ and $1150\text{ }^\circ C$ for $C/O = 0.6$. Both, in the plot of reactant conversion vs. temperature and product selectivity vs. temperature (Fig. 4.24 and Fig. 4.25 respectively), a discontinuity was observed in this temperature range. As shown in Fig. 4.28, also the shape of the temperature profile changed significantly if the temperature maximum of the tube was increased from $1100\text{ }^\circ C$ to $1200\text{ }^\circ C$. The pronounced temperature maximum highlighted as shaded area in Fig. 4.28 indicated heat liberation by additional exothermic oxidation reactions. To verify the assumption that all these discontinuities were caused by gas phase reactions, threshold ionization measurements were performed to search for

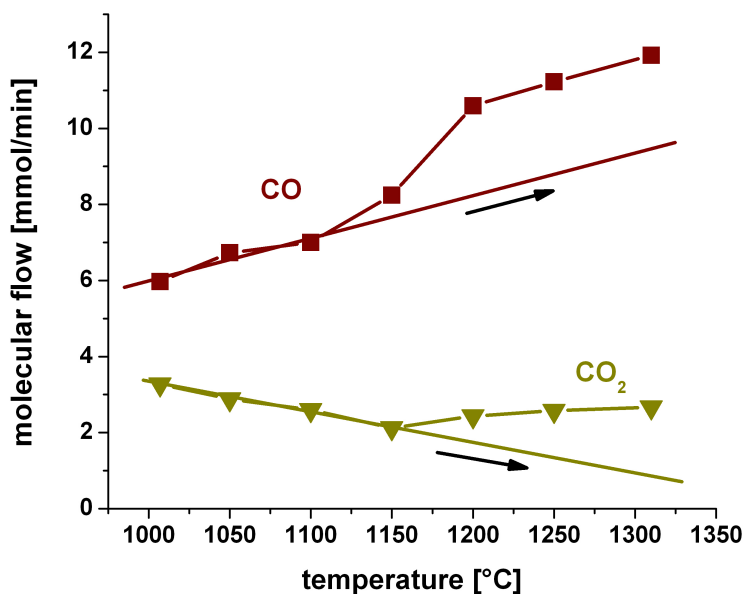


Figure 4.27: Molecular flow rates of CO and CO_2 as function of temperature at $C/O = 0.6$ and $\dot{F}_{total} = 1000 \text{ ml} \cdot \text{min}^{-1}$. At $1150 \text{ }^\circ\text{C}$ an additional production of CO_x is observed.

gas phase radicals in the temperature range between autothermal operation ($T_{max} = 1015 \text{ }^\circ\text{C}$) and the maximum temperature of $T_{max} = 1310 \text{ }^\circ\text{C}$. The parameters for the threshold ionization measurements were as follows:

$$\begin{aligned}
 \text{mass range} &= 0.4 \text{ to } 50 \text{ amu} \\
 \text{ionization energy} &= 9 \text{ to } 25 \text{ eV} \\
 \text{electron current} &= 100 \text{ } \mu\text{A} \\
 \text{dwell time} &= 10 \text{ ms} \\
 \text{settle time} &= 10 \text{ ms}
 \end{aligned}$$

For each ionization energy, a full mass spectrum was recorded ($0.4 - 50 \text{ amu}$). As described in Chapter 4.1.5, IE curves were created by integrating the peaks and plotting the peak area over the ionization energy (IE).

Apart from $CH_3\cdot$ radicals at 15 amu , no other radicals were detected in these or any later discussed measurements. Figure 4.29 shows the IE curves at 15 amu for autothermal reactor operation (blue dots; $T_{max} = 1015 \text{ }^\circ\text{C}$) and for the maximum temperature possible (red dots; $T_{max} = 1310 \text{ }^\circ\text{C}$). The insets show the corresponding

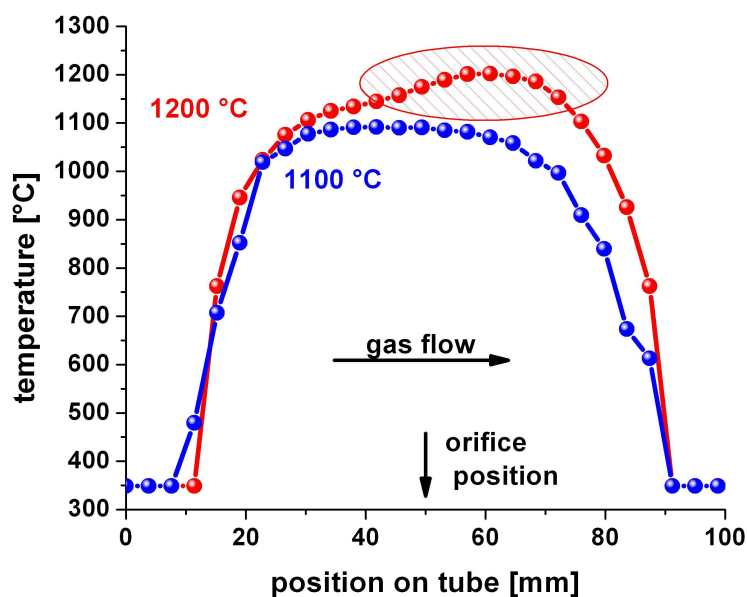


Figure 4.28: Temperature profiles at maximum tube temperatures of 1100 °C and 1200 °C respectively at $C/O = 0.6$. The pronounced maximum (shaded area) in the 1200 °C profile is attributed to heat liberation by exothermic gas phase oxidation reactions.

mass spectra at an ionization energy of 11.9 eV which was high enough to ionize methyl radicals but too low to generate interfering fragment ions at 15 amu.

At $T_{max} = 1015$ °C no signal is observed at $m/z = 15$ amu and 11.9 eV ionization energy. The IE plot has its onset at about 14 eV which corresponds to CH_3^+ formation by methane fragmentation in the ionizer of the MS ($CH_4^+ \rightarrow CH_3^+ + H\cdot$). The same result was obtained at $T_{max} = 1050$ °C and $T_{max} = 1100$ °C. In contrast, the IE measurements at 1310 °C reactor temperature showed clearly the presence of $CH_3\cdot$ radicals. The mass spectrum at 11.9 eV shows an intense peak at 15 amu evidencing $CH_3\cdot$ radical ionization ($CH_3\cdot \rightarrow CH_3^+$) as methane is not yet ionized at 11.9 eV (negligible peak at 16 amu). The IE plot rises from 9.8 eV which corresponds to the ionization potential of $CH_3\cdot$ radicals. The step increase of the slope of the IE curve at 14 eV corresponds again to the fragmentation of residual methane. Therefore $CH_3\cdot$ radicals could be clearly detected at $T_{max} = 1310$ °C which agrees well with the detection of C2 products (C_2H_6 , C_2H_4 , C_2H_2) in the reactor effluent stream.

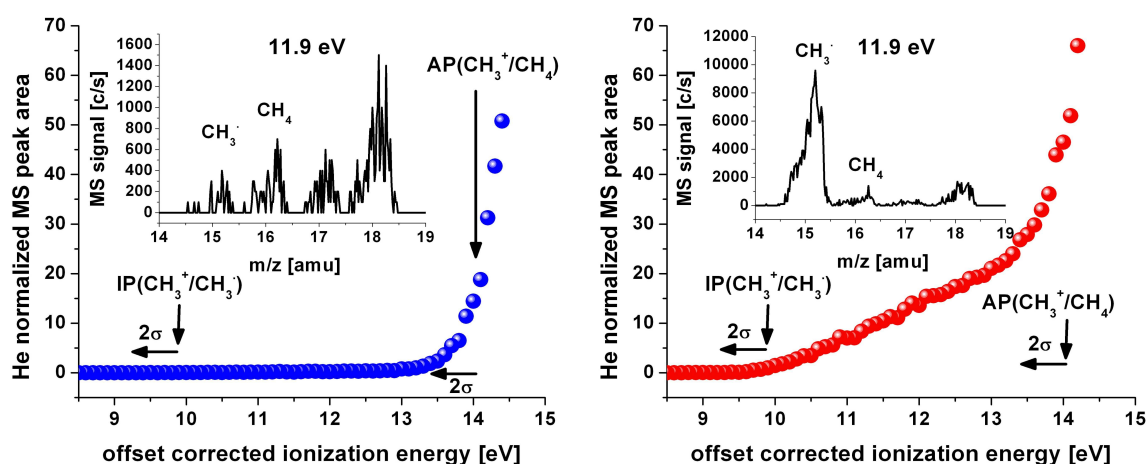


Figure 4.29: Left: Threshold ionization IE curve at 1015 °C showing no signal increase at 9.8 eV. The curve onset at 14 eV corresponds to methane fragmentation ($CH_4^+ \rightarrow CH_3^+ + H\cdot$) in the MS ionizer. The inset represents a mass spectrum at 11.9 eV showing nearly no signal at $m/z = 15$. No $CH_3\cdot$ radicals were detected. Right: Threshold ionization IE curve at 1310 °C. The onset at 9.8 eV corresponds to ionization of $CH_3\cdot$ radicals. The inset represents a mass spectrum at 11.9 eV showing a high peak at $m/z = 15$ but nearly no ionization of CH_4 at 16 amu.

By application of the radical quantification method described in Section 4.1.4 it was now possible to calculate for each temperature the $CH_3\cdot$ radical flow rate at the sampling position. The results are shown in Fig. 4.30 together with the selectivity to C_2H_6 , C_2H_4 , C_2H_2 and C_2 total measured at the reactor outlet. The conversion of CH_4 to C_2 coupling products is indeed connected to the presence of $CH_3\cdot$ radicals in the gas phase. Even though a parallel production of C_2 species and $CH_3\cdot$ radicals can not be totally excluded a consecutive reaction is most likely. At temperatures ≤ 1100 °C, where virtually no $CH_3\cdot$ radicals were detected, the selectivity to C_2 coupling products was close to zero. Above 1100 °C, where the gas phase reactions started, the methyl radical flow rate increased exponentially accompanied by a step increase in C_2 selectivity. Even if a quantitative correlation between $CH_3\cdot$ radical formation and C_2 product selectivity can not be established due to the different sampling positions (tube center vs. tube exit respectively) and the dependence of the measured $CH_3\cdot$ radical flow on the location of the tube temperature maximum, the qualitative connection is evident.

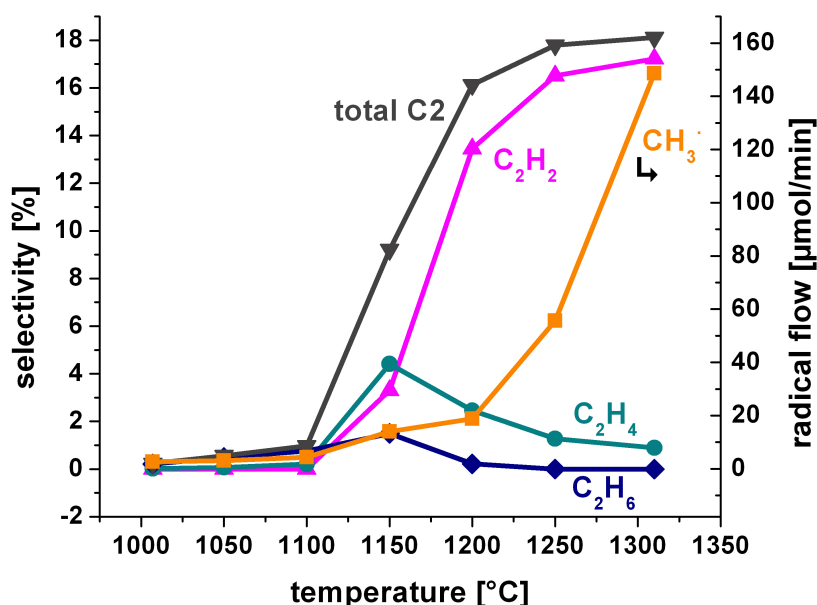
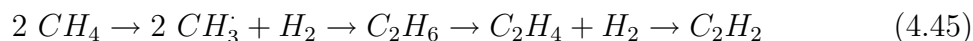


Figure 4.30: Methyl radical flow rates measured at the tube center and selectivities to C_2H_6 , C_2H_4 and C_2H_2 measured at the tube outlet as function of temperature.

As gas phase oxidation and pyrolysis reactions proceed via a network of radical reactions (cf. Section 2.1.3) it is very likely that the methyl radicals are generated in the gas phase either by oxygen assisted hydrogen abstraction from methane ($CH_4 + O_2 \rightarrow CH_3\cdot + HO_2\cdot$) or by homolytic $C - H$ cleavage upon collision with an inert collision partner M ($CH_4 + M \rightarrow CH_3\cdot + H\cdot + M$). The $CH_3\cdot$ radicals then recombine to C_2H_6 followed by dehydrogenation to C_2H_4 and C_2H_2 . The formation of $CH_3\cdot$ radicals at the Pt surface followed by desorption into the gas phase seems very unlikely, as noticeable $CH_3\cdot$ formation should already begin at autothermal operation and increase with temperature. It is hard to believe that the surface chemistry changes so drastically by increasing the temperature above 1100 °C. The small amount of ethane detected by GC at the reactor outlet before $CH_3\cdot$ radicals could be detected by the MBMS can be explained by $CH_3\cdot$ concentrations below the detection limit which is in the low *ppm* range (Section 4.1.5). Small amounts of $CH_3\cdot$ and other radicals are probably formed before gas phase radical reactions start but remain undetected because of their low concentration. The results observed here are the first experimental verification of the numerical predictions by Quiceno

et al. [43] which predicted that C_2 products are exclusively formed in the gas phase and that exothermic surface oxidations are only providing heat to drive the gas phase chemistry.

The product distribution between the three possible C_2 hydrocarbons C_2H_6 , C_2H_4 and C_2H_2 shown in Fig. 4.30 follows a clear trend. At temperatures ≤ 1100 °C, where only traces of C_2 products are observed, ethane is formed preferentially. Ethylene is the favored C_2 product in a medium temperature range between 1100 °C and 1200 °C whereas acetylene dominates above 1200 °C. This trend follows closely the thermodynamic stability trend of C_2 hydrocarbons observed in methane pyrolysis shown in Fig. 4.31 taken from Reference [130]. Even though the reaction mixture leaving the tube is probably not in thermodynamic equilibrium the product distribution indicates that the gas phase chemistry in the O_2 depleted tube section resembles that of methane pyrolysis described by Eq. 4.45 [131]:



The production of H_2 described by Eq. 4.45 is also in agreement with the increasing H_2 selectivity upon onset of gas phase chemistry (cf. Fig. 4.25).

The experimentally determined $CH_3\cdot$ radical flow rates are in reasonable agreement to unpublished numerical simulations of the methane oxidation in a Pt tube conducted by K. A. Williams at the Department of Chemical Engineering & Materials Science at the University of Minnesota, USA, using the CRESLAF code of CHEMKIN [132]. To model the surface chemistry, Williams used a surface kinetic model published by O. Deutschmann et al. [42]. The kinetic gas phase model was taken from work published by Mims et al. [133]. Even though the reaction conditions simulated by Williams ($C/O = 1.0$, $v_{inlet} = 200$ cm \cdot s $^{-1}$, $T_{inlet} = 1173$ K, inert N_2 , $N_2/O_2 = 3.76$ adiabatic reactor) were different from the conditions used in the experiment ($C/O = 0.6$, $v_{inlet} = 110$ cm \cdot s $^{-1}$, $T_{inlet} = 298$ K, inert Ar , $Ar/O_2 = 0.25$, heat losses by conduction and radiation) the calculated maximum $CH_3\cdot$ mole fraction in the tube $X_{CH_3\cdot}^{calc,max} = 1.25 \cdot 10^{-3}$ is of the same order of magnitude as the experimentally observed mole fraction at 1583 K of about $X_{CH_3\cdot}^{exp.} \approx 3 \cdot 10^{-3}$. The predicted 2D temperature and $CH_3\cdot$ mole fraction profiles up to the sampling position at 5 mm are shown in Fig. 4.32 and Fig. 4.33 respectively. Because of radial symmetry, only half of the tube cross section is shown. Even more interesting than this apparent

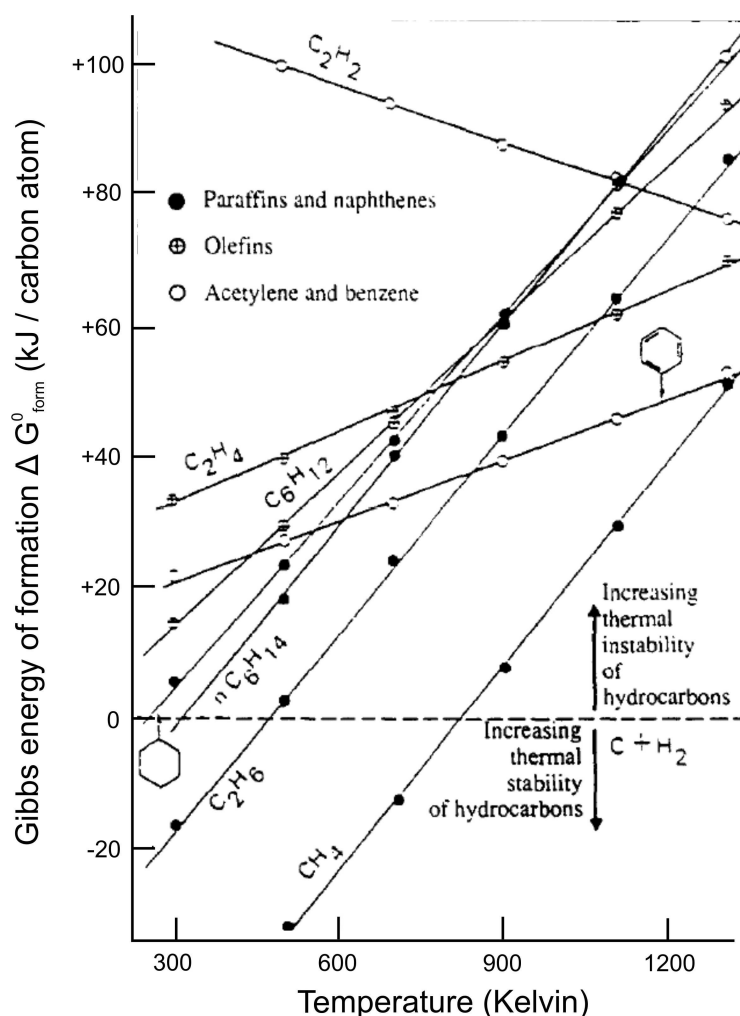


Figure 4.31: Stability of different hydrocarbons in methane pyrolysis - adopted from [130].

agreement is that the steady state concentration of all other radical species were predicted to be lower than the detection limit of the MBMS method (Section 4.1.5). Indeed even though it was searched for other radicals as $CH_x\cdot$, $C_2H_x\cdot$ and $C_3H_x\cdot$, as well as $H\cdot$ and oxygen containing radicals, not other than $CH_3\cdot$ could be detected experimentally. The observation of the thermodynamically stablest products confirms pyrolysis (cf. 2.1.3) as the main C2 forming mechanism. The non-catalytic oxidation of methane seems to lead to additional total oxidation products due to the very low stability of any oxygen containing intermediate. Nevertheless generated $OH\cdot$ and $H\cdot$, as well as $CH_3\cdot$ may contribute to radical chain reactions.

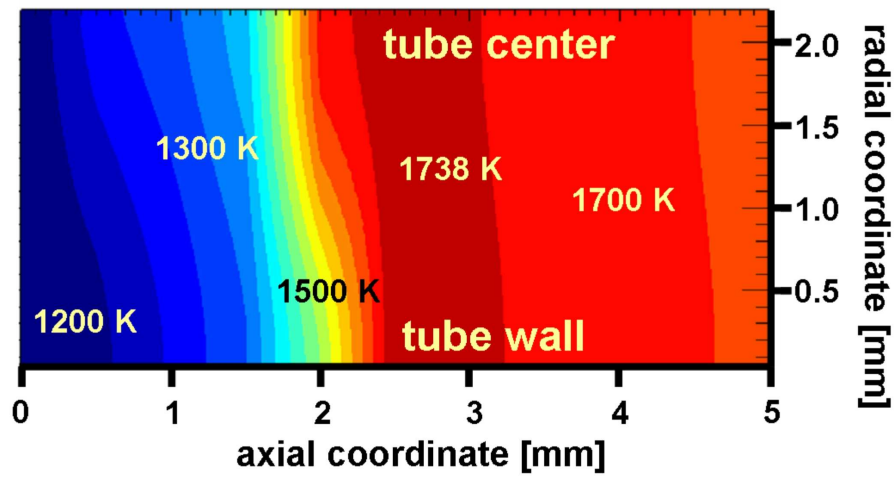


Figure 4.32: Calculated 2D temperature profile in the Pt tube up to the sampling position at 5 mm.

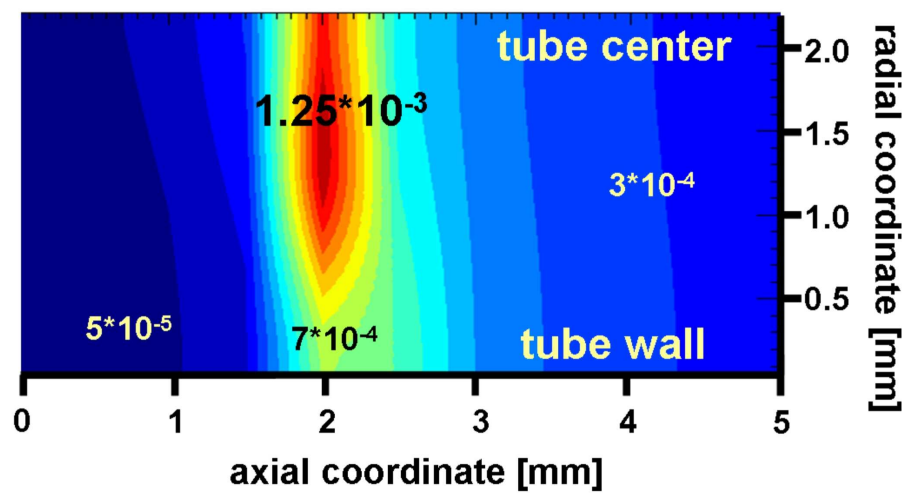


Figure 4.33: Calculated 2D $CH_3\cdot$ radical profile in the Pt tube up to the sampling position at 5 mm.

4.4.3 Unsaturated Higher Hydrocarbons at $C/O = 0.6$

Further support of the theory that the C_2 products are formed via gas phase reactions comes from the simultaneous appearance of highly unsaturated higher hydrocarbons. Even though these hydrocarbons are not interesting as products themselves and as soot precursors rather unwanted in practical application [134], their structures can give insight into the radical chemistry in the gas phase.

Fig. 4.34 shows a chromatogram with peaks eluting between 9 – 10 *min* and 12 – 14 *min* which, based on their retention times, can be attributed to hydrocarbons containing three and four C - atoms respectively. The structure of these unknown hydrocarbons could not be identified by normal GC calibration, as none of the available calibration species showed a matching retention time. An identification by the MBMS was also not possible as the fragmentation patterns of these species were strongly overlapping. Threshold ionization could not be used as the ionization energies were too close together. The structures of the unknown hydrocarbons were finally identified by employing the GC-MS technique described in Section 4.1.7. Some ten *ppm* of each hydrocarbon were sufficient for reliable identification. The concentration of each species was estimated from the GC data.

Fig. 4.35 shows the measured fragmentation pattern for each of the four unknown GC peaks. Reference spectra at 70 *eV*, taken from the NIST database [135], are shown in the insets. Small intensity differences between groups of peaks separated by several *amu* in the mass spectra might occur due to the transient nature of the sampled GC peak. However, the intensity distribution within a group of peaks was only little affected. Background correction was done by subtracting an average of five to ten MS spectra from a GC peak free region next to the analyzed peak. In cases where spurious peaks remained in the spectra due to incomplete correction for signals arising from background gases such as CO_2 (44 *amu*), CO/N_2 (28 *amu*), O_2 (32 *amu*), CH_4 and H_2O (15 – 19 *amu*) they are marked with stars in Fig. 4.35.

Based on this analysis, the GC peaks at 13.4 *min* and 12.6 *min* could be clearly assigned to 1,3-butadiyne and 1-butene-3-yne respectively (Fig. 4.35 a) and b)). The GC peaks at 9.8 *min* and 9.6 *min* could be assigned to propyne and allene respectively (Fig. 4.35 c) and d)). Due to their similar fragmentation pattern of the peaks

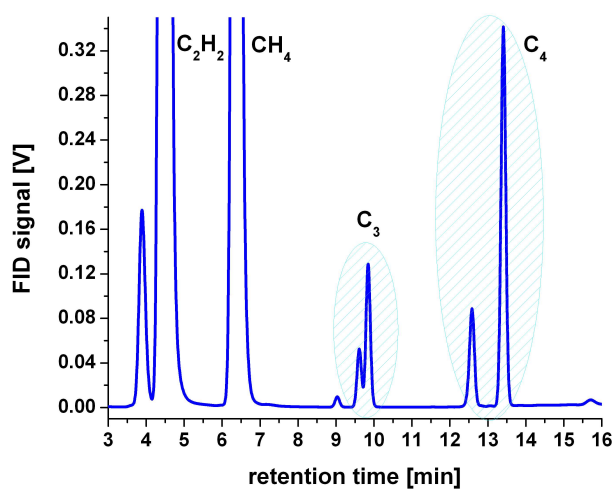


Figure 4.34: Gas chromatogram at $C/O = 0.6$ and 1300°C showing peaks of unknown C_3 and C_4 hydrocarbons.

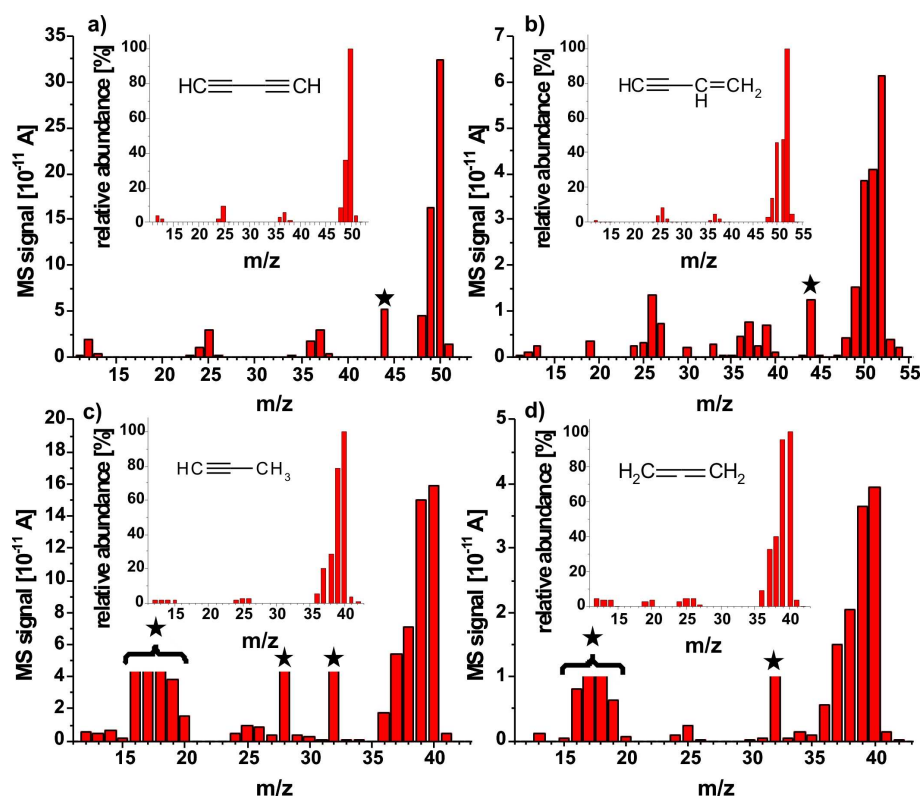


Figure 4.35: Fragmentation pattern of: a.) 1,3-butadiyne at 13.4 *min*; b.) 1-butene-3-yne at 12.6 *min*, c.) propyne at 9.8 *min* and d.) allene at 9.6 *min*. The insets represent reference spectra from NIST [135].

from 36 – 41 *amu* the discrimination of the latter was backed by reference chromatograms [136].

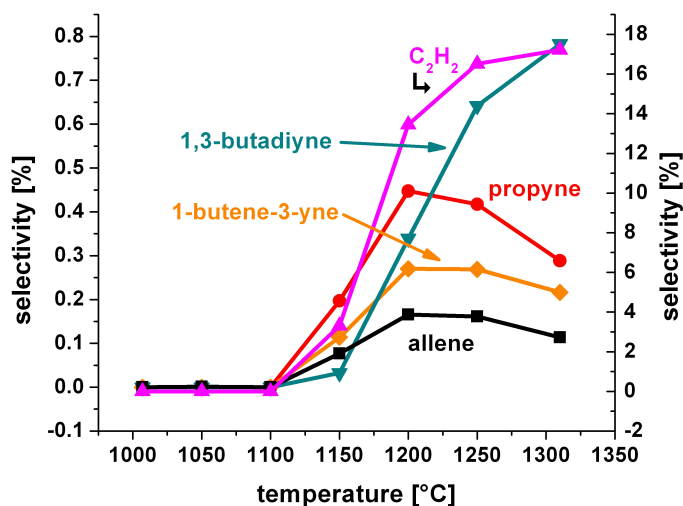
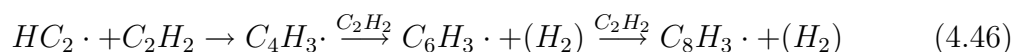


Figure 4.36: Temperature dependent selectivities for C3 and C4 hydrocarbons at a $C/O = 0.6$.

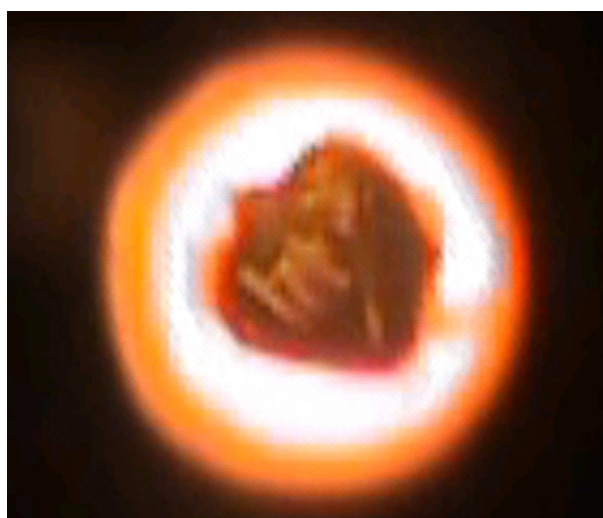
Fig. 4.36 shows the selectivities for the C3 and C4 hydrocarbons with increasing temperature at $C/O = 0.6$. None of these coupling products is observed below 1100 °C, i.e. before gas phase oxidation processes have started. Their formation coincides with the appearance of methyl radicals in the gas phase. From flame and pyrolysis studies it is known, that acetylene plays a major role in the soot formation process. The reaction of acetylene with a formed ethynyl ($HCC\cdot$) radical is the source for polyacetylenes [137]:



Release of one $H\cdot$ atom from $C_4H_3\cdot$ by β -scission leads to formation of 1,3-butadiyne. Contrary, the addition of one $H\cdot$ to $C_4H_3\cdot$ leads to 1-butene-3-yne. Both molecules were found in the reaction mixture. The absence of the radicals in the threshold ionization measurements results from their low concentration. As the stable, unsaturated C4 compounds were only formed in concentrations of about 100 ppm, the radicals precursors $C_2H\cdot$ and $C_4H_3\cdot$ are below the detection limit of the method.

In flames the formation of the first aromatic ring is one of the key steps in the soot formation mechanism [138]. Whereas benzene formation by trimerization of

acetylene has been observed on single crystals [139], a more general mechanism of benzene formation seems to involve reaction between C_4 and acetylene [7, 140] or two propargyl radicals ($C_3H_3\cdot$) [141]. The importance of one of these mechanisms in the Pt tube experiments can not be clearly specified as C_4 and C_3 precursor molecules are present in relatively equal amounts but benzene is indeed formed upon ignition of gas phase chemistry.



5 mm

Figure 4.37: Occurrence of flames in the Pt tube at $1300\text{ }^\circ C$ and $C/O = 0.6$. View through the tube.

In summary, all data presented in Section 4.4 support the mechanistic picture that methane oxidation under O_2 rich conditions ($C/O = 0.6$) can proceed through heterogeneous (surface) and homogeneous (gas phase) reactions. At temperatures below $1100\text{ }^\circ C$ the oxidation reactions are bound to the surface and typical product mixtures consisting of CO_2 , CO , H_2O and H_2 are observed. Due to the finite rate of O_2 diffusion to the Pt surface, O_2 remains present at the tube center and gas phase oxidation reactions are initiated if the temperature is raised above $1100 - 1150\text{ }^\circ C$. This initiation is accompanied by the formation of flames inside the tube (Fig. 4.37) and a distinct increase in CO and CO_2 production is observed. Furthermore, the start of gas phase chemistry goes along with the formation of $CH_3\cdot$ radicals, C_2 coupling products, highly unsaturated C_3 and C_4 molecules and even benzene. This product

spectrum indicates a complex network of gas phase oxidation-, radical coupling- and pyrolysis reactions, whereas pyrolysis seems to play a leading part for the coupled hydrocarbon species.

4.5 Catalytic Partial Oxidation of Methane - variable C/O Ratios and Gas Flows

After discussing in detail the results for methane oxidation at $C/O = 0.6$ and temperatures up to $1310\text{ }^{\circ}\text{C}$, the results for other C/O ratios and flow rates are presented and discussed in the following. Unfortunately, C/O ratios higher than 0.6 could not be investigated up to the maximum temperature of about $1300\text{ }^{\circ}\text{C}$ as the available heating power was limited. At $C/O = 2.0$, the highest investigated C/O in this work, the maximum achievable temperature was $1100\text{ }^{\circ}\text{C}$. For this reason, all experiments discussed in Section 4.5 were conducted with a maximum tube temperature of $1100\text{ }^{\circ}\text{C}$. Three different C/O ratios of 0.6, 1.0 and 2.0 were investigated at two different flow rates - $500\text{ ml}\cdot\text{min}^{-1}$ and $1000\text{ ml}\cdot\text{min}^{-1}$. The experimental conditions are summarized in Table 4.11.

Table 4.11: Experimental conditions for variable C/O experiments

| flow [$\text{ml}\cdot\text{min}^{-1}$] | $1000\text{ ml}\cdot\text{min}^{-1}$ | | | $500\text{ ml}\cdot\text{min}^{-1}$ | | | $1300\text{ ml}\cdot\text{min}^{-1}$ |
|--|--------------------------------------|-----|-----|-------------------------------------|-----|-----|--------------------------------------|
| | C/O | | | C/O | | | C/O |
| | 0.6 | 1.0 | 2.0 | 0.6 | 1.0 | 2.0 | 0.6 |
| CH_4 | 500 | 596 | 725 | 255 | 303 | 365 | 600 |
| O_2 | 416 | 306 | 194 | 217 | 154 | 92 | 500 |
| Ar | 106 | 103 | 109 | 52 | 52 | 53 | 200 |

4.5.1 Temperature Profiles for variable C/O Ratios

Figure 4.38 shows exemplarily the temperature profiles for $C/O = 0.6, 1.0$ and 2.0 at a volumetric inlet flow rate of $500\text{ ml}\cdot\text{min}^{-1}$. The electrical heating powers to achieve a tube temperature maximum of $1100\text{ }^{\circ}\text{C}$ are also listed. The temperature profiles

are a convolution of the heating power profile, due to the gas flow shifted in outlet direction, and the heat release by oxidation reactions near the inlet. It is clearly seen that with increasing C/O ratio (decreasing O_2 concentration) less heat is produced by exothermic surface oxidation reactions leading to an alleviated temperature increase and a downstream shifted temperature maximum, as the heating power increases strongly. The curves overlap only by chance in one point, which is even not the case at flow rates of $1000 \text{ ml} \cdot \text{min}^{-1}$.

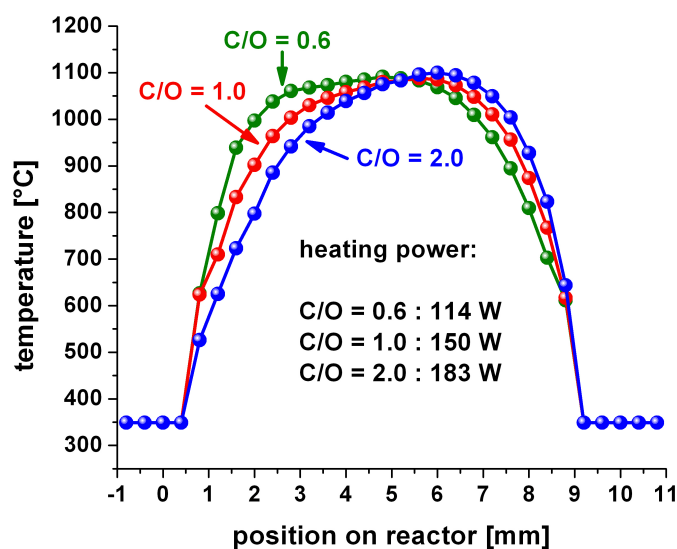


Figure 4.38: Temperature profiles for variable C/O ratios (0.6, 1.0, 2.0) at $1100 \text{ }^\circ\text{C}$ tube temperature maximum and $500 \text{ ml} \cdot \text{min}^{-1}$ inlet flow rate.

4.5.2 Conversions and Selectivities for variable C/O Ratios

Conversion plots for oxygen and methane at $C/O = 0.6, 1.0$ and 2.0 at 500 and $1000 \text{ ml} \cdot \text{min}^{-1}$ volumetric inlet flow rate are shown in Figure 4.39. As can be seen, 100% O_2 conversion is only achieved at $C/O = 0.6$ and at a flow rate of $500 \text{ ml} \cdot \text{min}^{-1}$. It will be reasoned in Section 4.5.3 that also this situation corresponds to the ignition of gas phase reactions. At any other C/O ratio and for $C/O = 0.6$ also at $1000 \text{ ml} \cdot \text{min}^{-1}$, O_2 conversion is incomplete and depends only weakly on the C/O ratio. This can be understood as O_2 is the stoichiometrically limited component

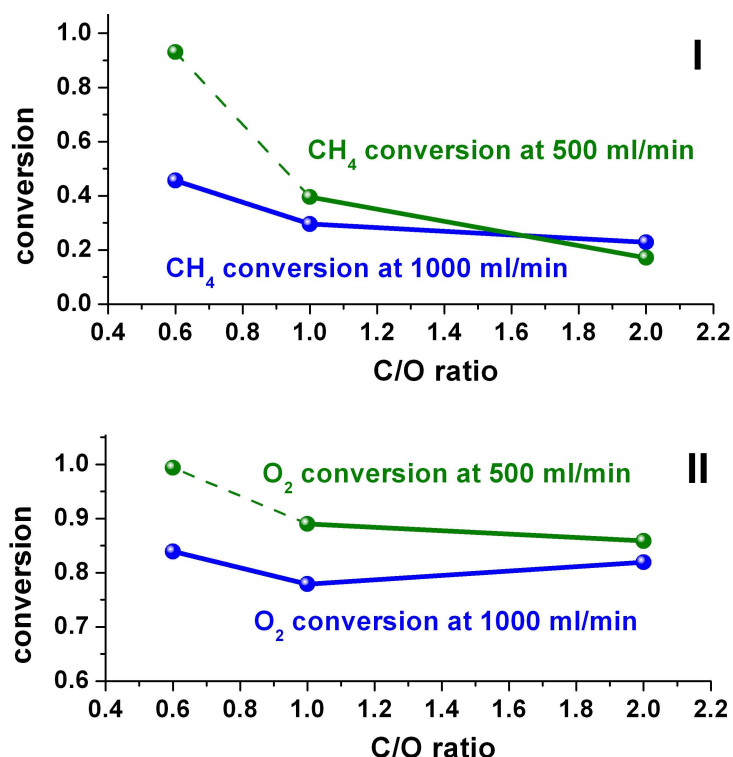


Figure 4.39: CH_4 I and O_2 II conversions with variable C/O ratios. For a C/O of 0.6 and a flow rate of $500 \text{ ml} \cdot \text{min}^{-1}$ gas phase reactions were observed.

at all investigated C/O ratios and its conversion at the tube wall depends rather on the ratio of axial convection to radial diffusion (cf. Section 4.2) than on C/O . As the residence time of O_2 doubles by going from $1000 \text{ ml} \cdot \text{min}^{-1}$ to $500 \text{ ml} \cdot \text{min}^{-1}$ but the diffusion coefficient remains roughly constant, O_2 conversion is higher at the lower flow rate. However, complete O_2 conversion is only observed if gas phase oxidation reactions occur.

The experiments at different C/O ratios and flow rates allow also to draw supporting conclusions with respect to the stepwise dehydrogenation mechanism for the formation of C_2 hydrocarbons. In these experiments, C_2 hydrocarbons are either produced by gas phase oxidation reactions before ignition, at $C/O = 0.6$ and $500 \text{ ml} \cdot \text{min}^{-1}$ also after ignition, or by pyrolysis reactions in close vicinity to the catalytic wall in an O_2 depleted atmosphere (cf. Fig. 4.26). Fig. 4.40 shows the C_2 selectivities at $1000 \text{ ml} \cdot \text{min}^{-1}$ and Fig. 4.41 at $500 \text{ ml} \cdot \text{min}^{-1}$ inlet flow rate respectively. As described already in Section 4.4.1 the total C_2 selectivity at $C/O = 0.6$

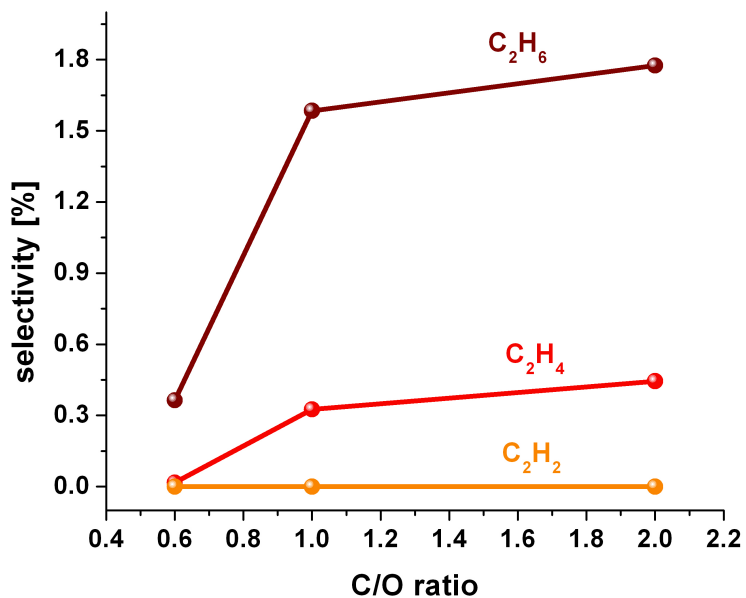


Figure 4.40: C₂ selectivities for variable C/O at $1000 \text{ ml} \cdot \text{min}^{-1}$ inlet flow rate.

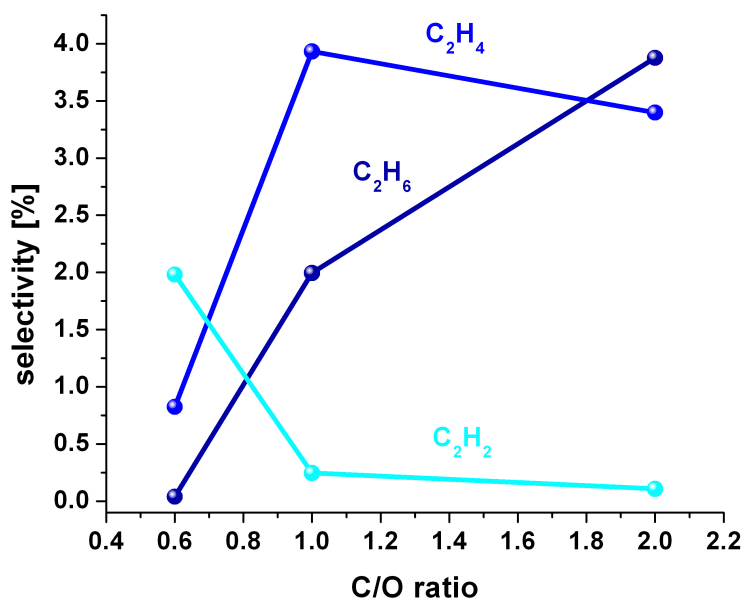


Figure 4.41: C₂ selectivities for variable C/O at $500 \text{ ml} \cdot \text{min}^{-1}$ inlet flow rate.

and $1000 \text{ ml} \cdot \text{min}^{-1}$ inlet flow rate is lower than 0.5 %. As can be seen in Figure 4.40 this changes with increasing C/O ratio, where more ethane and ethylene but no acetylene is formed. Ethane is clearly the dominant C_2 species at $1100 \text{ }^\circ\text{C}$ and $1000 \text{ ml} \cdot \text{min}^{-1}$ flow rate but the overall selectivity remains with 1.8 % very small. Decreasing the flow rate to $500 \text{ ml} \cdot \text{min}^{-1}$ and hence increasing the residence time by a factor of two leads to a selectivity shift towards the dehydrogenated products. At $500 \text{ ml} \cdot \text{min}^{-1}$ and at $C/O = 0.6$, acetylene is the exclusive C_2 species indicating ignited gas phase reactions. At higher C/O ratios acetylene is no longer formed. The main C_2 product at $C/O = 1.0$ is ethylene (4 % selectivity) and at $C/O = 2.0$ ethane (3.5 % selectivity) respectively.

4.5.3 Gas phase Ignition and Ignition Delay

The ignition of a homogeneous reaction requires the development of a stable radical pool, which is known in combustion as ignition delay. The following section will discuss the flammability of different used mixtures and the effect of temperature and flow velocity on the ignition delay time. As a quantitative analysis of these effects requires a known gas composition and a fixed temperature, the calculations shown below can only be interpreted qualitatively. Surface reactions change the composition in flow direction in the Pt tube and also the gas temperature is a function of the position. Nevertheless, the concept of ignition delay times can explain why gas phase ignition is only observed for $C/O = 0.6$ and not for other C/O ratios. For $C/O = 0.6$ it also explains the observed flow rate and temperature dependence.

Flammable Limits of Methane / Oxygen Mixtures and the Ignition Delay

The lowest temperature observed for homogeneous (non-catalyzed) ignition of methane in air is about $580 \text{ }^\circ\text{C}$ at atmospheric pressure [142]. The flammable limit of a methane-oxygen-nitrogen mixture is illustrated in Figure 4.42 [143]. The circles represent the three used C/O ratios of 0.6, 1.0 and 2.0, the red line shows the inert gas fraction of about 10 % Ar .

As can be seen, the O_2 concentration at a C/O ratio of 0.6 is high enough for the mixture to ignite. At higher C/O values the mixture can not ignite as it is too fuel

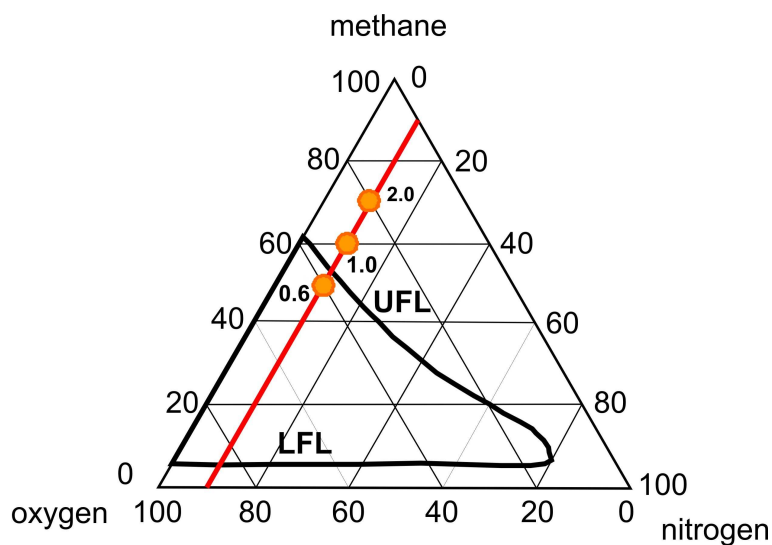


Figure 4.42: Flammable limits of methane in oxygen with nitrogen as diluent, adopted from [143]. Circles represent the three used C/O ratios.

rich. Unfortunately this diagram is only valid for a gas temperature of 25 °C. Higher gas temperatures shift the UFL (Upper Flammable Limit) to higher methane values, resulting in broadened flammable region.

The flammable limit for methane in air is about 5 to 16 %. Vanderstraeten et al. showed, that for a pressure of 1 bar the UFL increases from 15.7 Vol% to 18.1 Vol% methane in air while increasing the temperature from 25 °C to 200 °C [23]. He also used Eq. 4.47 for the pressure dependency and Eq. 4.48 for the temperature dependency for the calculation of the upper flammable limit:

$$UFL(p_1) = UFL(p_0) \cdot \left[1 + a \cdot \left(\frac{p_1}{p_0} - 1 \right) + b \cdot \left(\frac{p_1}{p_0} - 1 \right)^2 \right] \quad (4.47)$$

with $a = 0.0466$ and $b = -0.000269$ for $T = 20$ °C

$$UFL(T_1) = UFL(T_0) \cdot \left[1 + c \cdot \left(\frac{T_1 - T_0}{100} \right) \right] \quad (4.48)$$

with $c = 0.0854$ K⁻¹

According to 4.48 and using the ULF for a methane/oxygen mixture at 1000 °C only a small amount of oxygen is necessary for gas phase ignition.

Therefore it is in general possible, that the analyzed mixtures can ignite under the used conditions.

The lower flammable limit may also be lowered by the interplay with a noncatalytic surface due to heat exchange, but is irrelevant under operation conditions, as the fuel is always used in excess.

Nevertheless it was observed by several scientists that a flammable mixture does not ignite instantaneously after supply of energy, but after a distinct time - the ignition delay [144] [145]. Lamoureux et al. fits data of several groups and results in the following expression for the calculation of the ignition delay, depending of methane and oxygen mole fraction, pressure and temperature - Eq. 4.49 [146]:

$$\tau(s) = (X_{CH_4})^{0.3} (X_{O_2})^{-1} p^{-0.7} \left[7.8 \cdot 10^6 \exp\left(\frac{-25000}{T}\right) + 7.8 \cdot \exp\left(\frac{-10000}{T}\right) \right]^{-1} \quad (4.49)$$

A typical ignition delay for the non-catalyzed gas phase reaction for CPO conditions is in the range of a few ms. The ignition delay for a surface reaction over platinum instead is only about a few μs [147].

The Gas Phase Ignition with C/O of 0.6 with different Flow Velocities

The ignition of a gas phase reaction is dependent of the gas mixture and the flow rate. During this work three different flow velocities were studied using a C/O ratio of 0.6. As a result the gas phase ignition temperatures were found to be 1100 °C for 500 ml · min⁻¹, 1150 °C for 1000 ml · min⁻¹ and 1180 °C for 1300 ml · min⁻¹. Using now Eqn. 4.49 from section 4.5.3 allows calculating the ignition delay for a set of methane and oxygen ratios and temperature. Higher gas flows result in lower residence times, respectively in lower reaction times in the tube.

Again the calculated data will only show trends as neither the gas composition (oxygen is consumed at the wall and products, e.g. hydrogen, diffuse into the middle gas stream), nor a defined temperature level is reached. A comparison of the flow times through the tube and the ignition delays are presented in Fig. 4.43.

With increasing temperature the ignition delay for a C/O = 0.6 mixture decreases strongly from about 6 ms at 1100 °C to about 2.2 ms at 1180 °C. The residence times of the gases increase linearly with the flow through the tube. The intersection between the residence time curve and one ignition delay curve is equal to gas phase ignition at this point.

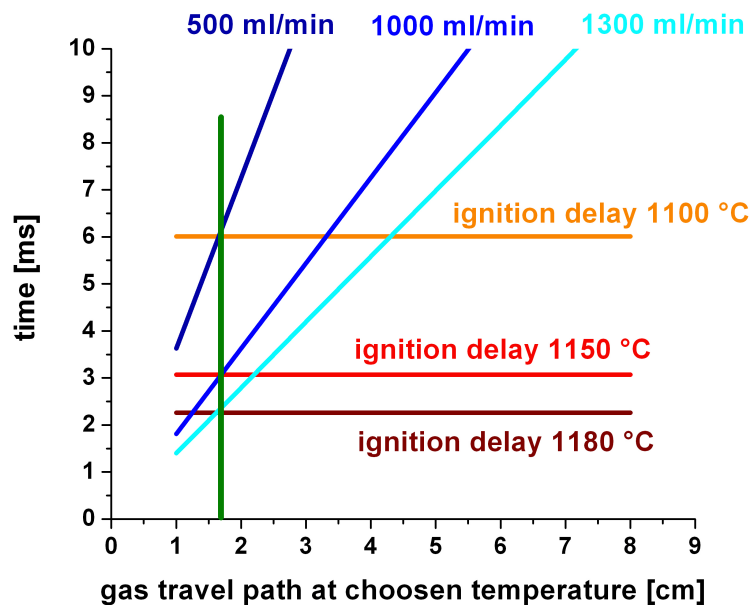


Figure 4.43: Ignition delay times for different temperatures with a C/O of 0.6 - resident times for three flows velocities.

With a flow of $1300 \text{ ml} \cdot \text{min}^{-1}$ the mixture would ignite at a temperature of $1180 \text{ }^\circ\text{C}$ after being virtually 1.7 cm at this temperature level. This distance is not equal to a position in the tube, as it represents a travel length at a fixed temperature. The tube offers a temperature curve instead.

The gas phase ignition starts always from the outlet, shown by Fig. 4.44, which displays the temperature curves of all three flows direct after the ignition of the gas phase.

Assuming now an equal conversion of oxygen and methane for the mixtures before gas phase ignition and equal temperature profiles (which is not too incorrect, as before ignition methane conversion is small and oxygen conversion always between 75 % to 85 % and the temperature profiles look similar - compare e.g. Fig. 4.38) the intercept between the delay times for the found gas phase ignition temperatures and the residence times should always be at the same travel length. This behavior was found and is represented by the green line in Fig. 4.43 and Fig. 4.45.

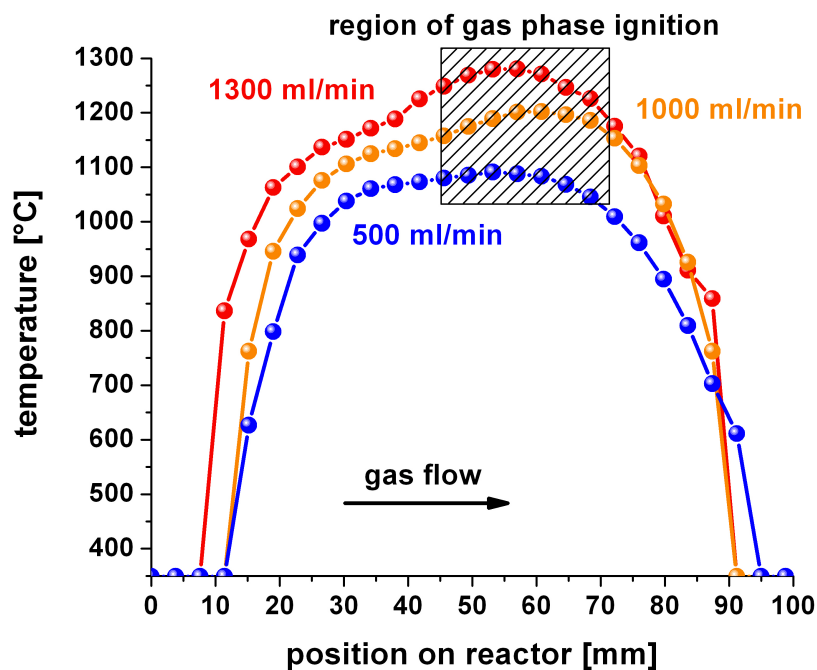


Figure 4.44: Temperature profiles of three flow velocities with a C/O of 0.6 direct after gas phase ignition.

The Gas Phase Ignition with varying C/O Ratios and a Flow Rate of $500 \text{ ml} \cdot \text{min}^{-1}$

The same effect should hold not only for different flow velocities at a fixed C/O ratio, but also for a fixed flow and varying C/O ratios. Fig. 4.45 shows the ignition delays for a flow of $500 \text{ ml} \cdot \text{min}^{-1}$ with varying C/O ratios.

With increasing C/O ratio the ignition delay time is shifted strongly to higher values. Both mixtures with 1.0 and 2.0 respectively should not be gas phase ignited, which was exactly shown by the experiments, as the oxygen conversion not reaches totality.

Contrary to the homogeneous reaction the ignition times for heterogeneous surface reactions are three orders of magnitudes lower [147] and therefore not influenced by a changed gas flow velocity or C/O ratio.

This difference in ignition delay times for a surface and a gas phase reaction is the best evidence, that the observed methyl radicals are exclusively produced in

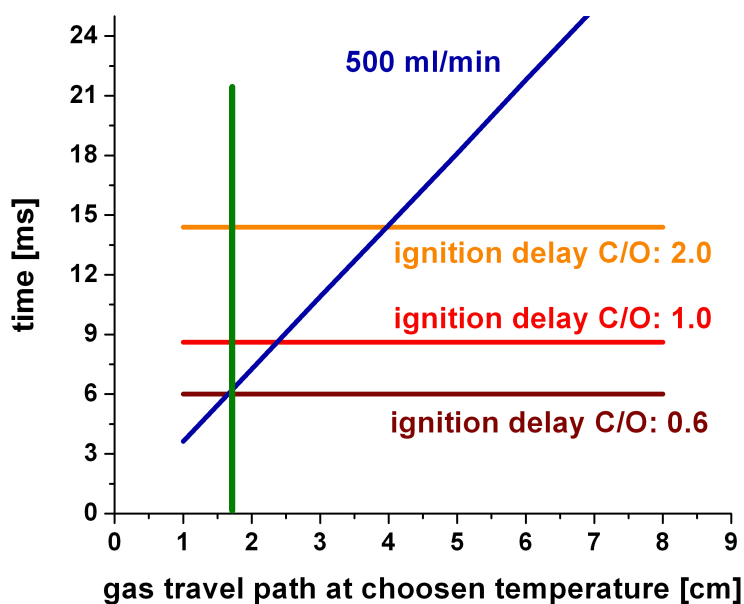


Figure 4.45: Ignition delays for different C/O ratios with a flow of $500 \text{ ml} \cdot \text{min}^{-1}$.

homogeneous reactions and not by a desorption from the catalyst surface. Applying the same temperatures and C/O ratios should lead with nearly every flow rate to a desorption (or contrariwise not to a desorption) of radicals as the surface reactions run nearly instantaneously. A change in the reaction mechanism is not explainable by surface reactions but was observed with a C/O of 0.6 and a temperature change from surface ignition to above $1100 \text{ }^\circ\text{C}$. The gas stream with $500 \text{ ml} \cdot \text{min}^{-1}$ shows all signs of homogeneous reactions, but the mixture with $1000 \text{ ml} \cdot \text{min}^{-1}$ not.

Part V

Summary

Chapter 5

Summary

Goal of the present work was to investigate whether gas phase reactions play a role in high temperature methane oxidation on platinum. The experimental strategy was to conduct the reaction in a dedicated *Pt* catalytic wall reactor at different reactant stoichiometries, volumetric inlet flow rates and reactor temperatures and to screen the reacting gases for short lived intermediates like radicals using the technique of molecular beam mass spectrometry with threshold ionization. The experiments were complemented by GC analysis of the reactor effluent gases and pyrometric temperature measurements of the reactor temperature profile.

After outlining in Section 4.1.3 and 4.1.4 how radicals can be detected and quantified by molecular beam mass spectrometry and threshold ionization, the detection limit for radicals and non-radical trace species was determined to be in the low *ppm* range (Section 4.1.5). From catalytic ignition studies (Section 4.3.1), steady state experiments at temperatures up to 1310 °C and a reactant stoichiometry slightly above the upper flammability limit ($C/O = 0.6$) (Section 4.4) as well as from catalytic experiments at other C/O ratios and at varying flow rates (Section 4.5) the following mechanistic picture of the interplay between surface and gas phase reactions during methane oxidation on *Pt* could be constructed:

At temperatures of about 450 °C, methane oxidation reactions started at the *Pt* surface forming nearly exclusively CO_2 and H_2O and large amounts of heat due to the high methane combustion enthalpy of about $-800 \text{ kJ} \cdot \text{mol}^{-1}$. At 580 °C, this rapid heat release exceeded heat losses in the employed reactor configuration

and reactor light-off was observed. After light-off, the reactor could be operated autothermally. The highest autothermal operation temperature was $1015\text{ }^\circ\text{C}$, observed at the lowest investigated C/O ratio of 0.6. Neither C_2 coupling products nor any radicals desorbing from the Pt surface could be detected between ignition of surface oxidation reactions and autothermal reactor operation. In terms of stable products, the total oxidation products CO_2 and H_2O dominated clearly before reactor light-off, but the selectivity to CO and H_2 increased with increasing temperature in line with the thermodynamic trend. At $1015\text{ }^\circ\text{C}$, the autothermal operation temperature at $C/O = 0.6$, CO and H_2 were formed with 67 % and 12 % selectivity respectively. Characteristic for the employed Pt catalytic wall reactor was that O_2 breakthrough occurred for all investigated C/O ratios at inlet flow rates of $500\text{ ml}\cdot\text{min}^{-1}$ and more. This incomplete O_2 conversion turned out to be vital for the ignition of gas phase oxidation reactions (cf. Section 4.4). As demonstrated numerically in Section 4.2, the O_2 breakthrough could be ascribed to the slower rate of O_2 diffusion to the Pt wall compared to its axial convection through the tube.

If the reactor temperature was increased above the autothermal temperature by electrical heating, an ignition of gas phase oxidation reactions and complete O_2 conversion was observed at around $1150\text{ }^\circ\text{C}$ for $C/O = 0.6$ but not for the other investigated C/O ratios of 1.0 and 2.0. The interpretation of this second ignition point in terms of gas phase reactions was supported by the following observations:

- jump up in O_2 and CH_4 conversion (cf. Fig. 4.24)
- occurrence of flames in the tube center (cf. Fig. 4.37)
- development of a pronounced temperature maximum upon ignition at $1150\text{ }^\circ\text{C}$ (cf. Fig. 4.28)
- onset of additional CO_x production (cf. Fig. 4.27)
- detection of $CH_3\cdot$ radicals at 15 amu by threshold ionization (cf. Fig. 4.29)
- formation of C_2 coupling products (C_2H_6 , C_2H_4 , C_2H_2) (cf. Fig. 4.30) and higher unsaturated C_3 and C_4 coupling products (cf. Fig. 4.35 and 4.36)
- correlation between concentration of $CH_3\cdot$ radicals in the gas phase and formation of C_2 coupling products (cf. Fig. 4.30)

As discussed in Section 4.5.3, the exceptional behavior of the stoichiometry $C/O = 0.6$ was rationalized by taking into account that this stoichiometry was already close to the upper flammability limit of CH_4/O_2 mixtures. As the latter increases with temperature and as other combustible fuels like H_2 and CO were formed by surface reactions, confined combustion reactions could occur at $C/O = 0.6$ in the tube without being able to propagate with the flow direction (lack of O_2) or against the flow direction (feed mixture outside flammability limit and ignition delay for homogeneous reactions). The occurrence of C_2H_6 , C_2H_4 , C_2H_2 and traces of higher unsaturated C_3 and C_4 coupling products suggests the occurrence of pyrolysis like reactions probably in O_2 deficient regions like close to the tube wall or towards the tube outlet (cf. Fig. 4.26). The flow dependence of the ignition temperature at $C/O = 0.6$ was qualitatively explained by the interplay between ignition delay time and convective transport time through the tube (Section 4.5.3).

Concerning gas phase radical chemistry, $CH_3\cdot$ radicals were the only radical species that could be detected by threshold ionization. As $CH_3\cdot$ radicals are known to be chain carriers in gas phase methane oxidation network as well as in pyrolysis and as they always occurred upon ignition of gas phase oxidation reactions it was concluded that they were exclusively produced in the gas phase and not at the Pt surface in contrast to the mechanism assumed for methane oxidative coupling on strong basic oxides like Li/MgO . The steady state concentration of other gas phase radicals like $OH\cdot$, $HO_2\cdot$ must have been below the detection limit of the threshold ionization technique, a solid assumption facing calculated concentration values in the literature [42].

The main results of this thesis can be summarized in the simplified mechanistic picture shown in Figure 5.1. The interaction between surface and gas chemistry during high temperature methane oxidation on Pt comprises mainly the provision of heat from exothermic surface oxidation reactions to drive the gas phase chemistry, in particular endothermic pyrolysis reactions. It could be shown that ethane, ethylene and acetylene are consecutive products formed upon recombination and dehydration of $CH_3\cdot$ radicals in the gas phase. No evidence was found for the catalytic generation of gas phase radicals, it is rather more likely that the catalyst acts as a sink for radicals (destructive wall collisions). Even though the gas phase $CH_3\cdot$ radicals were not produced at the catalyst, this work demonstrates for the first time that gas phase

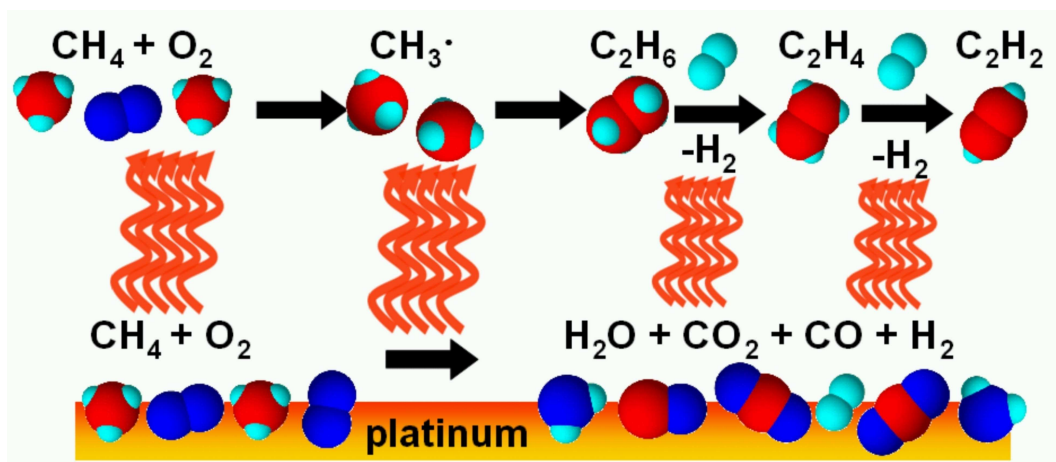


Figure 5.1: Interaction of surface and gas phase chemistry in the high temperature catalytic methane oxidation on platinum.

radicals can be detected and quantified over a solid catalyst under high pressure and high temperature reaction conditions.

Bibliography

- [1] Ertl G.; Knözinger H.; Weitkamp J.; Eds. *Handbook of Heterogeneous Catalysis*, volume 4, chapter 2 - Inorganic Reactions. Wiley-VCH, Weinheim, 1997.
- [2] Dahl S.; Sehested J.; Jacobsen C. J. H.; Törnqvist E.; Chorkendorff I. Surface Science Based Microkinetic Analysis of Ammonia Synthesis over Ruthenium Catalysts. *J. Catal.* **2000**, *192*, 391-399.
- [3] Wess G.; Urmann M.; Sickenberger B. Medicinal Chemistry: Challenges and Opportunities. *Angew. Chem. Int. Ed.* **2001**, *40*, 3341-3350.
- [4] Breitung C.; Papp H.; Li X.; Olindo R.; Lercher J. A.; Lloyd R.; Wrabetz S.; Jentoft F. C.; Meinel K.; Förster S.; Schindler K.-M.; Neddermeyer H.; Widdra W.; Hofmann A.; Sauer J. Activation and Isomerization of n-Butane on Sulfated Zirconia Model Systems: An Integrated Study across the Materials and Pressure Gaps. *Phys. Chem. Chem. Phys.* **2007**, *9*, 3600-3618.
- [5] Böttger I.; Schedel-Niedrig T.; Timpe O.; Gottschall R.; Hävecker M.; Ressler T.; Schlögl R. Catalytic Methanol Oxidation over Copper: Observation of Reaction-Induced Nanoscale Restructuring by Means of In Situ Time-Resolved X-ray Absorption Spectroscopy. *Chem. Eur. J.* **2000**, *6* (10), 1870-1876.
- [6] Kerr J. A. Bond Dissociation Energies by Kinetic Methods. *Chem. Rev.* **1966**, *66* (5), 465-500.
- [7] Olsvik O.; Rokstad O. A.; Holmen A. Pyrolysis of Methane in the Presence of Hydrogen. *Chem. Eng. Technol.* **1995**, *18*, 349-358.

- [8] Horn R.; Degenstein N.; Williams K. A.; Schmidt L. D. Spatial and Temporal Profiles in Millisecond Partial Oxidation Processes. *Catal. Lett.* **2006**, *110* (3-4), 169-178.
- [9] Lie L. N.; Razouk R. R.; Deal B. E. High Pressure Oxidation of Silicon in Dry Oxygen. *J. Electrochem. Soc.* **1982**, *129* (12), 2828-2834.
- [10] Hickman D. A.; Schmidt L. D. Production of Syngas by Direct Catalytic Oxidation of Methane. *Science* **1993**, *259* (5093), 343-346.
- [11] Deutschmann O.; Behrendt F.; Warnatz J. Formal Treatment of Catalytic Combustion and Catalytic Conversion of Methane. *Catal. Today* **1998**, *46*, 155-163.
- [12] Deutschmann O.; Schmidt L. D. Modeling the Partial Oxidation of Methane in a Short-Contact-Time Reactor. *AiCHE J.* **1998**, *44* (11), 2465-2477.
- [13] Baerns M.; Behr A.; Brehm A.; Gmehling J.; Hofmann H.; Onken U.; Renken A. *Technische Chemie*, chapter 11.2 - Katalyse, page 408. Wiley-VCH, Weinheim, 2006.
- [14] Baerns M.; Behr A.; Brehm A.; Gmehling J.; Hofmann H.; Onken U.; Renken A. *Technische Chemie*, chapter 11.2 - Katalyse, page 409. Wiley-VCH, Weinheim, 2006.
- [15] Atkins P. W. *Physikalische Chemie*, chapter Tabellenanhang, page 1033. VCH, Weinheim, 2. edition, 1996.
- [16] Endter F. Die Technische Synthese von Cyanwasserstoff aus Methane und Ammoniak ohne Zusatz von Sauerstoff. *Chem. Ing. Tech.* **1958**, *30* (5), 305-310.
- [17] Andrussow L. Über die Katalytische Oxydation von Ammoniak-Methan-Gemischen zu Blausäure. *Angew. Chem.* **1935**, *48* (37), 593-595.
- [18] Akers W. W.; Camp D. P. Kinetics of the Methane-Steam Reaction. *AiCHE J.* **1955**, *1* (4), 471-475.
- [19] Witt P. M.; Schmidt L. D. Effect of Flow Rate on the Partial Oxidation of Methane and Ethane. *J. Catal* **1996**, *163*, 465-475.

- [20] Lunsford J. H. The Catalytic Oxidative Coupling of Methane. *Angew. Chem. Int. Ed. Engl.* **1995**, *34*, 970-980.
- [21] Tabata K.; Teng Y.; Takemoto T.; Suzuki E.; Banares M. A.; Pena M. A.; Fierro J. L. G. Activation of Methane by Oxygen and Nitrogen Oxide. *Catal. Rev.* **2002**, *44* (1), 1-58.
- [22] Li S. C.; Williams F. A. NO_x Formation in Two-Stage Methane-Air Flames. *Combust. Flame* **1999**, *118*, 399-414.
- [23] Vanderstraeten B.; Tuerlinckx D.; Berghmans J.; Vliegen S.; Van't Oost E.; Smit B. Experimental Study of the Pressure and Temperature Dependence on the Upper Flammability Limit of Methane/Air Mixtures. *J. Hazard. Mater.* **1997**, *56*, 237-246.
- [24] Hayes R. E.; Kolaczkowski S. T. *Introduction to Catalytic Combustion*, chapter 1 - Introduction, page 2. Gordon and Breach Science Publishers, Amsterdam, 1997.
- [25] Lyubovsky M.; Smith L. L.; Castaldi M.; Karim H.; Nentwick B.; Etemad S.; LaPierre R.; Pfefferle W. C. Catalytic Combustion over Platinum Group Catalysts: Fuel-Lean versus Fuel-Rich Operation. *Catal. Today* **1995**, *83* (1-4), 71-84.
- [26] Lee J. H.; Trimm D. L. Catalytic Combustion of Methane. *Fuel Process. Technol.* **1995**, *42*, 339-359.
- [27] Markatou P.; Pfefferle L. D.; Smooke M. D. A Computational Study of Methane-Air Combustion over Heated Catalytic and Non-Catalytic Surfaces. *Combust. Flame* **1993**, *93* (1-2), 185-201.
- [28] Griffin T. A.; Pfefferle L. D.; Dyer M. J.; Crosley D. R. The Ignition of Methane/Ethane Boundary Layer Flows by Heated Catalytic Surfaces. *Combust. Sci. Technol.* **1989**, *65*, 19-37.
- [29] Pfefferle L. D.; Griffin T. A.; Winter M.; Crosley D. R.; Dyer M. J. The Influence of Catalytic Activity on the Ignition of Boundary Layer Flows, Part I: Hydroxyl Radical Measurements. *Combust. Flame* **1989**, *76*, 325-338.

- [30] Mallens E. P. J.; Hoebink J. H. B. J.; Marin G. B. The Reaction Mechanism of the Partial Oxidation of Methane to Synthesis Gas: A Transient Kinetic Study over Rhodium and a Comparison with Platinum. *J. Catal.* **1997**, *167*, 43-56.
- [31] Grunwaldt J.-D.; Baiker A. Axial Variation of the Oxidation state of *Pt – Rh/Al₂O₃* during Partial Methane Oxidation in a Fixed-Bed Reactor: An *in situ* X-ray Absorption Spectroscopy Study. *Catal. Lett.* **2005**, *99* (1-2), 5-12.
- [32] Mattos L. V.; de Oliveira E. R.; Resende P. D.; Noronha F. B.; Passos F. B. Partial Oxidation of Methane on *Pt/CeZrO₂* Catalysts. *Catal. Today* **2002**, *77*, 245-256.
- [33] Mark M. F.; Maier W. F. *CO₂*-Reforming of Methane on Supported *Rh* and *Ir* Catalysts. *J. Catal.* **1996**, *164* (1), 122-130.
- [34] Horn R.; Williams K. A.; Degenstein N. J.; Bitsch-Larsen A.; Dalle Nogare D.; Tupy S. A.; Schmidt L. D. Methane Catalytic Partial Oxidation on Autothermal Rh and Pt Foam Catalysts: Oxidation and Reforming Zones, Transport Effects, and Approach to Thermodynamic Equilibrium. *J. Catal.* **2007**, *249*, 380-393.
- [35] Lee J. S.; Oyama S. T. Oxidative Coupling of Methane to Higher Hydrocarbons. *Catal. Rev.-Sci. Eng.* **1988**, *30* (2), 249-280.
- [36] Campbell K. D.; Lunsford J. H. Contribution of Gas-Phase Radical Coupling in the Catalytic Oxidation of Methane. *J. Phys. Chem.* **1988**, *92* (20), 5792-5796.
- [37] Ito T.; Wang J.-X.; Lin C.-H.; Lunsford J. H. Oxidative Dimerization of Methane over a Lithium-promoted Magnesium Oxide Catalyst. *J. Am. Chem. Soc.* **1985**, *107*, 5062-5068.
- [38] Feng Y.; Niiranen J.; Gutman D. Kinetic Studies of the Catalytic Oxidation of Methane. 1. Methyl Radical Production on 1 % *Sr/La₂O₃*. *J. Phys. Chem* **1991**, *95*, 6558-6563.
- [39] Feng Y.; Niiranen J.; Gutman D. Kinetic Studies of the Catalytic Oxidation of Methane. 2. Methyl Radical Recombination and Ethane Formation over 1 % *Sr/La₂O₃*. *J. Phys. Chem* **1991**, *95*, 6564-6568.

- [40] Hofstad K. H.; Sperle T.; Rokstad O. A.; Holmen A. Partial Oxidation of Methane to Synthesis Gas over a Pt/10 % Rh gauze. *Catal. Lett.* **1997**, *45* (1-2), 97-105.
- [41] Berlowitz P.; Driscoll D. J.; Lunsford J. H.; Butt J. B.; Kung H. H. Does Platinum Generate Gas Phase Methyl Radicals in the Catalytic Combustion of Methane? *Combust. Sci. Technol.* **1984**, *40* (5-6), 317-321.
- [42] Quiceno R.; Perez-Ramirez J.; Warnatz J.; Deutschmann O. Modeling the High-Temperature Catalytic Partial Oxidation of Methane over Platinum Gauze: Detailed Gas-Phase and Surface Chemistries coupled with 3D Flow Field Simulations. *Appl. Catal. A* **2006**, *303* (2), 166-176.
- [43] Quiceno R.; Deutschmann O.; Warnatz J.; Perez-Ramirez J. Rational Modeling of the CPO of Methane over Platinum Gauze: Elementary Gas-Phase and Surface Mechanisms coupled with Flow Simulations. *Catal. Today* **2007**, *119* (1-4), 311-316.
- [44] Wedler G. *Lehrbuch der Physikalischen Chemie*, chapter 6.4 - Reaktionsmechanismen, page 763. VCH Verlagsgesellschaft, Weinheim, 1987.
- [45] Hidaka Y.; Sato K.; Henmi Y.; Tanaka H.; Inami K. Shock-Tube and Modeling Study of Methane Pyrolysis and Oxidation. *Combust. Flame* **1999**, *118*, 340-358.
- [46] Dean A. M. Detailed Kinetic Modeling of Autocatalysis in Methane Pyrolysis. *J. Phys. Chem.* **1990**, *94*, 1432-1439.
- [47] Fincke J. R.; Anderson R. P.; Hyde T.; Wright R.; Bewley R.; Haggard D. C.; Swank W. D. Thermal Conversion of Methane to Acetylene: Final Report. Technical Report INEEL/EXT-99-01378, Idaho National Engineering and Environmental Laboratory, 2000.
- [48] Holmen A.; Olsvik O.; Rokstad O. A. Pyrolysis of Natural Gas: Chemistry and Process Concepts. *Fuel Process. Technol.* **1995**, *42*, 249-267.
- [49] Gladisch H. How Huels makes Acetylene by DC Arc. *Hydrocarbon Process. Petrol. Refiner.* **1962**, *41*, 159-164.

- [50] Anon. New Burner opens Door to Arc Acetylene. *Chem. Week* **1964**, *94* (3), 64-65.
- [51] Kee R. J.; Coltrin M. E.; Glarborg P. *Chemically Reacting Flow - Theory and Practice*, chapter 13 - Reaction Mechanisms, pages 560–562. Wiley, Hoboken - New Jersey, 2003.
- [52] Lewis B.; von Elbe G. *Combustion, Flames and Explosions*, chapter IV - The Reaction between Hydrocarbons and Oxygen, pages 94–116. Academic Press Inc., New York, 1951.
- [53] Mackie J. C. Partial Oxidation of Methane: The Role of the Gas Phase Reactions. *Catal. Rev.* **1991**, *33* (1-2), 169-240.
- [54] Huff M. C.; Androulakis I. P.; Sinfelt J. H.; Reyes S. C. The Contribution of Gas-Phase Reactions in the Pt-Catalyzed Conversion of Ethane-Oxygen Mixtures. *J. Catal.* **2000**, *191*, 46-54.
- [55] Zerkle D. K.; Allendorf M. D.; Wolf M.; Deutschmann O. Understanding Homogeneous and Heterogeneous Contributions to the Platinum-Catalyzed Partial Oxidation of Ethane in a Short-Contact-Time Reactor. *J. Catal.* **2000**, *196*, 18-39.
- [56] Perbal R.; Riesthuis P. Detonation of Degassing line at Gas/Slurry Loop Reactor. *J. Loss. Prev. Process. Ind.* **1997**, *10* (1), 67-73.
- [57] Driscoll D. J.; Martir W.; Wang J.-X.; Lunsford J. H. Formation of Gas-Phase Methyl Radicals over MgO. *J. Am. Chem. Soc.* **1985**, *107*, 58-63.
- [58] Davis M. B.; Pawson M. D.; Veser G.; Schmidt L. D. Methane Oxidation over Noble Metal Gauzes: a LIF Study. *Combust. Flame* **2000**, *123* (1-2), 159-174.
- [59] Marks C. M.; Schmidt L. D. Hydroxyl Radical Desorption in Catalytic Combustion. *Chem. Phys. Lett.* **1991**, *178* (4), 358-362.
- [60] Vlachos D. G. Homogeneous-Heterogeneous Oxidation Reactions over Platinum and Inert Surfaces. *Chem. Eng. Sci.* **1996**, *51* (10), 2429-2438.

- [61] Owston R.; Magi V.; Abraham J. Interactions of Hydrogen Flames with Walls: Influence of Wall Temperature, Pressure, Equivalence Ratio, and Diluents. *Int. J. Hydrogen Energ.* **2007**, *32*, 2094-2104.
- [62] Lewis B.; von Elbe G. *Combustion, Flames and Explosions*, chapter I - Theoretical Foundations, page 6. Academic Press Inc., New York, 1951.
- [63] Lewis B.; von Elbe G. *Combustion, Flames and Explosions*, chapter I - Theoretical Foundations, page 5. Academic Press Inc., New York, 1951.
- [64] Miller D. R. *Atomic and Molecular Beam Methods Vol. 1*, chapter 2 - Free Jet Sources, page 14. Oxford University Press, New York - Oxford, 1988.
- [65] Miller D. R. *Atomic and Molecular Beam Methods Vol. 1*, chapter 2 - Free Jet Sources, page 15. Oxford University Press, New York - Oxford, 1988.
- [66] Horn R.; Ihmann K.; Ihmann J.; Jentoft F. C.; Geske M.; Taha A.; Pelzer K.; Schlögl R. Molecular Beam Mass Spectrometer equipped with a Catalytic Wall Reactor for In Situ Studies in High Temperature Catalysis Research. *Rev. Sci. Instrum.* **2006**, *77*, 9-17.
- [67] Miller D. R. *Atomic and Molecular Beam Methods Vol. 1*, chapter 2 - Free Jet Sources, page 18. Oxford University Press, New York - Oxford, 1988.
- [68] Miller D. R. *Atomic and Molecular Beam Methods Vol. 1*, chapter 2 - Free Jet Sources, page 23. Oxford University Press, New York - Oxford, 1988.
- [69] Fenn J. B. Mass Spectrometric Implications of High-Pressure Ion Sources. *Int. J. Mass Spectrom.* **2000**, *200*, 459-478.
- [70] Becker E. W.; Henkes W. Geschwindigkeitsanalyse von LAVAL-Strahlen. *Z. Phys.* **1956**, *146*, 320-332.
- [71] Becker E. W.; Bier K.; Burghoff H. Die Trenndüse. Ein neues Element zur Gas- und Isotopentrennung. *Z. Naturforsch.* **1955**, *10a*, 565-572.
- [72] Greene F. T.; Brewer J.; Milne T. A. Mass Spectrometric Studies of Reactions in Flames. I. Beam Formation and Mass Dependence in Sampling 1-Atm Gases. *J. Chem. Phys.* **1964**, *40* (6), 1488-1495.

- [73] Waterman P. C.; Stern S. A. Separation of Gas Mixtures in a Supersonic Jet. *J. Chem. Phys.* **1959**, *31* (2), 405-419.
- [74] Reis V. H.; Fenn J. B. Separation of Gas Mixtures in Supersonic Jets. *J. Chem. Phys.* **1963**, *39* (12), 3240-3250.
- [75] Campargue R. Aerodynamic Separation Effect on Gas and Isotope Mixtures Induced by Invasion of the Free Jet Shock Wave Structure. *J. Chem. Phys.* **1970**, *52* (4), 1795-1802.
- [76] Campbell C. T.; Ertl G.; Kuipers H.; Segner J. A Molecular Beam Study of the Adsorption and Desorption of Oxygen from a Pt/(111) Surface. *Surf. Sci.* **1981**, *107*, 220-236.
- [77] Valden M.; Aaltonen J.; Kuusisto E.; Pessa M.; Barnes C. J. Molecular Beam Studies of CO Oxidation and CO-NO Reactions on a supported Pd Catalyst. *Surf. Sci.* **1994**, *307-309*, 193-198.
- [78] Kaiser R. I.; Le T. N.; Nguyen T. L.; Mebel A. M.; Balucani N.; Lee Y. T.; Stahl F.; v. R. Schleyer P.; Schaefer III H. F. A combined Crossed Molecular Beam and Ab Initio Investigation of C_2 and C_3 Elementary Reactions with Unsaturated Hydrocarbons—Pathways to Hydrogen deficient Hydrocarbon Radicals in Combustion Flames. *Faraday Discuss.* **2001**, *119*, 51-66.
- [79] Vandooren J.; Branch M. C.; Van Tiggelen P. J. Comparisons of the Structure of Stoichiometric CH_4-N_2O-Ar and CH_4-O_2-Ar Flames by Molecular Beam Sampling and Mass Spectrometric Analysis. *Combust. Flame* **1992**, *90* (3-4), 247-258.
- [80] Petherbridge J. R.; May P. W.; Pearce S. R. J.; Rosser K. N.; Ashfold M. N. R. Low Temperature Diamond Growth using CO_2/CH_4 Plasmas: Molecular Beam Mass Spectrometry and Computer Simulation Investigations. *J. Appl. Phys.* **2001**, *89* (2), 1484-1492.
- [81] Geske M.; Pelzer K.; Horn R.; Jentoft F. C.; Schlögl R. In-Situ Investigation of Gas Phase Radical Chemistry in the Catalytic Partial Oxidation of Methane on Pt. *Catal. Today* **2009**, *142*, 61-69.

- [82] Sablier M.; Fujii T. Mass Spectrometry of Free Radicals. *Chem. Rev.* **2002**, *1029*, 2855-2924.
- [83] NIST National Institute of Standards and Technology. <http://webbook.nist.gov/cgi/cbook.cgi?ID=C106978&Units=SI&Mask=200#Mass-Spec>, 16.01 2009.
- [84] Hwang W.; Kim Y.-K.; Rudd M. E. New Model for Electron-Impact Ionization Cross Sections of Molecules. *J. Chem. Phys.* **1996**, *104* (8), 2956-2966.
- [85] Cattolica R. J.; Yoon S.; Knuth E. L. OH Concentration in an Atmospheric-Pressure Methane-Air Flame from Molecular-Beam Mass Spectrometry and Laser-Absorption Spectroscopy. *Combust. Sci. Technol.* **1982**, *28* (5-6), 225-239.
- [86] Douglas D. J.; French J. B. Gas Dynamic of the Inductively Coupled Plasma Mass Spectrometry Interface. *J. Anal. Atom. Spectrom.* **1988**, *3*, 743-747.
- [87] Leeds S. M.; May P. W.; Bartlett E.; Ashfold M. N. R.; Rosser K. N. Molecular Beam Mass Spectrometry Studies of the Gas-Phase Chemistry occurring during Microwave Plasma assisted Chemical Vapor Deposition of Diamond. *Diam. Relat. Mater.* **1999**, *8*, 1377-1382.
- [88] Schäfer H.; Tebben A. Gleichgewichtsmessungen im System Platin-Sauerstoff: Gasförmiges Platindioxyd. *Z. Anorg. Allgem. Chem.* **1960**, *304*, 317-321.
- [89] Hulett G. A.; Berger H. W. Volatilization of Platinum. *J. Am. Chem. Soc.* **1904**, *26* (11), 1512-1515.
- [90] Weast R. C. *CRC Handbook of Chemistry and Physics*, chapter Section F - Miscellaneous, pages F-171. CRC PRESS Inc, Boca Raton - Florida, 60th edition, 1980.
- [91] Müller B.; Renz U. Development of a fast Fiber-Optic Two-Color Pyrometer for the Temperature Measurement of Surfaces with varying Emissivities. *Rev. Sci. Instrum.* **2001**, *72* (8), 3366-3374.
- [92] Aksyutov L. N. Normal Spectral Emissivity of Gold, Platinum, and Tungsten. *J. Eng. Phys. Thermophys.* **1974**, *27* (2), 913-917.

- [93] Horn R. *Investigation of Heterogeneously Catalyzed Reactions using Molecular Beam Sampling Mass Spectrometry with Threshold Ionization*. PhD thesis, Technical University Berlin, 2003.
- [94] Wutz M. *Handbuch Vakuumtechnik*, chapter 4.5.1 - Reibungsfreie Strömung, page 84. vieweg, Braunschweig - Wiesbaden, 2000.
- [95] Miller D. R. *Atomic and Molecular Beam Methods Vol. 1*, chapter 2 - Free Jet Sources, page 20. Oxford University Press, New York - Oxford, 1988.
- [96] Dun H.; Mattes B.; Stevenson D. The Gas Dynamics of a Conical Nozzle Molecular Beam Sampling System. *Chem. Phys.* **1979**, *38*, 161-172.
- [97] Wetzel R. C.; Baiocchi F. A.; Hayes T. R.; Freund R. S. Absolute Cross Sections for Electron-Impact Ionization of the Rare-Gas Atoms by the Fast-Neutral-Beam Method. *Phys. Rev. A* **1987**, *35* (2), 559-577.
- [98] Honig R. E. Ionization Potentials of Some Hydrocarbon Series. *J. Chem. Phys.* **1948**, *16* (2), 105-112.
- [99] Collin J. E. *Mass Spectrometry*, chapter 9 - The Determination of Ionization and Appearance Potentials, page 186. Academic Press, London and New York, London - New York, 1965.
- [100] Wannier G. H. The Threshold Law for Single Ionization of Atoms or Ions by Electrons. *Phys. Rev.* **1953**, *90* (5), 817-825.
- [101] Geltman S. Theory of Ionization Probability Near Threshold. *Phys. Rev.* **1956**, *102* (1), 171-179.
- [102] Koffel M. B.; Lad R. A. Ionization and Dissociation of Paraffin Hydrocarbons by Electron Bombardment. *J. Chem. Phys.* **1948**, *16* (4), 420-422.
- [103] Vought R. H. Molecular Dissociation by Electron Bombardment: A Study of SiCl_4 . *Phys. Rev.* **1947**, *71*, 93-101.
- [104] Morrison J. D. On the Optimum Use of Ionization-Efficiency Data. *J. Chem. Phys.* **1963**, *39* (1), 200-207.

- [105] Singh H.; Coburn J. W.; Gravesa D. B. Appearance Potential Mass Spectrometry: Discrimination of Dissociative Ionization Products. *J. Vac. Sci. Technol. A* **2000**, *18* (2), 299-305.
- [106] Lossing F.P.; Semeluk G.P. Free Radicals by Mass Spectrometry. XLII. Ionization Potentials and Ionic Heats of Formation for C1-C4 Alkyl Radicals. *Can. J. Chem.* **1970**, *48* (6), 955-965.
- [107] Plessis P.; Marmet P.; Dutil R. Ionization and Appearance Potentials of CH_4 by Electron Impact. *J. Phys. B* **1983**, *16* (7), 1283-1295.
- [108] Hille E.; Märk T. D. Cross Section for Single and Double Ionization of Carbon Monoxide by Electron Impact from Threshold up to 180 eV. *J. Chem. Phys.* **1978**, *69* (10), 4600-4605.
- [109] Armentrout P. B.; Tarr S. M.; Dori A.; Freund R. S. Electron Impact Ionization Cross Section of Metastable N_2 (Σ^+). *J. Chem. Phys.* **1981**, *75* (6), 2786-2794.
- [110] Rapp D.; Englander-Golden P. Total Cross Sections for Ionization and Attachment in Gases by Electron Impact. I. Positive Ionization. *J. Chem. Phys.* **1965**, *43* (5), 1464-1479.
- [111] Baiocchi F. A.; Wetzel R. C.; Freund R. S. Electron-Impact Ionization and Dissociative Ionization of the CD_3 and CD_2 Free Radicals. *Phys. Rev. Lett.* **1984**, *53* (8), 771-774.
- [112] Duric N.; Cadez I.; Kurepa M. Electron Impact Total Ionization Cross-Sections for Methane, Ethane and Propane. *Int. J. Mass Spectrom. Ion Processes* **1991**, *108*, R1-R10.
- [113] Tate J. T.; Smith P. T. The Efficiencies of Ionization and Ionization Potentials of Various Gases Under Electron Impact. *Phys. Rev.* **1932**, *39* (2), 270-277.
- [114] Foner S. N.; Hudson R. L. Ionization Potential of the OH Free Radical by Mass Spectrometry. *J. Chem. Phys.* **1956**, *25* (3), 602-603.
- [115] Chatham H.; Hils D.; Robertson R.; Gallagher A. Total and Partial Electron Collisional Ionization Cross Sections for CH_4 , C_2H_6 , SiH_4 , and Si_2H_6 . *J. Chem. Phys.* **1984**, *81* (4), 1770-1777.

- [116] Smith D. H. High Performance Flame-Ionization Detector System for Gas Chromatography. *Hewlett-Packard J.* **1973**, *24* (7), 2-10.
- [117] Holm T. Aspects of the Mechanism of the Flame Ionization Detector. *J. Chromatogr. A* **2000**, *842*, 221-227.
- [118] NIST National Institute of Standards and Technology. <http://webbook.nist.gov/cgi/cbook.cgi?ID=C115071&Units=SI&Mask=200#> *Mass – Spec*, 16.01 2009.
- [119] Weast R. C. *CRC Handbook of Chemistry and Physics*, chapter Section F - Miscellaneous, pages F-58-61. CRC PRESS Inc, Boca Raton - Florida, 60th edition, 1980.
- [120] Sari A.; Safekordi A.; Farhadpour F. A. Comparison and Validation of Plug and Boundary Layer Flow Models of Monolithic Reactors: Catalytic Partial Oxidation of Methane on Rh Coated Monoliths. *Int. J. Chem. React. Eng.* **2008**, *6*, A73.
- [121] Baerns M.; Behr A.; Brehm A.; Gmehling J.; Hofmann H.; Onken U.; Renken A. *Technische Chemie*, chapter 3.3 - Stoff- und Wärmetransportvorgänge, page 41. Wiley-VCH, Weinheim, 2006.
- [122] Wilke C. R. Diffusional Properties of Multicomponent Gases. *Chem. Eng. Prog.* **1950**, *46*, 95104.
- [123] Aghalayam P.; Park Y. K.; Fernandes N.; Papavassilion V.; Mhadeshwar A. B.; Vlachos D. G. A C1 Mechanism for Methane Oxidation on Platinum. *J. Catal.* **2003**, *213*, 23-38.
- [124] Claridge J. B.; Green M. L. H.; Tsang S. C.; York A. P. E.; Ashcroft A. T.; Battle P. D. A Study of Carbon Deposition on Catalysts during the Partial Oxidation of Methane to Synthesis Gas. *Catal. Lett.* **1993**, *22*, 299-305.
- [125] Atkins P. W. *Physikalische Chemie*, chapter 2.3.1 - Die Standardenthalpie, page 79. VCH, Weinheim, 2. edition, 1996.
- [126] Atkins P. W. *Physikalische Chemie*, chapter Tabellenanhang, page 1038. VCH, Weinheim, 2. edition, 1996.

- [127] Nilsen O.; Kjekshus A.; Fjellvag H. Reconstruction and Loss of Platinum Catalyst during Oxidation of Ammonia. *Appl. Catal. A-Gen.* **2001**, *207*, 43-54.
- [128] Hannevold L.; Nilsen O.; Kjekshus A.; Fjellvag H. Reconstruction of Platinum-Rhodium Catalyst during Oxidation of Ammonia. *Appl. Catal. A-Gen.* **2005**, *284*, 163-176.
- [129] Lyubovsky M. R.; Barelko V. V. Formation of "Metal Wool" Structures and Dynamics of Catalytic Etching of Platinum Surfaces during Ammonia Oxidation. *J. Catal.* **1994**, *149*, 23-35.
- [130] Gueret C.; Daroux M.; Billaud F. Methane Pyrolysis: Thermodynamics. *Chem. Eng. Sci.* **1997**, *52* (5), 815-827.
- [131] Billaud F. G.; Baronnet F. Thermal Coupling of Methane in a Tubular Flow Reactor: Parametric Study. *Ind. Eng. Chem. Res.* **1993**, *32*, 1549-1554.
- [132] Minnesota USA Personal communication with Ken Williams, Minneapolis.
- [133] Mims C. A.; Mauti R.; Dean A. M.; Rose K. D. Radical Chemistry in Methane Oxidative Coupling: Tracing of Ethylene Secondary Reactions with Computer Models and Isotopes. *J. Phys. Chem.* **1994**, *98*, 13357-13372.
- [134] Homann K. H. Carbon Formation in Premixed Flames. *Combust. Flame* **1967**, *11* (4), 265-287.
- [135] NIST National Institute of Standards and Technology. Nist chemistry webbook, <http://webbook.nist.gov/chemistry/>, 25.05 2009.
- [136] GRACE. <http://www.discoverysciences.com/chromdb/chromview.aspx?refno=1869&discipline=gc>, 16.01 2009.
- [137] Lahaye J.; Prado G. Formation of Carbon Particles from a Gas Phase: Nucleation Phenomenon. *Water Air Soil Poll.* **1974**, *3*, 473-481.
- [138] Frenklach M. Reaction Mechanism of Soot Formation in Flames. *Phys. Chem. Chem. Phys.* **2002**, *4*, 2028-2037.

- [139] Logan M. A.; Rucker T. G.; Gentle T. M.; Muetterties E. L.; Somorjai G. A. Conversion of Acetylene to Benzene over Palladium Single-Crystal Surfaces. 2. The Effect of Additives. *J. Phys. Chem.* **1986**, *90*, 2709-2715.
- [140] Westmoreland P. R.; Dean A. M.; Howard J. B.; Longwell J. P. Forming Benzene in Flames by Chemically Activated Isomerization. *Combust. Flame* **1989**, *93* (25), 81628170.
- [141] D'Anna A.; Kent J. H. Aromatic Formation Pathways in Non-Premixed Methane Flames. *Combust. Flame* **2003**, *132*, 715-722.
- [142] iSOC Technology. Material safety data sheet: Methane, <http://www.isocinfo.com/documentroot/13/methane.pdf>, 08 2008.
- [143] Fritz W. *Reinigung von Abgasen*. Vogel Buchverlag, Würzburg, 2nd edition, 1990.
- [144] Skinner G. B.; Ruehrwein R. A. Shock Tube Studies on the Pyrolysis and Oxidation of Methane. *J. Phys. Chem.* **1959**, *563* (10), 1736-1742.
- [145] Spadaccini L. J.; Colket III M. B. Ignition Delay Characteristics of Methane Fuels. *Prog. Energy Combust. Sci.* **1994**, *20* (5), 431-460.
- [146] Lamoureux N.; Paillard C.-E.; Vaslier V. Low Hydrocarbon Mixtures Ignition Delay Times Investigation behind Reflected Shock Waves . *Shock Waves* **2002**, *11* (4), 309-322.
- [147] Vesper G.; Frauhammer J. Modelling Steady State and Ignition during Catalytic Methane Oxidation in a Monolith Reactor. *Chem. Eng. Sci.* **2000**, *55*, 2271-2286.

List of Figures

| | | |
|------|--|----|
| 1.1 | Simplified surface mechanism for syngas formation and total oxidation - adopted from [10]. | 4 |
| 2.1 | Activation barrier for a reaction $X \rightarrow Y$ with and without catalyst. The reaction enthalpy ΔH is equal for both, but the activation energies E_a are reduced for the catalytic reaction. - Adopted from [13]. | 7 |
| 2.2 | Selectivity control by catalysts, adopted from [14]. | 8 |
| 2.3 | General mechanism of catalytic combustion - adopted from [26]. | 11 |
| 2.4 | I Relative C2 yield and methyl formation rate as function of the Na^+ loading - adopted from [36]; II Variation in C2 and $CH_3\cdot$ productivity as a function of the lithium content at 700 °C - adopted from [20]. | 14 |
| 2.5 | Plot of $CH_3\cdot$ and C_2H_6 concentration as function of catalyst contact time - adopted from [39]. | 14 |
| 2.6 | Methane pyrolysis products with solid carbon phase - adopted from [47]. | 18 |
| 2.7 | Methane pyrolysis products excluding solid carbon phase - adopted from [47]. | 18 |
| 2.8 | General structure of a supersonic free jet expansion with MN denoting the mach number - adopted from [65]. | 25 |
| 2.9 | Sketch of the formation process of the molecular beam with a combi- nation of skimmer and collimator cone in a three stage differentially pumped vacuum system. | 25 |
| 2.10 | Mass separation factors α of various compounds diluted in nitrogen. | 29 |

| | | |
|------|--|----|
| 2.11 | Electron impact ionization mass spectrum of butane, showing strong fragmentation (the molpeak at $m/z = 58$ <i>amu</i> has only small intensity) - adopted from [83]. | 31 |
| 2.12 | Total electron ionization cross sections for <i>He</i> , <i>N₂</i> and <i>CH₄</i> as function of the electron energy - the maximum is observed between 50 <i>eV</i> and 150 <i>eV</i> | 32 |
| 2.13 | Possible sources of the signal at $m/z = 15$ <i>amu</i> , either by ionization of the sought <i>CH₃</i> [•] radicals or by fragmentation of other molecules like <i>CH₄</i> and <i>C₂H₆</i> | 32 |
| 2.14 | Threshold ionization measurements of methyl radicals in an excess of methane - additionally the IP of the radical and the AP from methane fragmentation are shown. | 33 |
| 3.1 | Shape and dimensions of the <i>Pt</i> reactor tube. | 36 |
| 3.2 | Picture of high temperature tubular catalytic wall reactor in the main vacuum chamber of the MBMS. | 36 |
| 3.3 | Laser drilled orifice for molecular beam sampling from the high temperature tubular flow reactor (tilted by 15 ° for wall view). | 37 |
| 3.4 | Sketch of the experimental setup to measure gas phase radicals in the catalytic partial oxidation of methane. | 38 |
| 3.5 | Picture of the experimental setup to measure gas phase radicals in the catalytic partial oxidation of methane. | 38 |
| 3.6 | Sketch of the pyrometer setup including a 0.45 ° stepper motor for an effective spatial resolution of 4 <i>mm</i> on the platinum tube. | 41 |
| 3.7 | GC gas flow and switch scheme. | 42 |
| 3.8 | FID signal of the hydrocarbons for the GC separation efficiency demonstration. | 44 |
| 3.9 | TCD signal of main compounds for the GC separation efficiency demonstration. | 44 |

| | | |
|------|--|----|
| 4.1 | Determination of the <i>He</i> volumetric flow rate through the sampling orifice. | 50 |
| 4.2 | Orifice-skimmer shift experiments with $50 \text{ ml} \cdot \text{min}^{-1}$ <i>Ar</i> and $450 \text{ ml} \cdot \text{min}^{-1}$ <i>He</i> at four different temperatures: I. total pressure dependency; II. Axial MS signal of <i>Ar</i> ; III. Axial MS signal of <i>He</i> ; IV. Axial <i>Ar</i> to <i>He</i> ratios. | 52 |
| 4.3 | Temperature dependent MS signal evolution of a mixture of $50 \text{ ml} \cdot \text{min}^{-1}$ <i>Ar</i> , $200 \text{ ml} \cdot \text{min}^{-1}$ <i>He</i> and $1100 \text{ ml} \cdot \text{min}^{-1}$ N_2 : I. visible temperature effect on raw data; II. nearly no enrichment effect on <i>He</i> normalized data. | 54 |
| 4.4 | Rare gas electron ionization curves near the threshold - adopted from [97]. | 54 |
| 4.5 | Electron ionization data of pure <i>Ar</i> near the threshold, obtained with the used Mass Spectrometer in this work. | 55 |
| 4.6 | Electron Ionization MS peak areas of <i>Ar</i> next to the threshold and the resulting 2^{nd} derivative - giving information about peak shape, energy spread and offset of the MS. | 57 |
| 4.7 | Electron ionization cross sections of <i>CO</i> [110] in N_2 [110] and CH_3 [111] in CH_4 [112]; CH_4 was omitted, as it overlaps with <i>CO</i> . The ionization potential difference in CO/N_2 is much smaller than in CH_3/CH_4 | 60 |
| 4.8 | Linear regression of the MS peak area over concentration data with confidence band and statistical analysis <i>CO</i> in N_2 | 62 |
| 4.9 | I : demonstration of the linear fit of threshold ionization MS data about 3 eV behind the threshold with 50 ppm CH_4 in <i>Ar</i> ; II : threshold ionization MS data of five different, low CH_4 concentrations; III : linear fit of the electron ionization cross section data behind the threshold from CH_3 [111], CH_4 [112] and C_2H_2 [113]; IV : calibration of 10 ppm to 75 ppm CH_4 in <i>Ar</i> to demonstrate the stability of the method (the data with and without the blue circles represent two series of measurements) and the very low detection limit ($< 10 \text{ ppm}$). | 64 |
| 4.10 | Sketch of the GC / MS combination for the identification of unknown GC peaks. | 67 |

| | |
|--|----|
| 4.11 Comparison between reference (taken from NIST [118]) and measured propene fragmentation pattern. | 67 |
| 4.12 Comparison of thermocouple and pyrometer readings at the same position during heating of a platinum tube in vacuum. | 70 |
| 4.13 Overlay of 10 pyrometer spectra to demonstrate the stability and reproducibility of the measurement. | 70 |
| 4.14 Temperature ramp of methane CPO ignition study - heating rate $10\text{ K}\cdot\text{min}^{-1}$. Data were smoothed by a 20 point FFT filter. | 78 |
| 4.15 Snapshot of the surface ignition (view through the tube). | 78 |
| 4.16 Reactant distribution during ignition. Moderate conversion before surface ignition visible. The ignition is represented by full oxygen conversion. Data were smoothed by a 5 point FFT filter. | 78 |
| 4.17 Background corrected product distribution during ignition. The CO signal was additionally reduced by the fragmentation of CO_2 on $m/z = 28$. Data were smoothed by a 5 point FFT filter. | 78 |
| 4.18 Qualitative tube temperature profile and sample points. | 80 |
| 4.19 Photographs (left panels) and mass spectra (right panels) from reaction zone shifting experiments: I) Sampling at the reaction zone onset, II) Sampling between reaction zone onset and temperature maximum, III) Sampling at temperature maximum. | 81 |
| 4.20 Cut through a $\text{Pt}/10\%\text{ Rh}$ tube, used in the methane CPO reaction. Visible are several regions, part of them are visually covered with carbon. Gas flows from left to right. | 82 |
| 4.21 I shows the cold inlet region - only striations from the production process are visible. In region II the change into the reaction zone is displayed. The bright stripe contains Rh_xO_y , in flow direction carbon formation starts. The carbon film is not dense, but consists of partly carbon covered particles and small carbon deposits, shown in region III . At the hottest position the surface is massively destructed, as shown in IV and in a cross section VI . The carbon deposits at the outlet, region V , are relatively equal to III | 83 |

-
- 4.22 Region **IV** from the vacuum (outer) side. **I** shows the ETD detector picture, representing the topography, **II** the SSD detector, displaying more the elementary contrast. 85
- 4.23 Axial temperature profiles for different maximum temperatures at $C/O = 0.6$ and $\dot{F}_{total} = 1000 \text{ ml} \cdot \text{min}^{-1}$ 86
- 4.24 Oxygen and methane conversions as function of temperature at $C/O = 0.6$ and $\dot{F}_{total} = 1000 \text{ ml} \cdot \text{min}^{-1}$ 88
- 4.25 Product selectivities as function of temperature at $C/O = 0.6$ and $\dot{F}_{total} = 1000 \text{ ml} \cdot \text{min}^{-1}$. In **I** the carbon based selectivities are shown, in **II** the hydrogen based one. The H_2O molecular flow was calculated in respect to the hydrogen balance. 89
- 4.26 Estimated O_2 concentration profile as result of convective axial O_2 transport, radial O_2 diffusion and catalytic O_2 conversion at the Pt tube wall: (A) Radial O_2 profile close to entrance; (B) Radial O_2 profile in tube middle; (C) Radial O_2 profile close to tube exit. 90
- 4.27 Molecular flow rates of CO and CO_2 as function of temperature at $C/O = 0.6$ and $\dot{F}_{total} = 1000 \text{ ml} \cdot \text{min}^{-1}$. At $1150 \text{ }^\circ\text{C}$ an additional production of CO_x is observed. 91
- 4.28 Temperature profiles at maximum tube temperatures of $1100 \text{ }^\circ\text{C}$ and $1200 \text{ }^\circ\text{C}$ respectively at $C/O = 0.6$. The pronounced maximum (shaded area) in the $1200 \text{ }^\circ\text{C}$ profile is attributed to heat liberation by exothermic gas phase oxidation reactions. 92
- 4.29 Left: Threshold ionization IE curve at $1015 \text{ }^\circ\text{C}$ showing no signal increase at 9.8 eV . The curve onset at 14 eV corresponds to methane fragmentation ($CH_4^+ \rightarrow CH_3^+ + H\cdot$) in the MS ionizer. The inset represents a mass spectrum at 11.9 eV showing nearly no signal at $m/z = 15$. No $CH_3\cdot$ radicals were detected. Right: Threshold ionization IE curve at $1310 \text{ }^\circ\text{C}$. The onset at 9.8 eV corresponds to ionization of $CH_3\cdot$ radicals. The inset represents a mass spectrum at 11.9 eV showing a high peak at $m/z = 15$ but nearly no ionization of CH_4 at 16 amu 93

| | | |
|------|--|-----|
| 4.30 | Methyl radical flow rates measured at the tube center and selectivities to C_2H_6 , C_2H_4 and C_2H_2 measured at the tube outlet as function of temperature. | 94 |
| 4.31 | Stability of different hydrocarbons in methane pyrolysis - adopted from [130]. | 96 |
| 4.32 | Calculated 2D temperature profile in the Pt tube up to the sampling position at 5 mm. | 97 |
| 4.33 | Calculated 2D $CH_3\cdot$ radical profile in the Pt tube up to the sampling position at 5 mm. | 97 |
| 4.34 | Gas chromatogram at $C/O = 0.6$ and $1300^\circ C$ showing peaks of unknown C3 and C4 hydrocarbons. | 99 |
| 4.35 | Fragmentation pattern of: a.) 1,3-butadiyne at 13.4 min; b.) 1-butene-3-yne at 12.6 min, c.) propyne at 9.8 min and d.) allene at 9.6 min. The insets represent reference spectra from NIST [135]. . . | 99 |
| 4.36 | Temperature dependent selectivities for C3 and C4 hydrocarbons at a $C/O = 0.6$ | 100 |
| 4.37 | Occurrence of flames in the Pt tube at $1300^\circ C$ and $C/O = 0.6$. View through the tube. | 101 |
| 4.38 | Temperature profiles for variable C/O ratios (0.6, 1.0, 2.0) at $1100^\circ C$ tube temperature maximum and $500\text{ ml}\cdot\text{min}^{-1}$ inlet flow rate. | 103 |
| 4.39 | CH_4 I and O_2 II conversions with variable C/O ratios. For a C/O of 0.6 and a flow rate of $500\text{ ml}\cdot\text{min}^{-1}$ gas phase reactions were observed. | 104 |
| 4.40 | C2 selectivities for variable C/O at $1000\text{ ml}\cdot\text{min}^{-1}$ inlet flow rate. . . | 105 |
| 4.41 | C2 selectivities for variable C/O at $500\text{ ml}\cdot\text{min}^{-1}$ inlet flow rate. . . . | 105 |
| 4.42 | Flammable limits of methane in oxygen with nitrogen as diluent, adopted from [143]. Circles represent the three used C/O ratios. | 107 |
| 4.43 | Ignition delay times for different temperatures with a C/O of 0.6 - resident times for three flows velocities. | 109 |

| | | |
|------|---|-----|
| 4.44 | Temperature profiles of three flow velocities with a C/O of 0.6 direct after gas phase ignition. | 110 |
| 4.45 | Ignition delays for different C/O ratios with a flow of $500 \text{ ml} \cdot \text{min}^{-1}$ | 111 |
| 5.1 | Interaction of surface and gas phase chemistry in the high temperature catalytic methane oxidation on platinum. | 116 |

List of Tables

| | | |
|------|--|-----|
| 4.1 | Possible degrees of freedom for the main gas components at 1573 K . . | 49 |
| 4.2 | Parameters for the determination of the detection limit of CO in N_2 . | 62 |
| 4.3 | Results for the analysis of CO in N_2 | 62 |
| 4.4 | GC calibrations of available compounds | 66 |
| 4.5 | GC calibrations per C-atom | 66 |
| 4.6 | Dynamic viscosities of reactants and products | 71 |
| 4.7 | Reactor inlet gas composition | 72 |
| 4.8 | Molecular fractions of the constituents of the product gas streams . . | 73 |
| 4.9 | Parameters to estimate the O_2 diffusion coefficient in the reaction mixture | 76 |
| 4.10 | Comparison of characteristic times for axial convective and radial diffusive O_2 transport τ_C, τ_D respectively | 77 |
| 4.11 | Experimental conditions for variable C/O experiments | 102 |

Affidavit

I hereby declare that this PhD thesis has been written by myself and without any assistance from third parties. I confirm that no other sources have been used in the preparation of this thesis than those indicated in the thesis itself.

.....

Signature

12th October 2009

I express my gratitude to ...

- .. Prof. Dr. Robert Schlögl for giving me the opportunity to prepare this work in an excellent surrounding, offering interesting projects and providing scientific advice
- .. Prof. Dr. Reinhard Schomäcker for taking over the second opinion
- .. Prof. Dr. Michael Gradzielski for taking the chair of the examination board
- .. Dr. Raimund Horn for realizing the MBMS apparatus, his very helpful discussions and the revision of the manuscript
- .. Prof. Dr. Friedericke Jentoft for advising me during the first half of this work
- .. Dr. Axel Knop-Gericke for the supervision during the second half of the work
- .. my colleagues from the High Temperature Catalysis Group for all the scientific discussions and help
- .. all other colleagues in the Department of Inorganic Chemistry and the staff members of the different service groups at the Fritz-Haber-Institute of the Max-Planck-Society
- .. the staff from Haberling for two, relatively uncomplicated moves without breaking any of the machines

Curriculum Vitae

Personal Data

Name: Michael Geske
Address: Geschwister-Scholl-Str. 7
15566 Schöneiche
Date of Birth: November 10, 1978
Place of Birth: Frankfurt (Oder), Brandenburg, Germany
Nationality: German

School

1986-1987: Polytechnische Oberschule
'Georgi Dimitroff' Frankfurt (Oder)
1987-1991: Polytechnische Oberschule
'Clara Zetkin' Frankfurt (Oder)
1991-1998: Carl-Friedrich-Gauß-Gymnasium Frankfurt (Oder)
1998: Abitur

University

1999-2005: Study of Chemistry at the Technische Universität Berlin
Intermediate exam in April 2002
Final exam for degree 'Diplom-Chemiker' in February 2005
Thesis in Analytical Chemistry under the supervision of
Dr. Wolfgang Frenzel
Title: „Untersuchung zur Automatisierung photometrischer
Bestimmungsmethoden mit einem kommerziell
erhältlichen Sample Processor“

since Mai 2005: Ph.D. student at the Department of Inorganic Chemistry,
Fritz-Haber-Institute of the Max-Planck-Society in Berlin,
under the supervision of Prof. Dr. Robert Schlögl